

# Micro capillary dielectric barrier plasma jet discharge

Characterisation by optical spectroscopy

---

Dissertation  
zur Erlangung des Grades  
eines Doktors der Naturwissenschaften  
der Physik Fakultät der Universität Dortmund

vorgelegt von  
Stefan-Bogdan Olenici-Craciunescu

Technische Universität Dortmund  
Leibniz-Institut für Analytische Wissenschaften – ISAS e.V.  
Juli 2011



## Contents

1	Introduction .....	5
2	Microplasma discharges .....	9
2.1	Plasma discharges .....	9
2.2	Laboratory plasma generation .....	11
2.3	Basic plasma processes .....	11
2.4	Plasma classification .....	16
2.5	Atmospheric pressure plasma discharges .....	18
2.6	Microplasmas .....	21
2.7	The operation principle and applications of the dielectric barrier discharge....	24
2.8	Atmospheric pressure plasma jets .....	30
3	The dielectric barrier discharges as analytical detectors .....	37
3.1	The dielectric barrier discharge as detector for laser absorption spectrometry	37
3.2	Atmospheric pressure microplasma cell as emission detector for organic compounds in gas chromatography .....	39
3.3	The first approach on the capillary dielectric barrier plasma jet discharge as ionisation source .....	40
3.4	The capillary dielectric barrier plasma jet discharge implemented as ionisation source for LC/MS .....	47
4	The capillary dielectric barrier plasma jet characterized by optical emission and ion mobility spectrometry .....	55
4.1	Experimental arrangements for the characterisation of the capillary dielectric barrier plasma jet .....	55
4.2	Ion mobility spectrometry .....	57
4.3	Optical emission spectroscopy .....	59

---

4.4	Experimental arrangement for optical emission spectroscopy.....	62
4.5	Results and discussions .....	63
4.6	Conclusion .....	71
5	Spatially resolved spectroscopic measurements of the capillary dielectric barrier plasma jet.....	73
5.1	Experimental arrangement for plasma jet mapping .....	73
5.2	Measurements and results .....	75
5.3	Description of line intensity distributions .....	77
5.3.1	Spatial density distributions in the jet .....	77
5.3.2	Excitation energy transfer processes involving He, N <sub>2</sub> , and H <sub>2</sub> O.....	78
5.3.3	Rate equations .....	82
5.3.4	Discussion of the shapes of line intensity distributions .....	84
5.4	Comparison of experimental data with model data .....	87
5.5	Conclusion .....	90
6	Estimation of the number density of He metastable atoms in the plasma jet ...	93
6.1	Optical absorption measurements for evaluating the He metastable density in the plasma jet .....	93
6.2	Observed spectral intensities.....	97
6.2.1	Number density distributions .....	97
6.2.2	The spectral intensity of the measured He lines .....	99
6.3	Broadening of the He lines.....	101
6.3.1	General aspects .....	101
6.3.2	Lorentz and Doppler broadening of the He 728.1 nm line .....	102
6.3.3	Voigt profiles and Pearson-7 function .....	103
6.3.4	Measured line intensities.....	104
6.3.5	Curve of growth .....	106

---

6.3.6	Simulated curves of growth for He 728 nm line.....	106
6.4	Estimation of the number density of He .....	108
6.4.1	He emission lines measurements .....	108
6.4.2	The optical thickness of considered lines .....	110
6.4.3	The excitation temperatures.....	111
6.4.4	The procedure to estimate the number density of He metastable.....	111
6.4.5	Density estimations.....	112
6.4.6	Discussion, conclusion and outlook .....	114
7	Conclusion and Outlook .....	115
8	Appendix .....	119
8.1	Conversion of energy units.....	119
8.2	Basic aspects of optical spectroscopy.....	119
8.3	The curve of growth for He 728 nm determined using Origin software .....	125
8.4	Abel transformation.....	129
	Bibliography .....	133
	Acknowledgments .....	141



# 1 INTRODUCTION

Since Crooks first came up in 1879 with the idea that ionised media inside of a discharge in low pressure gases can be considered as a state of matter, different from the well-known solids, liquids and gases [1], the research in this field has evolved continuously. Later, Langmuir named this new form of matter plasma, considering the property of the gas discharges to fill-in the available space. It is considered that plasma represents 99 % of the matter in the Universe (the stars and the space between them). On Earth plasma is present in the form of lightning, fire flame and the auroras. The most common way to produce plasma artificially is represented by the discharges between two electrode plates in rare gases at low pressure. The investigations that have been done along the time on the plasma discharges lead the scientists to consider this media as one with new and very useful properties. The particles that are generated inside plasma like ions, electrons, excited atoms and photons, gain energy and are reactive. This property can be used by manipulating the plasma particles. Many applications have been developed and investigated using plasma discharges based on different geometries using various materials for the electrodes, different gases in a large range of pressures or even liquid solutions or powders, different ways to ignite and sustain the discharges using various power sources and sometimes additional features like heating or magnetic fields. This large flexibility in producing plasma leads to a large diversity of plasma sources with a wide range of applications in industry, energy, biomedicine, analytics and quality of life. In some areas plasma plays a crucial role and cannot be replaced. One of these fields is represented by the analytics where most of the devices are based on a plasma source to ionise the analytes so that they can be further determined. The demands of nowadays are to develop sensitive, reliable, inexpensive and easy to handle devices, but at the same time portable, so that “the lab” is brought to the sample. This implies also to provide small and low power consumption ionisation sources, as well as a good sensitivity for a wide range of analytes. Also operation at atmospheric pressure has to be considered because for most of the analytical devices the samples are in open air.

Such an ionisation source was developed based on a capillary dielectric plasma jet discharge. It was implemented and tested on devices like ion mobility spectrometer

(IMS) and liquid chromatography coupled with mass spectrometry (LC/MS) and the results proved that it has successfully accomplished the specific requirements.

In this work the plasma source and the results obtained in characterizing it are presented. The focus of the research was aimed to get more insights into the physical properties of the plasma jet concerning the processes involving the energy transfer between different species.

The work is structured on two parts. The first part, containing only one chapter, is an introduction into the field of plasma physics. Basic aspects concerning plasma, atmospheric plasma, dielectric barrier discharges, microplasmas and plasma jets are presented. The reader is brought from the vast field of plasma discharges up to the plasma jet discharges and their applications, passing through specific aspects that have to be taken into consideration in order to describe and characterize the plasma jet subject of this thesis.

The second part presents the results of the experiments conducted in order to characterize and implement a capillary dielectric plasma jet discharge as an ionisation source. It contains four chapters. The first chapter presents the implementation of dielectric barrier discharges in the field of analytical sciences. A chronological transition and the evolution in the development of the present plasma jet are presented. The first results in characterizing the plasma jet as well as the first implementations as ionisation source for analytical devices, like IMS and LC/MS are presented.

It follows a chapter in which a more detailed investigation of the capillary dielectric plasma jet is done. The results obtained by means of optical spectroscopic investigation bring new features of the plasma jet. A comparison between He, Ar and Ne as working gases for the plasma discharge shows which of these gases give the best results when the plasma jet is implemented as soft ionisation source in the IMS. Based on the ionisation principle that takes place in an IMS device, mixtures of the He, Ne and Ar each with different concentration of N, are implemented as working gas for the plasma and analysed by means of optical spectroscopy. The results obtained lead to a possible energy transfer scheme between the plasma species based on Penning ionisation, and concluded that He is the best suited gas to be used.



The second chapter of this part describes the results obtained using He as working gas for the plasma jet based on the previous results. Spatially resolved spectroscopic measurements of the plasma jet resulted in a three dimensional mapping. This mapping shows a clear distribution of the reactive species in the plasma jet. A simplified model based on the energy transfer processes and the rate equations involving He, N<sub>2</sub> and H<sub>2</sub>O is presented and is proven to be in accordance with the experimental results. The main role in the ionisation process of water is showed to be played by the He metastable atoms inside the plasma jet.

The next chapter gives an estimation procedure of the density population of one of the excited He states which populates a metastable level by radiative transition. The evaluation was made based on spectroscopic measurements done for the plasma jet mapping. Considering the emission line broadening parameters presented in the case of the chosen optically thin line, a simulation of the curve of growth was done from which the density population could be estimated.

The work that has been done so far in characterizing this plasma jet brought more insights on the processes that take place. A path describing the energy transfer when the plasma jet is implemented as ionisation source was presented and the behaviour of the important atomic and molecular species is described.



## 2 MICROPLASMA DISCHARGES

### 2.1 Plasma discharges

The plasma physics appeared as modern continuity and development of the older physics chapter of gas discharges that started back in the middle of the XIX century. The term of plasma was lately brought out by Irving Langmuir (1928) to describe, in contrary with the thin charged sheets close to the electrodes, the electrically neutral part of a gas discharge [2] and was used like this in the classical paper of Tonks and Langmuir about electrical oscillations in gas discharges [3]. The etymology of the term leads to the greek word *πλασμασ* that defines the action of “pouring“. This suggests the fundamental capacity of the plasma to “fill in” the shape of the discharge tube, but also the property to act as a fluid capable of collective response to the action of electric and magnetic fields. To nowadays acceptance, the term plasma defines a gaseous mixture of neutral particles (atoms in ground and excited states, photons) and electrically charged particles (positive and negative ions and electrons) where the percentage of the last ones is big enough so that the electromagnetic interactions lead to a collective behaviour of the whole particles assembly and also give the electrical conductivity. From a macroscopic point of view, plasma is electrically neutral. Plasma can be seen as the fourth aggregation state of the matter. This idea was first presented by Crooks in 1879. He considered the ionised media inside of a discharge in low pressure gases to be one state of the matter with different qualitative properties compared to those well-known for solids, liquids and gases [1]. Although it forms 99 % of the matter in the Universe (the stars and the space between them) the plasma does not exist under the normal thermodynamically conditions of the life on Earth<sup>1</sup>. That means that in order to be studied and used, plasma has to be created under artificial conditions. On the upper layer of the Earth’s atmosphere the plasma state is present due to photoionisation of atoms and molecules by cosmic ray giving raise to aurora borealis at

---

<sup>1</sup> Normal thermodynamically conditions on Earth: pressure on the range of  $10^5 \text{ N m}^{-2}$  and temperature of  $3 \times 10^3 \text{ K}$ .

the poles of the earth. Also, electrical discharges in atmosphere (lightning and thunderbolt) generate plasma for short periods of time. Artificial plasma can be found as different technical applications like arc discharge, fluorescence tubes, the gases exhausted by the jet engines, technical treatment devices, nuclear fusion reactors etc.[4].

To come up with an idea about the energy required to bring up a certain chemical element into the plasma state, one should have in mind that the specific energies of thermal agitation of the atoms and molecules of solids, liquids and gases are very small. They represent only a few tenths or hundredths of electron Volts<sup>2</sup> (eV) compared to those required to excite and ionize atoms and molecules that are in the range of eV. These big values required for the dissociation of the molecules and the ionisation of the atoms explain why under normal temperature and pressure conditions on Earth, plasma cannot appear naturally or it requires high amounts of energy like in case of lightning. Considering a system formed by the neutral particles of a gas, positively charged particles (ions) and the corresponding negatively charged particles (electrons and negative ions), one can say that this system represents a plasma only if the ionisation ratio (charged/neutral particles) is big enough, so that the movement of the charged particles is governed by collective interactions<sup>3</sup>. In plasma, the collective interactions are the statistical result of the electromagnetic forces produced by the charged particles in movement. Each charged particle of the plasma undergoes the external electromagnetic field but also the macroscopic field generated by all the other particles of the plasma. This characteristic of the particle interactions makes that plasma, as physical system, to be described by self-consistent models, in which the movement of the charged particles (positions and the corresponding speeds) determine the forces that afterwards will govern this movement. Compared to the charged particles, the movement of the neutral ones is governed by the local conditions represented by the binary collisions with the neighbouring particles.

---

<sup>2</sup> To express the kinetic energy of different particles and to compare it with the respective bounding energy, the Joule ( $1\text{J}=1\text{ N} \times 1\text{m}$ ) is not an appropriate measure unit. This is the reason why in the plasma physics is used the electron-volt unit (eV), which represents the kinetic energy gained by an electron in an electrical field with a potential difference of 1 V ( $1\text{ eV} = 1.602176487(40) \times 10^{-19}\text{ J}$ ).

<sup>3</sup> Collective interactions are those that involve a large statistical number of particles.

## 2.2 Laboratory plasma generation

As presented above, in order to generate plasma one should provide the neutral gas system with a big amount of energy that leads to the production of excited species (atoms, molecules) and the formation of charge carriers (electrons and ions). This energy can be thermal or carried by either an electric field or electromagnetic radiation. Electrons and ions are produced in the gas phase when electrons or photons with sufficient energy collide with neutral atoms and molecules of the working gas (electron impact ionisation or photoionisation). There are various ways to supply the necessary energy for plasma generation to a neutral gas. One possibility is to supply thermal energy, for example in flames, where exothermic chemical reactions of the molecules are used as the prime energy source. Adiabatic compression is also capable of gas heating up to the point of plasma generation. Yet another way to supply energy to a gas reservoir is via energetic beams that moderate in a gas volume [5]. Beams of neutral particles have the additional advantage of being unperturbed by electric and magnetic fields. Neutral beams are primarily used for sustaining plasma or for plasma heating in fusion devices. The most used method of generating and sustaining a low-temperature plasma for technological application is by applying an electric field to a neutral gas. Any volume of neutral gas always contains a few electrons and ions that are formed, for example, as a result of interaction with cosmic rays or radioactive radiation with the gas. These free charges are accelerated by the electric field and new particles may be created when they collide with atoms and molecules in the gas or with the surface of the electrodes. This leads to an avalanche of charged particles that is eventually balanced by charge carrier losses, so that a steady-state plasma is developed.

## 2.3 Basic plasma processes

In order to get a better idea about what artificial plasma (produced in laboratory) means, one should consider the processes that take place in such a system. An easy way is to separate them in bulk processes and surface processes [4].

The last ones are those that take place at the interaction between the plasma particles and the surface, in most of the cases between charged particles and electrodes, as these are accelerated towards them: negative ions and electrons to the anode, and positive

ions to the cathode, respectively. As a result of these interactions, several phenomena can take place. The most important ones are those at the cathode surface where heavy charged particles with high kinetic energy strike the surface. Thus the cathode heats up and electrons can be extracted from the structure on the metal or even atoms, a principle that is used in plasma surface treatment.

The bulk processes are represented by the collective motions of the charged particles under the action of external fields and collisions between different types of components with kinetic energy. The most common collisions are the so-called binary collisions that take place between pairs of particles. Useful details about binary collisions can be revealed by the laws of energy and momentum preservation that can be summarised as follows:

Lighter particles ( $m$ ) cannot lose too much energy through elastic collisions with heavier particles ( $M$ ) - at best a fraction  $2m/M$ ; nevertheless, substantial changes of the smaller particle momentum occurs (like throwing a ball to a wall).

A moving particle striking elastically a stationary one of equal mass head-on can transfer all of its kinetic energy (like billiards).

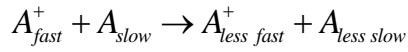
Lighter particles can lose virtually all their kinetic energy through inelastic collisions with heavier objects (like sandblasting).

Equal mass particles can lose no more than half their kinetic energy through inelastic collisions (ion impact ionisation).

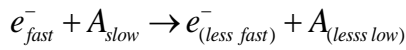
Binary collisions in which at least one particle is charged may be dominated by long-range Coulomb forces. The electric field transmits energy to the gas electrons (which are the most mobile charged species). This electronic energy is then transmitted to the neutral species by collisions. These collisions follow probability laws and can be divided in elastic collisions when the internal structure and energy of the particles involved does not change and the laws of energy and momentum preservation are fulfilled, and inelastic collisions when the internal structures of the particles involved varies and kinetic energy is lost. When the energy of the electrons is high enough, these collisions modify the electronic structure of the neutral species. It results in the creation of excited atoms or ions if the collisions are energetic enough. Most of the excited species have a very short lifetime and they get to ground state by emitting a photon. The

so-called "metastable species" are also excited states but with longer life-times because their decay by emission of radiation is hampered, as there are no allowed optical transitions departing from the respective state: decay can only take place by energy transfers through collisions. Now, a short overview of the collisions will be given presenting the type of the involved particles [4].

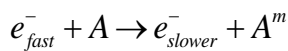
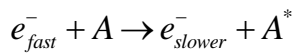
The elastic collisions that take place between neutral atoms  $A$  and the corresponding positive ions  $A^+$  determine an kinetic energy transfer leading to a random distribution of the motion with a mean thermal speed and thermodynamic equilibrium (the temperature of the ions and neutrals are equal  $T_i = T_n$ ).



In the elastic collisions involving energetic electrons and neutrals, the energy transfer is only in the fraction of  $m_e/M$  from their initial kinetic energy due to their small mass compared to the neutral atoms. Though this fraction is small, in the case of high pressure of the neutral gas, the number of these collisions is very high and they represent the main mechanism through which the electrons lose their energy gained from the electrical field.

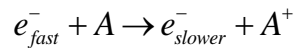


The inelastic collisions represent the way that leads to the loss of kinetic energy of charged particles. This is the important way to produce plasma particles like excited atoms on different energetic states or on metastable<sup>4</sup> states and positive ions from atoms on ground state respectively. The collisions between kinetic electrons and neutral atoms of the plasma resulting in excited  $A^*$  and metastable  $A^m$  atoms or ions  $A^+$  can be expressed as follows:

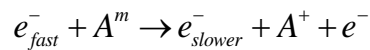



---

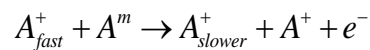
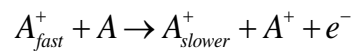
<sup>4</sup> The excited metastable states represent those atomic excited states that have a longer life time than other excited states which having a short lifetime in the order of  $10^{-8}$  s are considered to be unstable. The long lifetime of the metastable states makes their populating density to be relatively high, fact that leads to an increase ionisation probability of them by collisions with electrons or other plasma ions.



In order to produce an ion from a neutral atom, the colliding electron should have a kinetic energy equal or greater than the ionizing threshold energy of the atom on ground state  $eV_i$  ( $e$  is the elementary electric charge and  $V_i$  is ionizing potential). When the electrons collide with atoms on a metastable excited state, the kinetic energy required for ionisation is smaller<sup>5</sup>.

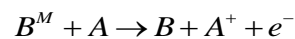


Ionisation of atoms can also be realized by collisions between energetic positive ions with neutral atoms in ground or different excited states including metastables.



In this case, in order to fulfil the preservation law of momentum and taking into consideration that the mass of the involved particles are of the same order, the kinetic energy of the ions should be at least two times bigger than the ionisation energy of the atoms.

Not only collisions between charged particles with kinetic energy and atoms can lead to the ionisation of the last ones, but also collisions between neutral atoms that possess inner energy, like atoms on metastable states, and atoms on ground state. This type of energy transfer through collisions is called Penning ionisation and can take place in plasmas that contain a mixture of two gases ( $A$  and  $B$ ) with one of them having the metastable excitation energy ( $E_M^B$ ) bigger than the ionisation energy of the other one ( $eV_i$ )<sup>6</sup>:



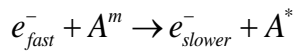
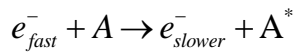

---

<sup>5</sup> To ionise a *He* atom from the ground state it requires an energy of 25 eV, while it requires only 5.2 eV to ionise the same *He* atom found on a metastable state (with an energy of 19.8 eV), representing the energy differences between these two states.

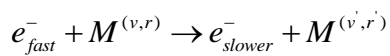
<sup>6</sup> Penning ionisation plays an important role in ionisation of the *Hg* atoms which are used in a gas mixture with *Ar* for industrial production of fluorescent lamps. The energy of the metastable excited state of the *Ar* is of 16 eV, while the ionisation energy of the *Hg* only of 4.9 eV.



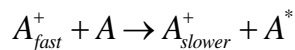
The collisions of kinetic electrons with neutral atoms in ground state or in a metastable state can lead to the transition of the last ones on a higher excited state like it follows:



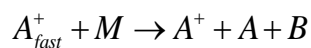
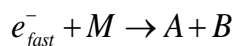
In the case of molecules  $M$  the number of different excited states is much bigger due to many vibrational and rotational energy levels, so the number of different inelastic collisions multiplies.



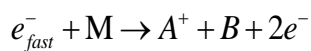
The excitation of atoms through collisions with kinetic ions is also possible, but in this case the kinetic energy of the ions should be at least two times bigger than the energy required to bring the neutral atoms from the ground state to the excited one,  $E_{kin} = 2eV_{ex}$ :



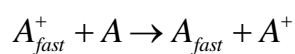
In the case of the molecules  $M$ , besides the collisions of these with charged particles that lead to excitation of them on different states, they can also be dissociated as it follows:



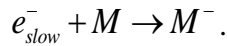
After the dissociation of molecules the ionisation of the components can follow:



The resonant charge transfer that leads to production of energetic neutral atoms represents also an important process that can take place in plasma discharges, especially in the cathodic region of a glow discharge:



In some plasma containing molecules with a high electron affinity like those containing  $O_2$  and  $FS_6$  an important process to produce negative ions is represented by the charge attachment:



## 2.4 Plasma classification

As already stated, to produce plasma on Earth (laboratory plasmas) one should provide specific conditions of temperature, pressure and energy transfer in order to obtain plasma particles (excited atoms, energetic electrons and ions, photons). In order to achieve these conditions, different technological conceptions can be used involving large pressure range from atmospheric pressure to a few millibars, different ways to couple the energy to produce plasma particles and different geometries in a large scale of dimensions, from microplasmas to huge fusion reactors. Despite this large production variety, all plasmas have a number of features in common. For example, they are composed of equal amounts of positive and negative charges carried by particles that are arranged without any local ordering, being free to move. As differences between plasmas the most visible and important ones are those which are determined by the used

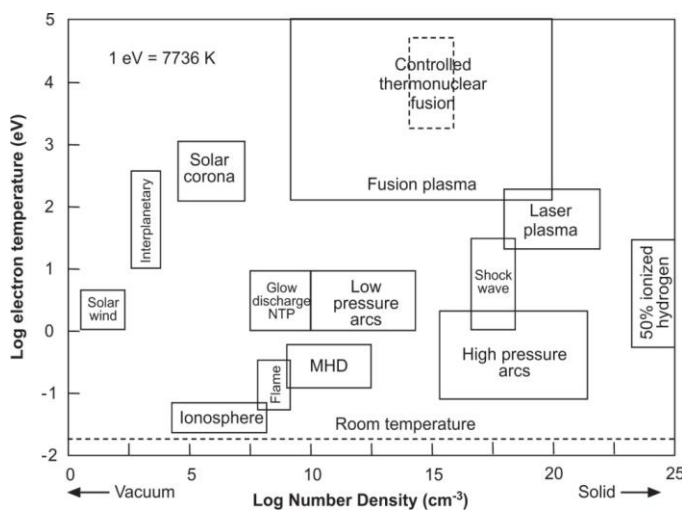


Figure 2.1 Classification of plasmas [5].

working gas, the density of the charged particles ( $m^{-3}$ ) and the thermal energy of these particles. Despite the large variety in plasma production only two most important parameters are taken into consideration in characterization of plasmas: the density of the charged carriers (number  $m^{-3}$ ) and the thermal energy of the electrons in

particular. These consideration lead to a classification of plasmas, both naturally and artificially produced, as can be seen in Figure 2.1 [6].

Also an important aspect in describing plasmas is represented by the temperature (energy) of the plasma components: electrons, ions and neutral atoms. How the temperature of the plasma components vary with the gas pressure is presented in the Figure 2.2 [6]. Considering this aspect, the plasmas can be separated into two distinct

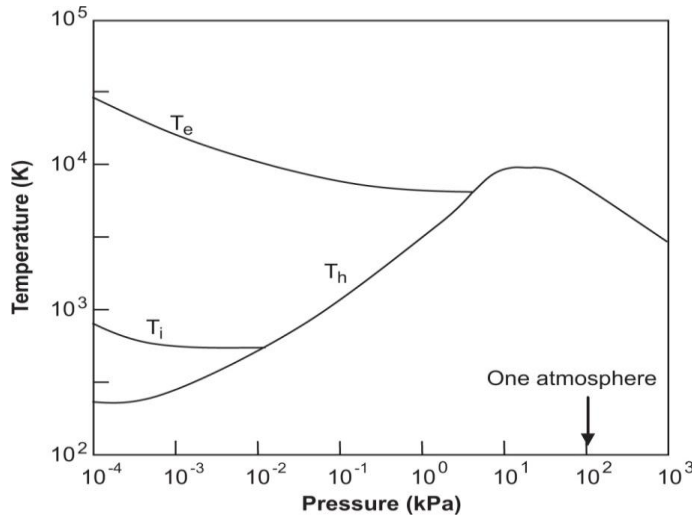


Figure 2.2 Variation of the electron and heavy particles temperature with pressure [5].

categories depending on the amounts of energy transferred to their components. The properties of the heavy particles (ions and atoms), like density and kinetic energy or temperature, separates the plasmas into thermal and nonthermal. Thermal plasmas have  $T_e \equiv T_h$  (where  $T_e$  represents the electron temperature and  $T_h$  represents the temperature of the heavy

particles like ions and neutral atoms). In the core of the plasma these temperatures can reach values up to 10000 K and the gas is significantly ionised. Atmospheric nonthermal plasmas have a very high electron temperature  $T_e$ , while the temperature  $T_h$  of heavy particles remains at the ambient value. They also have a low degree of ionisation and consequently a small density of charged particles. The electrons and ions never achieve local thermodynamic equilibrium, which is the reason why gas remains at room temperature or very slightly above it. However, nonthermal plasmas have a high density of active species like atoms in different excited states including metastables and free radicals, giving them a very reactive character. This is the reason why plasmas have a wide variety of potential industrial applications that will be further presented and discussed in the next section.

## 2.5 Atmospheric pressure plasma discharges

As their name says, atmospheric plasmas are operated in the range of normal atmospheric pressure. The working gas is in the range of atmospheric pressure, or the device produces the plasma in open air. In order to ignite the plasma, a breakdown voltage  $V_b$ , specific for each working gas must be exceeded. Considering a classical discharge that can be produced between two powered electrodes, the ignition voltage that must be applied to the electrodes depends on the distance between them and the pressure of the gas according to the following equation [7, 8]:

$$V_b = \frac{B(p \cdot d)}{\ln[A(p \cdot d)] - \ln\left[1 + \frac{1}{\gamma_{se}}\right]},$$

where  $A$  and  $B$  are specific parameters which are experimentally determined. They are

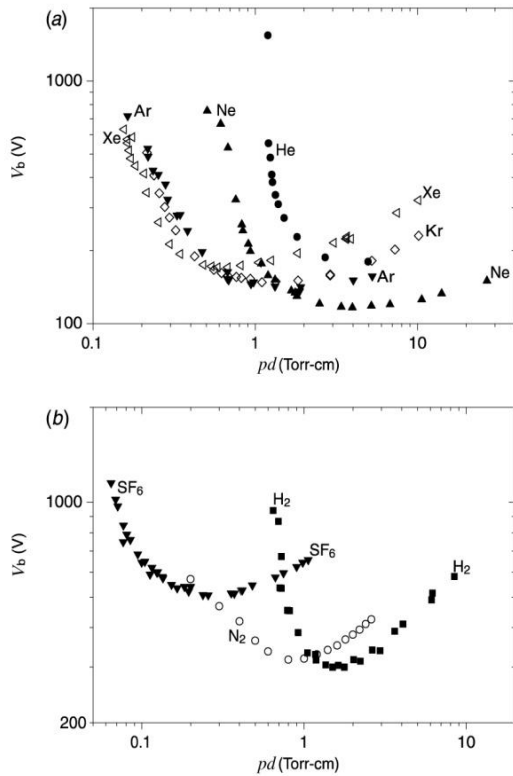


Figure 2.3 Breakdown voltage for plane-parallel electrodes at 20°C: a) noble gases; b) moleculara gases [6].

found to be roughly constant over a restricted range of  $E/p$  for any given gas. The corresponding units are  $\text{cm}^{-1} \text{Torr}^{-1}$  for  $A$  and  $\text{V cm}^{-1} \text{Torr}^{-1}$  for  $B$  respectively, while  $\gamma_{se}$  is the secondary electron emission coefficient of the cathode. The breakdown voltage is a function of the product  $p \cdot d$ . For large values of this product,  $V_b$  increases essentially linearly with  $p \cdot d$ . For small  $p \cdot d$  there is a limiting value of  $p \cdot d = A^{-1} \ln(1 + 1/\gamma_{se})$ , below which breakdown cannot occur. The breakdown voltage has a minimum  $V_{min}$  at an  $p \cdot d = (p \cdot d)_{min}$  intermediate value. The curve  $V_b(p \cdot d)$  is called the Paschen curve, and is a function of

the gas and weakly a function of the electrode material. In Figure 2.3 are shown some

typical breakdown curves for different gases in a discharge with plane-parallel electrodes. It can be clearly observed, that for each gas there is a minimum in the curve that gives the required working conditions (pressure and distance between the electrodes) in order to apply the lowest breakdown voltage. From the Paschen law follows that if the working gas is at atmospheric pressure and the distance between the electrodes is in the microscale range, then the igniting voltage should have a considerably high value. This involves the use of expensive and large power supplies.

Another way to produce plasma at atmospheric pressure with similar physical properties and at the same time to use lower voltages power supplies is to reduce the dimensions of the discharges, respectively the distances between the electrodes. This miniaturisation (down-scaling) of the discharges comes as a necessity to use plasma sources, which in some fields of applications cannot be replaced, capable to work in stable condition at atmospheric pressure. In this way lots of plasma discharges were down-scaled giving rise to a family of miniaturised discharges, like dark or Townsend discharge, the glow discharge, the corona discharge and the dielectric barrier discharges. Due to their small dimensions these discharges can be incorporated in other bigger devices like most of conventional analytical detection systems (e.g. inductive coupled plasma-optical spectrometry (ICP-OES) or inductive coupled plasma-mass spectrometry (ICP-MS)) as excitation and ionisation sources. They can also be used as excitation source for molecular mass spectrometry [9]. Having such a large area of application the condition of operation and specific characteristics are required to be known. The laws of similarity between two glow discharges in helium are given by Franzke [10]. Figure 2.4 illustrates that the product  $p \cdot d$ , the ratio  $E/p$  and all the quantities which are functions of  $p \cdot d$  or  $E/p$  are the same in the two systems. On the left side of the figure the cathode, the anode, and the negative glow between them are represented in case of a glow discharge. On the right side of the figure a micro-scale discharge is represented and in this case the negative glow is closer to the cathode. Between the cathode and the negative glow there is the cathode fall. The length of the cathode fall is given by the dimension  $d$ . When the pressure is  $p_1 = 30 \text{ mbar}$  and a voltage  $U = 240 \text{ V}$  is applied, the cathode fall has the length  $d_1 = 800 \mu\text{m}$ . An invariant term  $E/p$  can be calculated with these values.  $E/p$  is also valid for a discharge with smaller dimensions (microscale). When the discharge is maintained under atmospheric

pressure, the cathode fall will have a length of  $d_2 = 24 \mu\text{m}$ , as schematically shown on the right side of Figure 2.4. Therefore, the distance between the electrodes should not be smaller than  $d_2$ , otherwise the discharge cannot be ignited when operating under atmospheric pressure. This value is a limit for miniaturisation of an electrically driven discharge in He at atmospheric pressure. As shown in Figure 2.4 the smallest dimension in which a He discharge can be sustained under atmospheric pressure is  $24 \mu\text{m}$ ; for Ar this is  $6 \mu\text{m}$ .

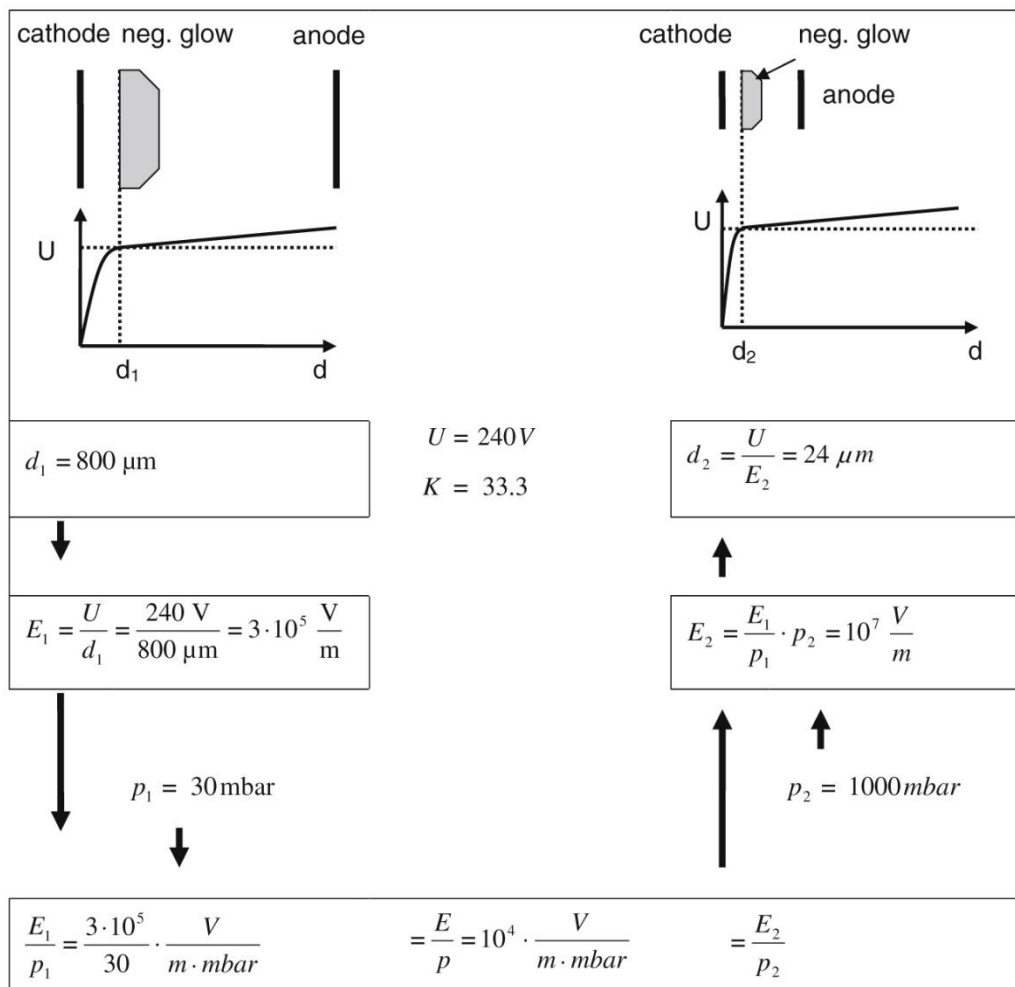


Figure 2.4 Two similar glow discharges are shown, illustrating that the product  $p \cdot d = p_1 \cdot d_1 = p_2 \cdot d_2 = 24 \times 10^{-3} \text{ m mbar}$  and the ratio  $E/p = E_1/p_1 = E_2/p_2 = 10^4 \text{ V m}^{-1} \text{ mbar}^{-1}$  are invariant in the two systems. The proportionality factor is  $K=33.33$ . After Janasek [10].

For analytical purposes it makes no sense to work with higher pressures. Therefore the limit of miniaturisation is reached for plasma discharges at the dimensions given above. If two discharges operating with the same gas, having the same electrode material and

for which the corresponding linear dimension, for example the length of the cathode falls, is given by relation  $d_1 = K \cdot d_2$ , the properties of the gas, for example the mean distance between the molecules, differ by a factor  $K$ . It is assumed that the gas temperature is the same for both discharges, and the same voltage is applied. Such discharges are called similar. Table 2.1 gives a brief overview of the most important properties of two similar discharges. Note that the voltage and current remain constant. Therefore, the relationship between current and voltage is valid for characterizing miniaturised discharges also.

Table 2.1 Similarity parameters for electrical discharges [9].

Parameters	Relation	Similarity parameters	Most of the similarity principles have been described for the glow discharge although there are other discharges also. Furthermore most of the discharges developed as miniaturised ionisation or excitation sources for analytical chemistry can be compared with the glow discharge and are applied for element spectrometry. A general
Linear dimension	$d_1 = K \cdot d_2$		
Voltage	$U_1 = U_2$	$U, I, T$	
Current	$I_1 = I_2$		
Gas temperature	$T_1 = T_2$		
Mean free path	$\lambda_1 = K \cdot \lambda_2$	$E/p, p \cdot d$	
Gas density	$N_1 = N_2 / K$		
Gas pressure	$p_1 = p_2 / K$		
Electric field	$E_1 = E_2 / K$		

presentation of the functional aspects concerning different kinds of microplasma discharges depending on the way to produce them and the field of application will be given in the following section.

## 2.6 Microplasmas

As presented in the previous sections, decreasing the dimension of the discharge by reducing the distance between the electrodes gives the possibility to operate at atmospheric pressure. In order to achieve this condition, the dimensions should be in the range of micrometers as it was demonstrated before. A short overview on this kind of discharges will be given in the following part.

The term of microplasma is used to define discharges that have dimension in the range of a few micrometers up to few millimeters, so they are at least one order of magnitude smaller than the common low-pressure and low-temperature plasma discharges used in laboratories or for different industrial applications [11]. The potential of low-temperature plasmas and the advantage of being micro are brought together by these reduced discharges. They can create a highly reactive environment containing charged particles, excited species, radicals and photons, while at the same time requiring low power sources. This and the small footprints make them suitable for integration in microsystems and portable devices. These properties increase their technological impact in many scientific domains and give them an economical potential. This fact makes the microplasma discharges to receive increasing attention and to represent a new area of interest in the field of plasma physics. Mentions on microplasmas can be found back in the late 1950's [12]. But only in the last decades the research on microplasma started to attract interest determined by the microfabrication techniques of the integrated circuits. The aim was to develop other plasma sources that could be afterwards implemented in new and complex devices designed for different purposes. Starting with this, the microplasma research began to develop very rapidly as it can be seen from the increasing number of publications and reviews [11, 13-15] and dedicated section at the major international plasma conferences and workshops. This increasing interest on microplasma has broadened their application area including bio-medical applications, displays, radiation sources, micro-medical analysis systems, gas analysers, photodetectors, microlasers, dynamic millimetre-wave and microwave devices, microreactors, propulsions systems, aerodynamic flow control, material processing and environmental applications.

Some practical considerations concerning the construction of microplasma discharges, as well as their functional parameters will briefly be presented in the following part [11]. For particular applications where integrability and portability are required, it is necessary that not only the plasma sources are subject of miniaturisation but also the adjacent components like power sources, gas supply and vacuum systems. In order to eliminate micro pumping systems which are anyway not efficient and increase the total costs, mostly atmospheric pressure discharges are in focus of research. Low-power operation is preferred especially for portable systems powered by batteries. In order to



avoid energy losses due to gas heating, mostly low-temperature plasmas close to room temperature are preferred. For construction of the microplasmas the most suitable materials have to be found depending on the application in use. They have to fulfil requirements like the right electrical properties, to be easy to manipulate during fabrication, to have a long life time and to be inexpensive. Most microplasma sources use for electrodes metals like copper, gold, platinum and nickel. Also refractory metals like molybdenum and tungsten have been used, typically for direct current sources that operate at high temperatures. For applications where transparent electrodes are required, like plasma display panels, indium-tin oxide (ITO) is used. Doped silicon can also be used as electrode material giving the possibility of straight integration with semiconductor circuits. The most common dielectric materials in use are glass, mica, kapton and ceramics. DC and DBDs discharges that rely on secondary electron emission often use films of materials with large secondary electron emission coefficients such as MgO. The most used gases for microplasma and depending on the application are the noble gases like He, Ne, Ar and Xe. These gases offer simpler chemistry and also low temperature plasmas that are required for some applications. Typically, He is used for applications at atmospheric pressure because it is easier to obtain diffuse glow-like discharges compared to any other gases and thermal instability is avoided. For discharges open to the atmosphere there is always a mixture of the working gas with air resulting in production of reactive species. When production of reactive species is desired, molecular mixtures of gases are used. The ratio of the added gas (“the impurity”) is limited to few percents of the total gas amount because most microplasma sources are not capable to sustain discharges with higher impurity concentrations. The reactive gas can be fed before the electrode region (upstream) or in the afterglow region (downstream), which prevents contamination of the plasma source. This contributes also to transport the reactive species (metastable and excited atoms species) and energy produced in the active region of the plasma downstream where the desired reaction can occur. Portable devices are restricted to low gas flows, and in the case of discharges opened to atmospheric air, back-diffusion of air can occur resulting in an unstable operation or can even extinguish the discharge. To produce microplasmas, mostly low-frequency operation in direct current (DC) or alternative current (AC) is used as it requires low-cost electronics. For better performance, operation at high frequencies is

preferred because it requires lower breakdown voltages than DC. As a result, high frequency operation leads to less energy transfer to the ions, more efficient plasma generation and longer lifetime of the devices. Pulsed operation systems are also used for a large variety of applications due to their advantages like extracting the reactive negative ions (otherwise trapped in the plasma) and reducing the average power consumption (critical for portable devices running on batteries). But probably the most important advantage is represented by the possibility to generate plasmas with electrons high energy while the background gas remains close to room temperature. These high electron temperatures offer new chemical equilibrium which is not achievable with other continually operating sources [7, 16]. Diffuse glow discharges are preferred for practical consideration due to uniformity and controlling. But some phenomena like constricted discharges, striations and patterns which are often observed in microplasmas [17-19] are still under research being not yet completely understood.

There are many of the macro-scale plasma discharges that have been taken to microdischarges. Several reviews give some detailed presentation of them and their applications [11,15,20-22]. The most investigated microdischarges are: DC microplasma discharges with different geometrical configurations, micro hollow cathode discharges, corona discharge, microwave microplasmas, inductively coupled microplasmas (mICP) and capacitively coupled microplasmas (mCCP). Among the microplasmas listed above two more microdischarges have been developed and intensively investigated: the micro dielectric barrier discharge (mDBD) and the microplasma jet (mPJ), respectively. A detailed description of these two will be given in the following sections.

## **2.7 The operation principle and applications of the dielectric barrier discharge**

As mentioned in the previous section, one of the types of atmospheric pressure discharges is represented by the dielectric barrier discharge (DBD). And like many other plasma discharges, this has been also brought to micro scale and a lot of applications were developed [22]. A short description of DBD construction, principle of

operation as well as some of the most important application will be given in the following section.

The DBD, also called barrier discharge or silent discharge, was first reported for more than a century ago in 1857 by Werner von Siemens (Figure 2.5). At that time the research was focused on using it as an ozone generator and this remained the main application for a long period of time. The production of ozone was accomplished by sending a flow of oxygen or air through the narrow annular gap between two coaxial glass tubes subjected to the influence of an alternating electrical field of sufficient amplitude. The new feature brought by this discharge apparatus was that the electrodes were positioned outside the discharge chamber and were not in contact with the plasma as presented in Siemens' first experimental arrangement (Figure 2.5). In this set-up the gas in- and outlet are on the left and on the lower side of the cylinder respectively, and the electrodes are attached as silver sheets on the inside and outside of the cylinder.

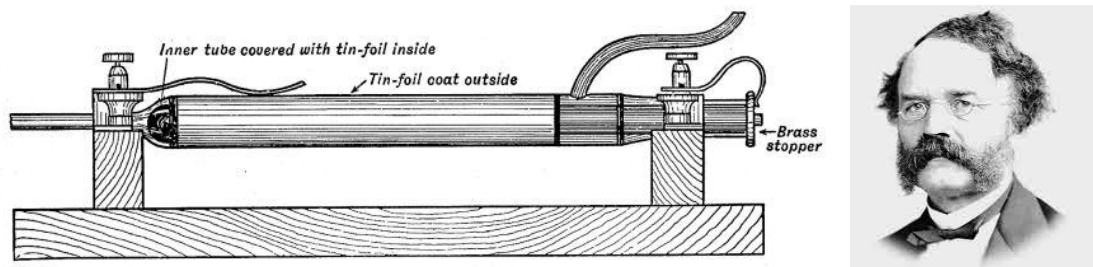


Figure 2.5 Siemens initial ozone discharge tube <sup>7</sup> and Werner von Siemens in 1872<sup>8</sup>.

Basically, a DBD consists of two plane-parallel metal electrodes, whereas at least one of them is covered by a dielectric layer. To ensure stable plasma operation, the gap which separates the electrodes is limited to a width of few millimetres [23]. The working gas flows through the gap. The discharge is ignited by means of a sinusoidal or pulsed power source. Depending on the working gas composition, the voltage and the frequency of excitation, the discharge can be either filamentary or glow. A filamentary discharge is formed by micro-discharges or streamers that develop statistically on the dielectric layer surface. The use of He as plasma gas seems to favour a glow discharge

<sup>7</sup> <http://www.lateralscience.co.uk/marum/index.html>

<sup>8</sup> <http://www.siemens.com/history/de/persoenlichkeiten/gruendergeneration.htm>

by the presence of high energetic He metastables species [24] determining the Penning effect [25, 26].

The dielectric layer plays an important role in operating the discharge as it follows:

It limits the discharge current avoiding the arc transition that enables to work a continuous or pulsed mode.

It randomly distributes streamers on the electrode surface ensuring a homogenous treatment. The streamer creation is due to the electrons accumulation on the dielectric barrier layer.

Typical materials used as dielectric barrier for these discharges are glass, quartz and ceramics. Some other materials like plastic foils, Teflon plates or insulating materials can be used too. As already mentioned, these discharges were also brought to microscale. Some geometrical configurations of mDBD are presented in the Figure 2.6 [11].

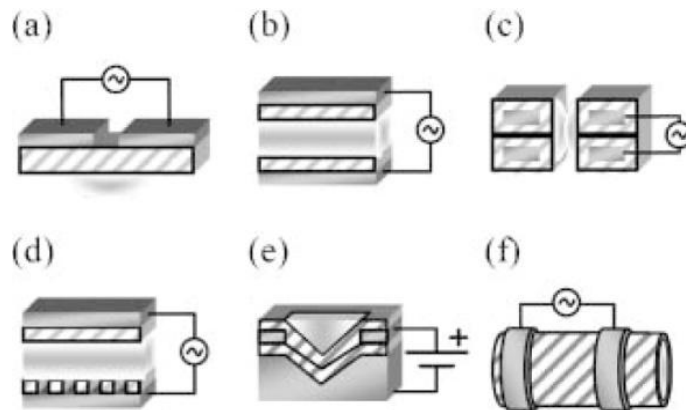


Figure 2.6 Schematics of dielectric barrier microdischarges: a) coplanar DBD b) parallel plate DBD, c) coaxial DBD, d) capillary plasma electrode discharge, e) pyramidal DBD, and f) capillary discharge/plasma pencil/plasma jet. The solid colour represents metal electrodes and hatched objects represent dielectric material [10].

As it can be observed from Figure 2.6, a variety of configurations can be used [11]. In the coplanar geometry, where both electrodes are on the same plane, the discharge is ignited like an arc on the surface (a). In planar configurations the two electrodes are parallel to each other and the dielectric is on both or only on one of the electrodes surfaces, or in the middle between them (b). Coaxial and capillary configurations can be also implemented (c, d) as well as unusual ones like pyramidal (e). Capillary discharges

where the electrodes are in shape of rings around a dielectric capillary and the plasma burns inside or is pushed outside are also in use (f). Discharges with cylindrical arrangement can be obtained using electrodes like concentric cylinders one inside the other and the dielectric material in-between them [27] like ozone generators.

As a consequence of the presence of the dielectric barrier, these discharges require alternating voltages for their operation. The dielectric, being an insulator, cannot pass a DC current. Its dielectric constant and thickness, in combination with the time derivative of the applied voltage  $dU/dt$  determines the amount of displacement current that can be passed through the dielectric(s). To transport current (other than capacitive) in the discharge gap, the electric field has to be high enough to cause breakdown in the gas. In most applications the dielectric barrier limits the average current density in the gas space. Thus it acts as ballast which, in the ideal case, does not consume energy. In some applications except the dielectric material between the electrodes, additional protective or functional coatings are applied. At very high frequencies the current limitation by the dielectric barrier becomes less effective. For this reason DBDs are normally operated with alternating voltages (sinusoidal or square-wave pulses) at frequencies between a few Hz and hundreds of kHz and at amplitudes from several hundreds of V up to a few kV. Also the dielectric helps on distributing randomly streamers on the electrode surface and ensuring a homogenous treatment. The streamer creation is due to the accumulation of electrons on the dielectric barrier layer. The preferred operating pressure is of the order of  $10^5$  Pa. This is the preferred pressure range for ozone generation, excimer formation, as well as for flue gas treatment and pollution control. When the electric field in the discharge gap is high enough to cause breakdown, in most gases a large number of microdischarges are observed, the so called filamentary discharge regime.

The principle of igniting (breakdown) and sustaining mechanism of the DBD can be summarized as follows [27, 28] and is schematically presented in Figure 2.7. As the alternating potential is applied to the electrodes, the dielectric material polarizes and induces the electrical field in the gap between the electrodes. This high ignition potential produces ionisation of the gas and the electrons and ions travel towards the electrodes charging them negatively and positively respectively, producing a decrease of the applied electrical potential that conducts to extinguish the plasma.

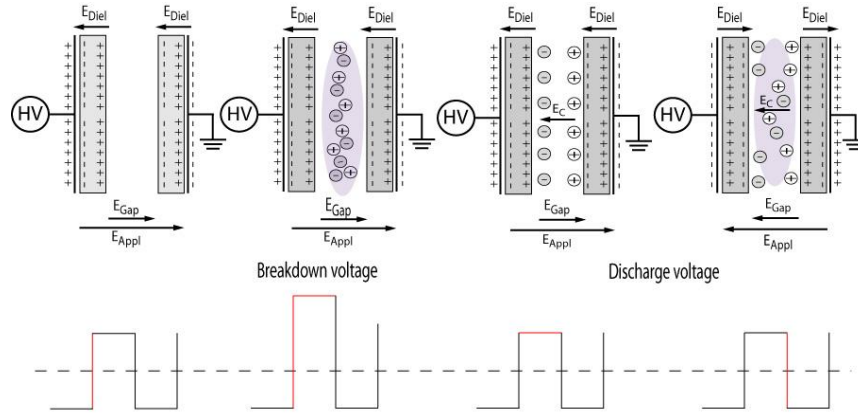


Figure 2.7 Principle of igniting and operating the DBD discharge

When the polarity of the potential is reversed, the applied potential and the memory potential due to polarization of the dielectric are added and the discharge starts again. Therefore the potential required to sustain the plasma is lower than that for ignition. Furthermore, the plasma ignites again automatically as a result of the charged dielectric. This memory potential formation by charge accumulation on the dielectric material represents an advantage of DBD in comparison with other electrodeless discharges. This memory potential decreases the breakdown potential and increases the potential applied to the discharge gas respectively. For some other types of plasma discharges using alternating potentials at higher frequencies like ICP, CCP and MIP this memory effect disappears and they require potential with much higher amplitudes. Some typical operation conditions for DBDs are summarized in Table 2.2 [29].

Table 2.2. Common operating parameters of DBDs.

Electric field strength for the first breakdown	$\cong 150 Td (p = 1 \text{ bar}, T = 300 \text{ K})$
Voltage $V_{pp}$	3–20 kV
Repetition frequency $f$	50 Hz–10 kHz
Pressure $p$	1–3 bar
Gap distance	0.2–5 mm
Dielectric material	Glass, $Al_2O_3$
Thickness $d$	0.5–2 mm
Relative dielectric permittivity $\epsilon_r$	5–10 (glass)...7000 (ferroelectrics)

The operating conditions of the DBD make them suitable for applications at pressure around atmospheric pressure or even in open air. Reviews dealing with atmospheric pressure discharges in general [23] and with DBD in particular [27, 29] make a classification of them and their applications. The most important applications of the

DBD are represented by the ozone generation (the first and still one of the most used applications), surface treatment for covering polymer foils or for changing the surface properties (wettability, receptivity, printability and adhesion) of different materials, reduction of pollutants in gas streams (volatile organic compounds, chlorofluorocarbons or diesel exhaust) and excimer lamps. The micro-DBD that received the most interest in the last time is the plasma display panel (PDP). This is an example of how microdischarges can be put in parallel in order to create large surface devices. PDPs larger than 100 inches having more than two millions of pixels are already on the market.

Also the atmospheric pressure DBDs are used in analytical domain [9, 30-32]. Mostly, in DBD using He as working gas, different elements like F, Cl, Br and I are determined after volatile compounds are decomposed, where characteristic emission wavelengths that are registered by a spectrometer. Another application of the DBD in analytical sciences is represented by the use of this as ionisation source incorporated in other devices as will be further presented. One of these sources is represented by the microplasma jet, also named as “plasma pencil” and “capillary discharge”. There are several research groups, as will be presented in the following, investigating this micro-DBD plasma jet and developing it for different other applications like in the fields of biomedical, material processing and analytics. A short overview on the plasma jet research field will be given in the next section.

The DBDs are capable to produce highly non-equilibrium plasma in a controllable way at atmospheric pressure and at moderate gas temperature. They provide high-energetic electrons which are able to generate excited atoms, ions and radicals. The common operational mode is the filamentary one, but under special conditions a diffuse one can be obtained too. They require no vacuum technique and no high voltages to maintain the discharge. Applications like surface treatment, ozone generation, cleaning of polluted gases, light sources have been largely industrialized based on DBDs. They have a great flexibility with respect to their geometrical shape, working gas mixtures and operational parameters. Taking into consideration the particularities of the DBDs, as presented above, it can be concluded that they represent a versatile alternative to other discharges and are suitable for a large area of industrial processes and improvement of life quality.

## 2.8 Atmospheric pressure plasma jets

One category of plasma discharges, incorporating at least two or even all the features that characterize the atmospheric plasmas, microplasmas and DBDs, described in the previous sections, is represented by the atmospheric pressure plasma jets (APPJ). There are several review articles summarizing the different approaches in developing such a plasma discharge jets, as well as their possible application [33-35]. This proves a real interest in such plasma sources. The possibility to produce non-thermal atmospheric pressure plasma capable to achieve enhanced gas chemistry without the need to increase the gas temperature represents an attractive feature of the plasma jets. This attractive characteristic led to an extensive use in applications that require low plasma temperatures, like those in material processing, biomedical or analytical applications [22, 36]. Also compared with some other atmospheric plasma sources where the plasma is mostly confined in the space between the electrodes or in some sort of containment enclosure, the plasma jet gives the possibility to launch the reactive species outside to an area not bound by anything.

Different research groups developed several plasma jets using DC or pulsed DC power sources in the kV range with signal frequencies in kHz domain and pulse widths in the range from nanoseconds to microseconds. As working gases mostly, Ar, He, N or mixtures of these with O are used. The construction of these plasma jets mostly consists of dielectric capillary tubes (fused silica, quartz) having one of the electrodes wrapped around it while the second, one in the shape of a rod is inside the tube [37, 38]. The polarization of the electrodes may vary: the inner electrode can be connected to high voltage while the outer ring is grounded [37], or the other way around [38]. Also construction with both electrodes inside a hollow Teflon tube [39], or one ring electrode around the capillary while the second one in shape of plate can be situated outside the capillary, a few centimetres away and grounded [16]. The gas flows are in the range of  $\text{L min}^{-1}$  and gas temperature of the plasma jet was reported to be up to  $100^\circ\text{C}$  and capable to be touched by bare hands [38]. The authors reported that such plasma jets could be used for treatment of surfaces.

Another type of AC driven hand-held plasma jet was developed by Laroussi and Lu [40]. As the construction of this device called “plasma pencil” was one of the starting



points in the development of the plasma jet, which is the subject of this thesis, it will be presented in more detail in the following. The device is different than those presented above. It consists of two thin copper ring electrodes attached to the surface of two centrally perforated alumina ( $\text{Al}_2\text{O}_3$ ) discs of 2.5 cm diameter and the central hole of 3 mm diameter, respectively. The copper ring electrodes have a bigger diameter as the alumina discs central orifice, but smaller than that of the discs. The electrodes are inserted in a dielectric cylindrical tube and the distance between them varies in the range of 0.3 to 1 cm. A schematic of the construction is presented in Figure 2.8.

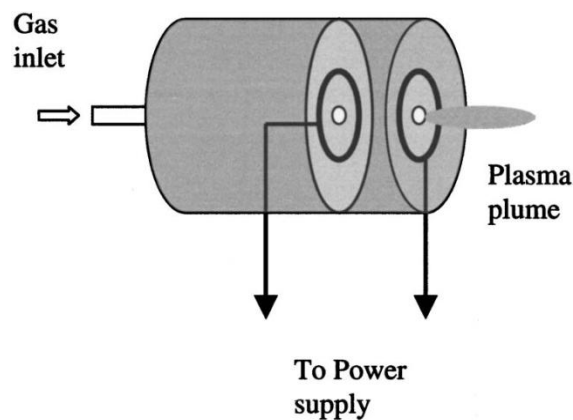


Figure 2.8 Schematic of the plasma jet developed by Laroussi and Lu [33].

The power supply consists of a high voltage pulse generator that can produce pulses with amplitudes up to 10 kV and widths between 200 ns to DC regime, at frequencies up to 10 kHz. The rise and the fall times of the voltage pulses are about 60 ns. When He or Ar are injected at the opposite end of the dielectric tube and the operating voltage is applied to the disc electrodes, a discharge is ignited in the space between the electrodes and a plasma plume/jet is launched through the hole of the outer electrode into the surrounding room air. Lengths of the jet up to 5 cm long and 3 mm diameter with gas temperature of 290 K were reported [40]. The current-voltage characteristics of the device presents three current pulses that occur per single voltage pulse and the authors sustain that the appearance of the second one after 100 ns is related to the launching of the plasma plume through the aperture of the device. Later the authors reported that the plasma jet was actually a train of small plasma bullets travelling at much higher speed than the gas flow (up to  $100 \text{ km s}^{-1}$  compared to the gas flow velocity of only  $8 \text{ m s}^{-1}$ ).

This plasma pencil was used to prove its potential biomedical applications by killing different types of bacteria. Since the diameter of the plasma jet is small, the treatment of samples is localized permitting good selectivity [41].

Another category of plasma jets are the AC-driven ones. Also in this case a dielectric material is used in the shape of a capillary tube on which two tubular electrodes are mounted [42], or one rod electrode is placed inside and the other is represented by a liquid solution in a tank surrounding the capillary [43], or even two concentric metal tubes with one of them covered in a dielectric material [44]. A so-called „corona DBD hybrid type discharge“ was also reported in this category [45] and consists of a needle inside a Pyrex tube and a dielectric plan electrode. In these cases, the applied voltages are in the range of few kV up to 80 kV [44] with frequencies from a few kHz up to 70 kHz [45]. The used gases are He and Ar with a flow from a few L min<sup>-1</sup> up to around 50 L min<sup>-1</sup> and plasma jets with lengths of several millimeters were reported, having temperatures between 300 and 500 K [43-45]. Plasma bullets with a speed of 15 km s<sup>-1</sup> were observed using an ICCD camera [42]. The authors reported that such plasma jets could be used for surface treatment, especially for changing the wettability of polymers [44, 45] and for degradation of organic compounds [43].

There are also many radio frequency (RF) driven plasma jets that have been developed in recent years. A short presentation of the most original ones, to which a large amount of work was dedicated, will be given. Most of them use RF sources of 13.56 MHz [34, 46-49], 13.05 and 7.17 MHz [48] and even 27.12 and 40.78 MHz [49]. The construction of these plasma jets has a cylindrical symmetry having an electrode like a needle (1 mm diameter) or a rod placed inside of a metal cylinder [34, 48] or a cylinder of dielectric material [46, 47, 49] which has wrapped around the second electrode. Also the inner electrode can have a pipe-like structure with 1-2 mm inner diameter [47], or it can be insulated by a glass sleeve and has a protruding tip of 0.3 mm diameter [48]. In all these configurations, the RF signal is applied to the inner electrode, while the second one is grounded. Also geometries with two ring electrodes wrapped around a quartz capillary tube (1 mm inner diameter) can be used [49] where one of the electrodes is powered, while the second one is grounded. As working gas for plasma production, mostly noble gases are used like He [34, 46, 48], Ar and molecular gases [49] at flows that can vary between several mL min<sup>-1</sup> [46] and several L min<sup>-1</sup> [34, 47-49]. Also liquids and

powders can be used [47]. Depending on the gas flow, plasma jets acquire lengths in the range of several millimeters. When He is used as working gas, the temperature of the plasma jet is close to room temperature [46, 48] up to few hundred grad Celsius [34] depending on the input power. When Ar is used with reactive gases, the temperature can reach up to 450 °C [46] or even  $7 \times 10^3$  °C [47]. The RF driven plasma jets are used for several applications like film deposition, material applications [34, 46, 49], biological applications [34, 46], decontamination of gases of chemical warfare [34], cleaning of archaeological artefacts [47], killing of bacteria and manipulation of cells [48].

Plasma jets produced using microwave powers (2.45 GHz) were also developed [50, 51]. These constructions are based on other macro-scale microwave plasma torches (MPT) [50] where the working gas flows through a capillary coaxially with the waveguide tube, or the gas flows between an inner conductor and an outer conductor that have a cylindrical configuration [51]. As gases, mostly Ar and N<sub>2</sub> are used at atmospheric pressure and flows from a several mL min<sup>-1</sup> [50] up to few L min<sup>-1</sup> [51]. The input power varies from low levels (2 W) [50] up to several hundred Watts [51]. The length of the obtained plasma jet varies from a few mm [50] up to several mm (aprox. 25 mm) depending on the gas flow [51]. The authors reported that these microwave microplasma jets can be applied in detection of gaseous species and as an element specific detector in gas chromatography [50], or for medical use as well as for surface processing, chemical vapour deposition and sprayer [51].

Rather small, mobile and easy to handle, APPJ units have to be considered for their capabilities. In recent years, a variety of applications has been realized using APPJs, and others may be still envisaged. The strength of vacuum-less plasma sources can be fully exploited, when the exhaust gas, which remains after the application, is harmless, and can be released to the environment without any further processing. This is valid when only steam or carbon dioxide is produced in addition to feedstock gases (like rare gases, oxygen, and hydrogen). Otherwise the exhaust gas has to be collected and processed, which will make the application more complicated and expensive. As long as the suction system does not require a full enclosure of the process, many advantages in respect to vacuum processes still remain. However many advantages are lost, when the application has to be performed in a closed chamber. As pointed out, APPJs are capable of producing charged particles, neutral metastable species, radicals and (V)UV

radiation, which can be used for example for biomedical applications. However, the charged particles are rapidly lost by recombination.

An overview of plasma sterilization using atmospheric pressure glow discharges (APGDs) was given by Laroussi [52]. In respect to the germicidal effect, the APPJ has very much in common with other sources of high-pressure non-equilibrium plasmas. It has been proved that APGDs can be efficiently used to inactivate bacteria. Hence, disinfection and sterilization of reusable, heat-sensitive medical instruments and implants is possible. Further possible biomedical applications would be the treatment of wounds and skin. The inactivation of biofilm-forming bacteria opens applications in the area of food safety [53]. Even the decontamination of chemical and biological warfare (CBW) agents using an APPJ has been proven [54].

Like other plasma based techniques, the APPJ can be used for the activation of surfaces, for example to make Teflon and synthetics wettable by improving the hydrophilicity. Also, a surface modification of biocompatible materials can be envisaged. An APPJ can also be used for the cleaning of surfaces by using air or oxygen highly diluted in a noble gas. The reactive oxygen species are capable to burn many organic materials with the release of  $\text{H}_2\text{O}$  and  $\text{CO}_2$ . The removal of spray paint from brick, the removal of ink from paper and removal of photoresist from silicon wafer has been also demonstrated by the group of Selwyn. Kapton and polyamide have been successfully etched [55, 56]. The etching of a variety of non-organic materials has been demonstrated as well [55, 57-59]. However, in this case, carbon tetrafluoride ( $\text{CF}_4$ ) was admixed to O containing noble gas, which makes the exhaust gas harmful. Etching of oxides like silicon dioxide ( $\text{SiO}_2$ ) and uranium dioxide ( $\text{UO}_2$ ), and of metals like tantalum (Ta), tungsten (W) and plutonium (Pu) was demonstrated.

APPJs were also used for plasma-enhanced chemical vapour deposition (PECVD) of a variety of coatings, as reported by review paper from Moravej and Hicks [60]. Glass and silicon dioxide ( $\text{SiO}_2$ ) have been successfully deposited by operating the APPJ with oxygen highly diluted in helium.

Considering the capacity of atmospheric pressure plasma jet to produce charged particles, neutral metastable species, radicals and UV radiation that are pushed outside due gas flow, rather than being bound to a confined volume, also the application in the

---

field of analytics can be envisaged. Such a research was conducted using a capillary dielectric barrier discharge (CDBD) capable to produce an atmospheric plasma jet using helium. Investigations to characterize the plasma as well as the use of this jet as an ionisation source were conducted and will be presented in the following chapters.



### 3 THE DIELECTRIC BARRIER DISCHARGES AS ANALYTICAL DETECTORS

#### 3.1 The dielectric barrier discharge as detector for laser absorption spectrometry

As already stated in the previous part, one of the applications of the DBD is represented by its analytical applications. It can be used as a detector for absorption atomic spectroscopy for different molecular compounds or as an ionisation source for other analytical devices as will be further described.

Such a micro-detector based on DBD was presented by Miclea et al [61-65] and it proved that it is a powerful microchip source for analytical spectrometry. The micro-detector consisted of two glass plates, each with a 50 mm-long aluminium electrode. The electrodes are produced by Al vapour deposition with a thickness of 0.1 mm, width of 1 mm and 50 mm length [66] and are covered by 20  $\mu\text{m}$ -thick glass layers, i.e. the dielectric layers. These are produced from glass powder melted on the electrodes. The distance between the electrodes, including the dielectric layers, is 1 mm. A 1 mm-wide discharge channel is formed by two glass spacers. The channel is 60 mm long and has

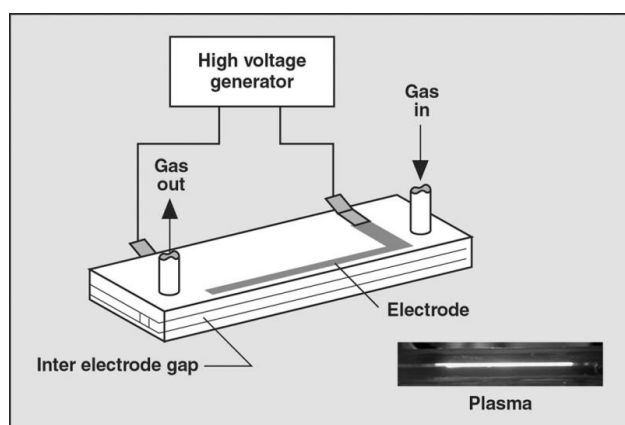


Figure 3.1 Linear dielectric barrier discharge for diode laser absorption spectroscopy operated at 5-20 kHz [65].

windows at each end. Additionally there are two connections for the gas input and output. A photograph of the discharge is presented in Figure 3.1. The discharge is characterized by small size, low electric power (less than 0.1 W), low gas temperature (approx. 600 K), and excellent dissociation capability for molecular species, for example  $\text{CCl}_2\text{F}_2$ ,  $\text{CClF}_3$ , and  $\text{CHClF}_2$ . It has

been used as excitation source for plasma modulation diode laser absorption spectrometry of excited chlorine and fluorine in noble gases and in air-noble gas

mixtures. The analytical figures of merit of the diode laser absorption spectrometry obtained with DBD are comparable with the results found earlier with DC and microwave induced plasmas of large size with much higher plasma powers. Detection limits of 400 ppt and 2 ppb for  $\text{CCl}_2\text{F}_2$  in He were found using the Cl 837 nm and F 685 nm lines, respectively. The DBD has provided excellent analytical results in diode laser atomic absorption spectroscopy (DLAAS) of halogenated hydrocarbons. This is because of the complete dissociation and efficient excitation of metastable atoms. Practical advantages of the DBD are the very low electrical power consumption and the simple power supply compared with other microchip plasmas. The gas temperature is low and the microchip is not thermally stressed. There is also negligible sputtering, which might be a problem in DC discharges. Therefore, long microchip lifetimes are expected, similar to those of DBDs in plasma displays. The distribution and diffusion of the excited atoms was measured with high spatial and temporal resolution. High-spatial-resolution plasma diagnostics of low-pressure DBD diode-laser absorption spectroscopy gave clear evidence of a thin, short-lived plasma layer approximately 40  $\mu\text{m}$  thick and 1 mm wide near the temporary cathode. In this thin layer plasma atoms are high efficiently excited, the gas temperature reaches approximately 1000 K, and electron density of greater than  $10^{15} \text{ cm}^{-3}$  can be found. In all other areas, the excitation is much less efficient, the gas temperature is near room temperature, and the electron density is below  $10^{14} \text{ cm}^{-3}$ . This means that most of the electrical power is used to heat a very small plasma volume. Although, the average power of the DBD is small (less than 0.1 W), in this volume the plasma should have an efficient dissociation capability not only for halogenated hydrocarbons, as shown in [65], but also for large molecules, at least for the main discharge period of approximately 10 ms. Diode-laser absorption measurements of excited chlorine in the low-pressure DBD filled with Ar and small concentrations of chlorinated hydrocarbons revealed the same spatial distribution as found for excited Ar. As a consequence, the measurements of halogenated hydrocarbons by diode-laser absorption spectroscopy of excited Cl or F as reported in [65] (the diode laser beam filled the whole space between the electrodes) can be significantly improved. The main absorption, however, was obviously caused by the small layers near the temporary cathodes. Approximate estimates give an improvement in the detection limit of at least one order of magnitude in comparison with the former experiment, if the



absorption measurements are only used for characterization, restricted to the small area of the plasma layer near the cathodes. This detector based on DBD absorption spectroscopy showed good limits of detection of molecular compounds containing Cl and F. Cl could be determined in the range of 400 ppt v/v and F in the range of 2 ppb v/v respectively. This micro-chip detector is limited in use only for those molecular compounds containing species that emit radiation corresponding to the laser diode wavelength, through radiative decay.

### 3.2 Atmospheric pressure microplasma cell as emission detector for organic compounds in gas chromatography

An atmospheric pressure microplasma cell was developed by Guchardi et al [67, 68]. The nature of this plasma source developed by this group is related to the microchip plasma based on a low frequency pulsed AC-source, using isolated electrodes as the one presented above by Miclea et al [65]. The arrangement of this micro cell consists of two cylindrical electrodes placed side by side on the fused silica capillary of 250  $\mu\text{m}$  inner diameter and 350  $\mu\text{m}$  outer diameter respectively. None of the electrodes is in contact

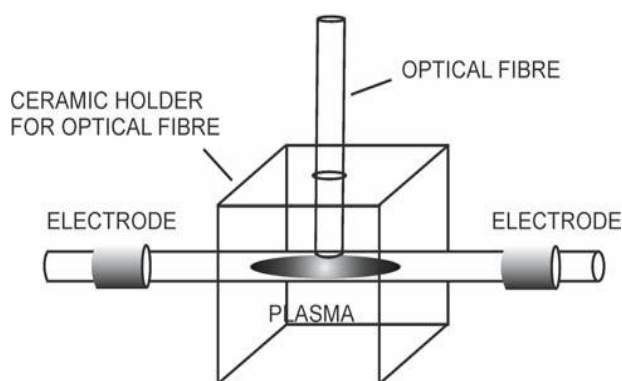


Figure 3.2 Capacitively coupled capillary plasma as optical emission detector for gas chromatography [13,68].

with the plasma which prevents deterioration of the electrodes and contamination of the plasma with electrode metal. The distance between the electrodes is 1 cm. The device was designed to work at 20 kV and 20 kHz by capacitive coupling of the energy into the capillary. A schematic of this device after Miclea et al [14, 69] is presented in Figure 3.2. Due to

the low frequency applied, this discharge can be considered as a DBD where the charges accumulated on the glass play a relevant role in switching of the discharge. The excitation temperature of the plasma determined from He emission lines is about 4000 K. Even though the authors did not present any temporally resolved emission of the plasma, it is expected that the excited species are pulsing with the frequency of the

field. This behaviour reduces the sensitivity of the detection. The microplasma can be supported at a flow rate range corresponding to most of common capillary chromatographic methods at atmospheric pressure, namely  $5 \text{ mL min}^{-1}$  and the applied power is 8 W. The microplasma was implemented as an on-column optical emission detector. The capillary column was placed directly in front of the plasma. The optical fibre was coupled directly above the capillary directing the emitted light to spectrometer. The plasma was self-ignited after the passage of the solvent through the capillary. The detection of Hg introduced as vapour has been demonstrated as well as that of Sb and As introduced in the form of volatile hydrides. It was also possible to detect molecular emission on the introduction of methane or carbon dioxide which could be used for quantitation. It was found possible to detect oxygen from its emission at 777 nm and 845 nm, hydrogen at 656 nm and sulphur containing species from emission at 923 nm [14]. The carbon-containing species  $\text{CH}_4$ , CO, and  $\text{CO}_2$  could be determined from an emission band at 385 nm due to CN. Detection limits in the range between about 1 and 10 ng were obtained using a miniature diode array spectrometer. The detection of organic compounds by monitoring the emission signals of C, Br, Cl, F, I, P, Se, and S separated in a He carrier gas was possible. In the case of halogens (F, Br, Cl, I) and S, these elements were measured by monitoring the emission lines at 685.60, 837.59, 827.24, 804.37 and 921.28 nm, respectively. The authors reported the determination of environmentally relevant halogenated volatile organic compounds and pesticides. The system showed the following detection limits: F 20, Br 0.3, Cl 0.1, I 158, and S  $6.6 \text{ pg s}^{-1}$ , respectively. These reported detection limits seem a little bit low for chromatographic peaks [69].

### **3.3 The first approach on the capillary dielectric barrier plasma jet discharge as ionisation source**

The capillary dielectric barrier plasma jet (CDBPJ), subject of this thesis, was first presented by Michels et al [70]. The construction is similar to the plasma discharges developed by Laroussi and Lu [40] and by Guchardi et al [67, 68] described in sections 2.8 and 3.2, respectively.

In this case one end of the capillary is left open to air and a plasma jet is established at the end of the capillary. He and Ar were used as working gasses. It is known that ionisation and fragmentation in the plasmas it is mainly caused by fast electrons and metastables atoms [71]. Based on this fact, the present plasma source was tested as an ionisation source for an IMS device. It was supposed that the excited He atoms on metastable states, getting out of the capillary due to gas flow, transport out energy which can further be used to ionize other atomic or molecular species. In this way such a plasma source can be suitable as ionisation source for other analytical devices like

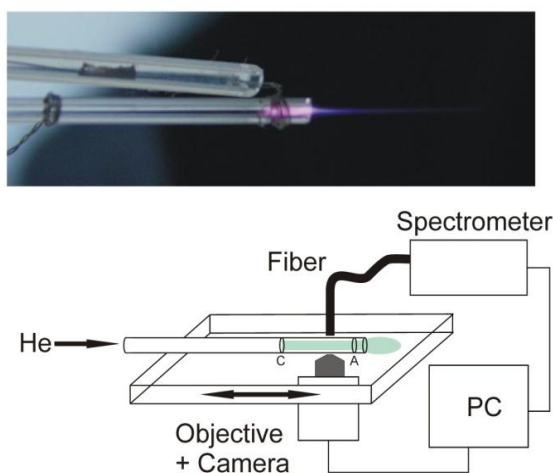


Figure 3.3 Photograph of the plasma source and the experimental arrangement for optical measurements [70].

mass spectrometers (MS) designed to operate at atmospheric pressure. A picture of the first dielectric capillary barrier discharge, tested as ionisation source, is presented in the Figure 3.3 [70]. The plasma jet outside the electrode region can be observed. Also the optical arrangement used for emission spectroscopy is presented. The discharge consisted of 3 cm long glass capillary with an inner diameter of 500  $\mu\text{m}$  and an outer diameter of

1.2 mm. Silver cables of 500  $\mu\text{m}$  diameter were wrapped around the capillary forming electrodes with a separation distance of 12 mm. The distance of the electrode to the end of the capillary was 2 mm. One electrode cable is isolated in order to prevent any discharge outside the capillary. He 5.0 which has a purity of 99.999% and an impurity of 3 ppm  $\text{N}_2$ , is used as plasma gas at atmospheric pressure. Three different flow rates of He (70, 350 and 750  $\text{mL min}^{-1}$ ) were established in the capillary. Unlike the DBDs used for diode laser atomic absorption spectroscopy, where the terminals of the power supply were ground free (the electrode voltage is changed between positive and negative voltage), here a periodic positive voltage pulse (5.5 kV with a frequency of 33 kHz and a pulse width of 2  $\mu\text{s}$ ) was applied. The discharge was initiated between the electrodes and a plasma jet outside the capillary, depending on the gas flow was obtained. The discharge capillary was mounted onto a movable stage of a microscope in

order to photograph the plasma light at certain positions. Side-on optical emission spectra at different positions along the capillary and plasma jet were taken with an Ocean Optics spectrometer (USB 2000) and a glass fibre (Ocean Optics QP 200-2-VIS-BX, 200  $\mu\text{m}$ ).

The first investigations on the capillary plasma jet were focused on the geometrical extension of the plasma jet in dependence on different electrode polarities and gas flow rates. He flow rates of 350  $\text{mL min}^{-1}$  and 750  $\text{mL min}^{-1}$  respectively, and with alternating polarities of the electrodes were used. In all the cases the plasma propagates outside the capillary as a plasma jet. For both He flow rates the plasma length outside the discharge is longer when the anode is at the outlet side. As the discharge is evaluated as an atmospheric pressure chemical ionisation (APCI) source for molecules at atmospheric pressure outside the capillary, the configuration with the anode at the

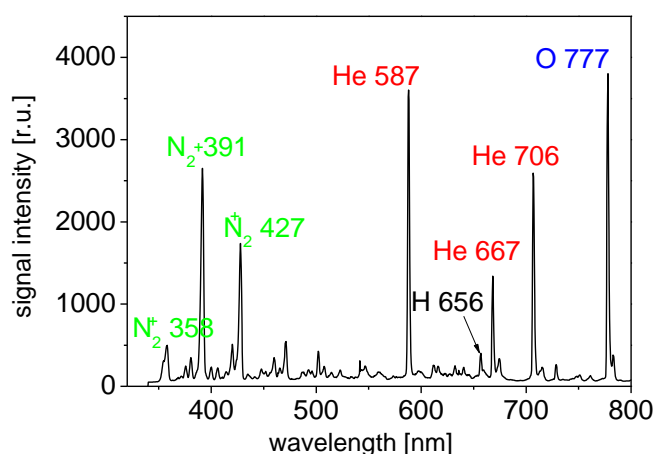


Figure 3.4 Characteristic emission spectra obtained in the vicinity of the electrode [70].

outlet end was chosen for further investigations. The length and the brightness of the plasma jet increases with higher flow rates. The processes occurring in the plasma, inside and outside the capillary were investigated by analysis of the optical emission spectra taken along the plasma propagation length in-between the electrodes and behind the anode outside the capillary. A representative emission spectrum acquired between the electrodes and close to the cathode region for a He gas flow of 70  $\text{mL min}^{-1}$  is given in Figure 3.4. The most intense lines were reported belonging to molecular ion lines of  $\text{N}_2^+$  at 358, 391, 427 nm originated from the impurity in the He 5.0, excited atoms of He at 587, 667, 706 nm and excited O atoms at 777 nm [72, 73].

It was found that the intensities of the observed lines strongly depend on the on the gas flow rate and the position of observation. As the electrodes were made of platinum wires of 100  $\mu\text{m}$  diameter wrapped around the capillary, this gave the possibility to acquire spectra also in the electrode region. The results obtained showed a spatial

dependence of He excited and O metastable states as well as the  $N_2^+$  emission lines. This can be observed from the graphs shown Figure 3.5. The associated photographs of the plasma discharge taken with a CCD colour video camera show the length of the electrodes, marked by a rectangle, and the outlet of the capillary, indicated by a line. Two maxima could be observed in the region of the cathode and of the anode, respectively.

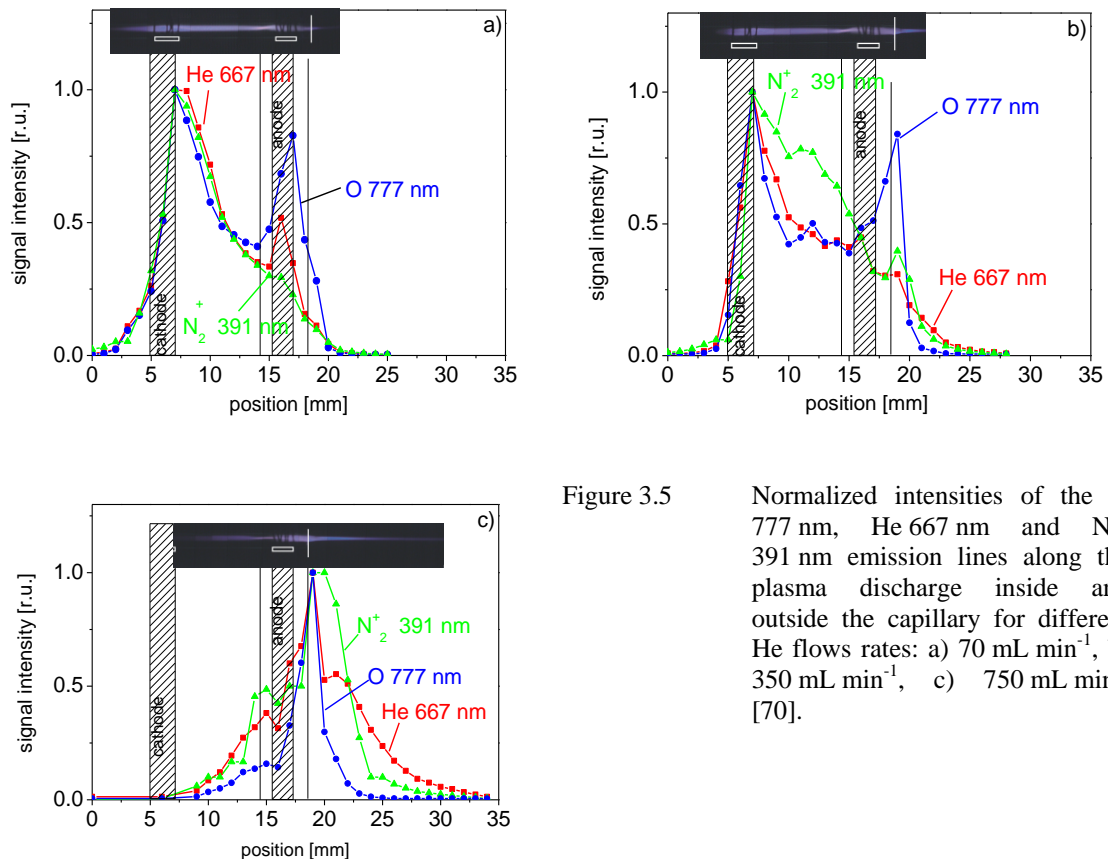


Figure 3.5

Normalized intensities of the O 777 nm, He 667 nm and  $N_2^+$  391 nm emission lines along the plasma discharge inside and outside the capillary for different He flows rates: a)  $70 \text{ mL min}^{-1}$ , b)  $350 \text{ mL min}^{-1}$ , c)  $750 \text{ mL min}^{-1}$  [70].

This characteristic resembles with the one presented by the DBD discharge applied for DLAAS [61, 63, 64, 74, 75], described in the beginning of this chapter. Such behaviour occurs in a glow discharge, where the negative glow is shifted towards the cathode when the pressure is increased. In that case the terminals of the power supply were ground-free (one electrode is negative while the other electrode is positive and vice versa), and consequently, the location of the absorption maximum switches from the vicinity of one electrode to the other, like in a glow discharge with changing polarities. In the present case of dielectric capillary barrier discharges, a periodic pulsed voltage

with a positive polarity is applied, and therefore, this discharge resembles a glow discharge periodically starting from the cathode side, like the above mentioned one.

Despite the dominant opinion that DBDs are Townsend discharges [76] and normally involve streamer breakdown like corona discharges, the question regarding the ignition of the breakdown is still open especially for the very beginning of the discharge [77]. This discharge has similarities to a glow discharge, with the left maximum correlating with the negative glow. The length of the cathode fall,  $d_c$ , covers the distance from the cathode surface up to the cathodic limit of the negative glow. It has to be underlined that the cathode zones are critical for sustaining the discharge because the ionisation and excitation takes place mostly in this region. If the distance between the electrodes is smaller than the length of the cathode fall, the discharge extinguishes because the electrons do not gain enough energy to produce ionisation even if the electric field is high [7]. Similar with the example presented in section 2.6 on microdischarges, for He the normal cathode fall should be between 60 and 180 V, while the  $p \cdot d$  (pressure dimension) product of the pressure and cathode fall thickness is about 1.3 Torr cm. Using this value, at 10 mbar the cathode fall thickness should be about 1.7 mm, at 100 mbar about 170  $\mu\text{m}$ , and at 1 bar about 17  $\mu\text{m}$ .

As the electrodes consist of wires with several coils wrapped around the capillary and have a spatial elongation of about 2 mm, they can be considered as hollow cathodes. Due to this aspect and the fact that the discharge was maintained under atmospheric pressure, the distance between the cathode and the negative glow is in the micrometer range, so the maximum emission intensity is located between the inner diameter and the center of the capillary in the radial direction inside the cathode. The distances calculated above (17  $\mu\text{m}$ ) and also observed (at the position of the cathode) are comparable with the conditions to be expected in DBDs. GD and DBD can be distinguished by the specific processes of electron production as explained in the following. In the case of a glow discharge, the secondary electrons are emitted from the surface of the metal cathode. In the case of the DBD, the secondary emission coefficient of glass is smaller than that of a metal surface so that the electrons cannot be emitted only from the glass surface of the dielectric layer, but they can be produced by ion-neutral collisions near the dielectric surface. It is obvious from the photos as well as from the intensities measured, inside and outside the electrodes, that the emission maximum shown in

Figure 3.5 a) is shifted towards the anode in Figure 3.5 b) and out of the region in between the electrodes in Figure 3.5 c).

In discharge tubes with diameters in the range of 5-20 mm this effect could not be observed. When the flow is about  $750 \text{ mL min}^{-1}$  and the diameter of the capillary is  $500 \text{ }\mu\text{m}$ , the velocity of an atom is about  $60 \text{ m s}^{-1}$ . Generally, the first maximum indicates the position of the negative glow. When the negative glow is transported away from the cathode, the electric field between the cathode and the negative glow (a positive space charge) would diminish drastically and the discharge should extinguish. But the discharge is not extinguished even when the negative glow has a distance from the cathode of a few millimetres (usually expected to be in the micrometer range). Therefore, the whole system, which is determined by the position where the electrons are created and the position of the negative glow, will be shifted in the direction of the anode and beyond. Since a discharge will not be extinguished when the positive column is eliminated the shifted system will support the discharge as long as the negative glow will not extend the position of the anode. This supports the assumption that the electrons are produced by ion-neutral collisions. In order to ionize the atoms of the buffer gas and therefore to produce electrons, the velocity of the ions calculated by the kinetic energy of an  $\text{He}^+$  ion, which is sufficient to ionize a He atom (24.56 eV), needs to be nearly 3 orders of magnitude higher than the velocity initiated by the flow of  $750 \text{ mL min}^{-1}$  ( $60 \text{ m s}^{-1}$ ). With a Paschen voltage of about 240 V and a ‘‘cathode fall thickness’’ of about  $20 \text{ }\mu\text{m}$ , which is the gap between the position where electrons are produced and the start of the negative glow, the velocity is given by:

$$\vec{u} = (e\lambda / 2m\bar{v})\vec{E} \quad (3.1)$$

where  $\lambda$  is mean free path,  $m$  the mass,  $\bar{v}$  the mean velocity and  $E$  the electric field of the  $\text{He}^+$ -ions which is sufficiently high to produce electrons.

When the ring anode with its radius  $R$  is regarded as a line charge, a field distribution along the electrode ring-axis of the capillary given by:

$$E_x = Qx / 4\pi\epsilon_0(R^2 + x^2)^{3/2} \quad (3.2)$$

is induced beyond both sides of the anode ( $E_x$  electric field along the axis,  $Q$  charge,  $R$  radius of the electrode ring,  $x$  position along the axis). Beyond the anode, the field

increases in the direction of the outlet and reaches its maximum at a distance  $L$  of  $R/(2^{1/2})=0.9\text{ mm}$  and decreases for  $L \gg R$  like the field of a point charge  $E_x = Q/4\pi\epsilon_0 x^2$ . Due to this field distribution, ions react differently than neutral species and atoms in excited states. In any case, all excited and ionised atoms and molecules will be de-excited by collisions outside the discharge region between the electrodes. As it can be seen from Figure 3.5 b),  $\text{N}_2^+$  reaches more out of the capillary than excited O due to the fact that  $\text{N}_2^+$  will be accelerated in the field behind the electrode.

Therefore,  $\text{N}_2^+$  de-excitation to  $\text{N}_2$  might be shifted in the direction of the outlet compared with the de-excitation of excited  $\text{O}^*$  or  $\text{He}^*$  atoms (position: 20 mm). In case of He, which is the buffer gas, the measurement identifies not only excited  $\text{He}^*$  atoms

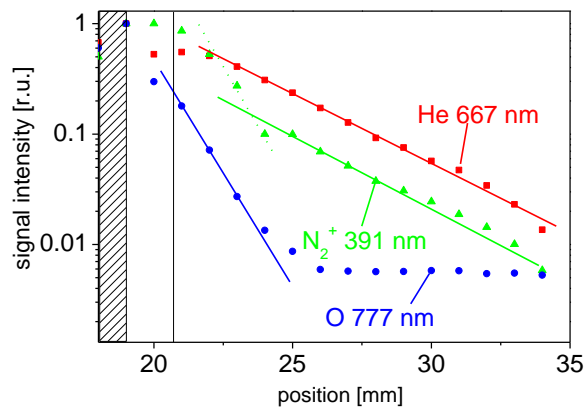


Figure 3.6 Spatial distribution of O 777 nm, He 667 nm and  $\text{N}_2^+$  391 nm emission intensities behind the anode for a gas flow of  $750\text{ mL min}^{-1}$  [70].

but also  $\text{He}_2^+$  ions, which are accelerated as well a  $\text{N}_2^+$  ions by the electric field. Due to the lower mass of  $\text{He}^+$ , the de-excitation to excited  $\text{He}^*$  states and the following de-excitation to metastable low level excited atoms may take place at a position even more shifted than the position where the de-excitation of  $\text{N}_2^+$  occurs (position: 21 mm). It can be seen that the slope of the  $\text{He}^+$  recombination is less steep than that

of  $\text{O}^+$  and  $\text{N}_2^+$ . Moving away 2 mm further the slope of  $\text{N}_2^+$  recombination is changed. This might be due to the fact that  $\text{N}_2$  molecules will be excited or re-excited by He excited atoms. This can clearly be seen in Figure 3.6, which reproduces a part of Figure 3.5 c) with the signal intensity on a logarithmic scale.

This graph shows a change of the slope at the position of 24 mm. For positions lower than 25 mm, the slope of  $\text{N}_2^+$  is parallel to the slope of  $\text{O}^*$  and the slope for positions higher than 25 mm has the same slope as the slope of  $\text{He}^*$ . This supports the assumption that the  $\text{N}_2^+$  recombination is definitely influenced by excited  $\text{He}^*$  atoms line outside the electrodes and the capillary.  $\text{He}^+$ ,  $\text{He}^*$ , and  $\text{N}_2^+$  extend from the capillary and are



directly or indirectly responsible for the production of protonated analyte ions as described above with the reactions proceeding in the corona discharge region during APCI or reactions initiated by a radioactive  $^{63}\text{Ni}$  foil in the IMS.

In order to test the possibility to use this plasma jet as a soft ionisation source, it was implemented on an IMS. The first results obtained using 2-heptatone as analyte at low concentration (ppb range) were presented. All the experiments were repeated 5 times with good reproducibility. In comparison with the conventional ionisation source that is used in IMS devices, i.e. the radioactive  $^{63}\text{Ni}$  foil, it was found that the IMS signal is 1.3 times higher when the plasma jet is used. The relative standard deviation of the reactive ion peak (RIP) signal height was less than 2% for the  $^{63}\text{Ni}$ -IMS and less than 4 % for the plasma-IMS. Considering that the same amplifier and electronics were used for the operation of both IMS, this can only be explained by a higher ionisation yield of the plasma ionisation source. Consequently, for a concentration of 55 ppb, dimer ions are still formed in the plasma-IMS, but no longer in the  $^{63}\text{Ni}$ -IMS for a similar concentration (50 ppb). Therefore, the plasma-IMS seems to be more sensitive than the radioactive  $^{63}\text{Ni}$ -IMS, a fact that is proven by the detection limits which were found in the range of 5 ppb for the plasma-IMS and of 20 ppb for the  $^{63}\text{Ni}$ -IMS, respectively.

### **3.4 The capillary dielectric barrier plasma jet discharge implemented as ionisation source for LC/MS**

As it was presented in the previous section, the capillary dielectric plasma jet proved to be a suitable ionisation source for the IMS. In order to test its ionisation sensitivity in comparison with other ionisation techniques, the plasma jet was also implemented for liquid chromatography/mass spectrometry (LC/MS) [78].

Coupling the liquid chromatography (LC) and the mass spectrometry (MS) represents one of the most powerful tools in analytical chemistry and gives important advances especially in biomedical and biochemical research. This was possible due to the intense basic research on developing new atmospheric pressure ionisation (API) techniques, which today offer a robust way to couple LC to MS. The main API techniques are electrospray ionisation (ESI) [79, 80], APCI [81, 82] and, less frequently applied, atmospheric pressure photoionisation (APPI) [83, 84].

These atmospheric pressure techniques differ in their ionisation process and their applicability [85]. Based on their working principle, these ionisation techniques are suited for different category of analytes. Also their selectivity and sensitivity differ. ESI for example, which is a highly sensitive method for analysis of large biomolecules [86] and has been also used for smaller organic molecules, being the most widely used API technique today. This is considered primarily a liquid-phase ionisation technique: preformed ions in solution are desorbed or evaporated to the gas phase and subsequently their mass can be analysed. The ionisation efficiency for more nonpolar compounds tends to be poor. For these compounds APCI and APPI are more suitable. In the case of APCI, which is considered to have some “harder” ionisation conditions than those in the ESI, the ionisation mechanism is primarily based on ion-molecule reactions in the gas-phase occurring between analyte molecules and a solvent-based reagent gas, generated by a series of ion-molecule reactions initiated by electrons from the corona discharge needle. Due to the short free pathway of ions at atmospheric pressure, ion-molecule reactions in the gas phase play an important role during the ionisation process. The ions undergo several collisions before reaching the mass analyzer. The high pressure liquid chromatography (HPLC) solvent is used as reactant gas and serves for the chemical ionisation of the analyte molecule. As an alternative to APCI-MS ionisation technique for nonpolar compounds, the APPI was introduced [83, 84]. This can be considered as a modified APCI source, where the corona discharge is replaced by a gas discharge lamp and other ionisation mechanisms are involved. In this case, the analytes will be ionised by resonant light excitation which in most cases is produced by a Kr discharge lamp. The analytes to be determined must have ionisation energies below 10.03 eV or 10.64 eV, corresponding to the wavelengths of the radiation emitted by Kr of 123.590 nm and 116.486 nm, respectively. Selective ionisation of the analytes may occur for common LC solvents [83]. The APCI and APPI ionisation techniques described above also have some disadvantages. In the case of APCI, the ionisation process takes place in a small volume around the needle of the corona discharge. The photoionisation process involved in the APPI technique mostly uses Kr as working gas. The two wavelengths of 116.486 nm and 123.590 nm, respectively, are in the vacuum UV range. This fact determines the absorption of the radiation in air yielding a low ionisation rate and also reactants with higher energy levels cannot be excited. Even

though a large concentration of easily ionising substance (dopant) can be used to produce the charge transfer to the analyte [83], there is no dopant capable to be used for all application, requiring always an individual optimisation for the involved working conditions.

An alternative to most ionisations techniques involved in the LC/MS can be seen in by the DBD, which can generate low temperature plasma at atmospheric pressure. Also the active region of the discharge is not confined in a small volume like in APCI and the ionisation mechanism involves highly excited states and not just a given radiation like in the APPI. Based on these facts, the dielectric barrier plasma jet discharge was implemented as ionisation technique on a LC/MS and tested on compounds possessing wide range of polarities. The latter is of particular importance for the application in metabolomics, where a broad range of metabolites (amino acids vs. lipids) have to be analyzed.

The microplasma discharge, which is the subject of this research, was implemented into a commercial API interface for LC/MS applications. A heterogeneous compound library was investigated by DBDI to illustrate the potential use of the miniaturised plasma as an alternative ionisation technique to ESI, APCI, and APPI.

The chemical compounds as well as the commercial LC/MS instrumentation are not described here as they do not represent the subject of this work, a detailed description of them can be found in the references [78].

The implementation of the dielectric capillary plasma jet discharge as ionisation source for LC/MS was realized by modification of a commercial API source (Ion Max source, Thermo Fisher Scientific), because it was anticipated that for efficient DBD microplasma ionisation, the HPLC eluent would require nebulisation and vaporization in the same manner as for APCI and APPI. Furthermore, this approach has the advantage that the new source could directly be connected to the mass analyzer without requiring a modification of the vacuum interface. Comparisons between the new source and the standard APCI and APPI source were also facilitated, because their housings were identical. Additionally, the ESI probe head fits into the same housing, which guarantees a similar geometry and hence comparability to DBDI, APCI and APPI, respectively.

Helium with a purity of 99.999 % at a flow  $150 \text{ mL min}^{-1}$  of was used as working gas to obtain the plasma jet at atmospheric pressure outside the capillary. Periodic positive high-voltage pulses of 5 kV in amplitude and  $2 \mu\text{s}$  pulse widths were applied on the electrodes at a frequency of 35 kHz. Details of the DBDI source used in this research are depicted in Figure 3.7.

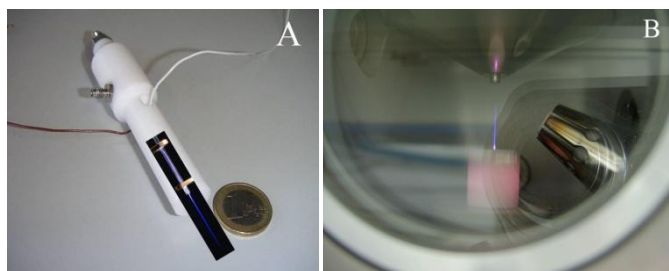


Figure 3.7 Photographs of the microplasma jet discharge implemented into the Ion Max source [78].

Figure 3.7 shows a photograph of the DBD with a plasma cone outside the electrode region. In order to show the inner arrangement of this discharge, a photomontage of the discharge and the housing is presented in Figure 3.7 A. The discharge consists of a 3 cm long glass capillary with an inner diameter of  $500 \mu\text{m}$  and an outer diameter of 1.2 mm. Rings with an inner diameter of  $500 \mu\text{m}$  are located around the capillary, forming electrodes with a separation distance of 12 mm. The distance of the electrode to the end of the capillary is 2 mm. The plasma electrodes are enclosed in a Teflon tube (see Figure 3.7 A) not only for safety precautions but also to prevent a discharge between the electrodes outside the capillary. For this Teflon tube, a probe head of polyether ether ketone (PEEK) was manufactured at the machine shop of ISAS for direct installation into the original API source housing. Therefore, only the window on the front side of the Ion Max source is replaced by the PEEK probe head. An installed O-ring within the PEEK body ensured proper fitting of the Teflon tube and easy adjustment of the distance to the mass spectrometer inlet. The position of the tube was on the same axis with the mass spectrometer inlet.

This ion source, like the unmodified APCI and APPI source, is working with a heated nebulizer (see Figure 3.7 B), which was maintained at  $450^\circ \text{C}$  for all experiments (except ESI).  $\text{N}_2$  (5.0, 99.999 %) was used to nebulize the liquid eluent (nebulizer gas) and also to transport the final dispersed sample droplets through the heated ceramic tube

in which they were vaporized (auxiliary gas). The ion current for the APCI and APPI experiments was set to 5  $\mu\text{A}$ . For ESI the capillary voltage was set to 4 kV.

Based on the assumption that the reactive species in the plasma jet are responsible for the ionisation process and the results on the microplasma jet discharge [70] described in the previous section, it was expected that it would serve as an efficient ionisation source for LC/MS. In order to prove this and to get more insight into the ionisation efficiency, a heterogeneous set of model compounds was investigated to evaluate the performance of DBDI in comparison to APCI, APPI, and ESI.

The displayed mass spectra showed that DBDI resulted in both protonated analyte molecules  $[\text{M}+\text{H}]^+$  and, for polycyclic aromatic compounds, analyte molecular ions  $[\text{M}]^+$ . With respect to different polarities, and, which is even more importantly, different ionisation energies and proton affinities, polycyclic aromatic hydrocarbons (PAHs) and functionalized anthracene derivatives were selected as model compounds. Therefore, a reversed-phase HPLC separation was carried out with subsequent ionisation and mass spectrometric detection. The instrumental limits of detection (LOD, signal-to-noise ratio  $> 3$ ) were determined by a dilution series. As expected, ESI is characterized by low ionisation efficiency for nonpolar compounds like the investigated PAHs. Even at the highest concentration level (of  $5 \times 10^{-5} \text{ mol L}^{-1}$ ), only six out of 13 model compounds could be detected. The pure hydrocarbons anthracenes were only barely detectable. The functionalized PAHs are more polarized and their ionisation efficiency is about 2 orders of magnitude higher compared to those of the pure hydrocarbons. The signal to noise ratios is even 4 times higher compared to those of DBDI and APCI.

By the use of APPI, almost all model compounds were detectable, except azulene and fluoranthene. In general, the signals for  $[\text{M}]^+$  are much more abundant compared to  $[\text{M}+\text{H}]^+$ . Interestingly, the  $[\text{M}]^+$  of 9,10-anthraquinone is not detectable, whereas the protonated molecule  $[\text{M}+\text{H}]^+$  gave intensities like in DBDI and APCI. In the present study, for all other model compounds, APPI gives less favourable LODs compared to APCI and DBDI. However, it is noteworthy that no dopant was used to assist the ionisation in APPI. Better LODs are expected by careful optimization of dopant usage (compound, concentration, flow-rate, etc.), but this was out of the scope of this work.

The detection of  $[M]^+$  was possible for all model compounds using APCI and DBDI. The ionisation efficiency of DBDI seems to be higher for compounds of small molecular weight (azulene, biphenylene, and acenaphthene) compared to APCI. The protonated molecules  $[M+H]^+$  of azulene, biphenylene, and fluorene were not observed by APCI and DBDI. In contrast to the PAHs of smaller molecular weight, the remaining compounds gave rise to intense protonated molecules  $[M+H]^+$ . In general, compounds covering a wider range of polarities can be ionised by DBDI better than by ESI. Ionisation efficiencies of DBDI for selected model compounds are quite similar to those of APCI, whereas dopant free APPI produced inferior results.

The dilution series of model compounds was measured three times by a LC/MS applying DBDI, APCI, APPI, and ESI. The relative standard deviations (RSDs) for multiple analysis ( $n = 3$ ) of identical solutions were determined and no significant differences between the used ionisation techniques were observed. Close to the LOD, the RSD is less than 15 % RSD, whereas at higher concentrations RSDs are less than 10%. This demonstrates that the new DBDI setup serves as stable ionisation technique for LC/MS (at least for 24 h).

The research conducted in this study demonstrates that the dielectric barrier plasma jet discharge can be used as a soft ionisation source for coupling HPLC to MS for several model compounds covering a wide range of polarities. The increased plasma volume in DBDI compared to APCI was expected to result in a larger fraction of ionised analytes, leading to improved sensitivity. However, the ionisation efficiencies seem to be very similar, as LODs for selected model compounds show only minor differences. This is due to the fact that only signals for  $[M]^+$  and  $[M+H]^+$  were considered. Signals obtained by DBDI of polycyclic aromatic hydrocarbons were distributed among several others mainly based on oxygen addition. Therefore, an increase of sensitivity is expected for a reducing of the amount of residual oxygen in the source and by optimization of the source geometry. In the DBD microplasma used in this study,  $He^M$ , which extends from the capillary, excites  $N_2^+$  by Penning ionisation and is directly or indirectly responsible for the ionisation of analyte molecules. In general, polar compounds are ionised preferentially by proton transfer in the DBDI source. These mechanisms are well-established for APCI using nitrogen (or air) as nebulising gas. However, ionisation of nonpolar compounds yields intense signals of molecular ions  $[M]^+$  in addition to the

protonated molecule  $[M+H]^+$ . Formation of molecular ions  $[M]^+$  can occur by direct ionisation in the DBD plasma, by charge exchange with other radical ions or conceivably by interactions with metastable species. The similarity of the obtained mass spectra by APCI and DBDI indicates an analogue basic principle of ionisation. Nevertheless, the DBD plasma is more reactive compared to corona discharge in APCI, because addition of several oxygen atoms and a nitrogen atom was observed for aromatic compounds. Furthermore, the degree of adduct formation with solvent molecules is more pronounced. Therefore, further studies are needed for deeper understanding of DBDI.





## **4 THE CAPILLARY DIELECTRIC BARRIER PLASMA JET CHARACTERIZED BY OPTICAL EMISSION AND ION MOBILITY SPECTROMETRY<sup>9</sup>**

Parallel to the experiments using the dielectric barrier capillary plasma jet as ionisation source for the LC/MS, as presented in the previous section, further investigations were carried out. In order to get more insight into the physical processes that take place in the plasma jet discharge as well as in the region surrounding the jet, three experimental arrangements have been used for the presented research. These together with the obtained results will be described in this chapter.

### **4.1 Experimental arrangements for the characterisation of the capillary dielectric barrier plasma jet**

First, an IMS was applied as a detector for the protonation by measuring the reactant ion signal. Second, an optical emission spectrometer was used to obtain information about the energetic levels which are involved in the ionisation mechanism. Third, both devices were combined in the ionisation chamber of the IMS.

The plasma jet tested as a soft ionisation source for IMS is based on a capillary dielectric barrier discharge (CDBD). It was realized using a 30 mm long glass capillary with an inner diameter of 500  $\mu\text{m}$  and an outer diameter of 1.2 mm from Hirschmann Laborgeräte. Two copper electrodes of 1 mm length surrounded the capillary at a distance of 10 mm from each other. A picture of the capillary and the electrodes together with the plasma jet established at the end of the capillary is presented in Figure 4.1. The electrodes are encapsulated in Teflon plates (1 mm thick), and also a Teflon spacer is mounted between these plates in order to prevent direct arcing between the electrodes outside the capillary.

---

<sup>9</sup> Parts of this chapter have been published with some modifications in *Characterization of a capillary dielectric barrier plasma jet for use as a soft ionisation source by optical emission and ion mobility spectrometry*, *Spectrochimica Acta Part B* **64** (2009) 1253-1258

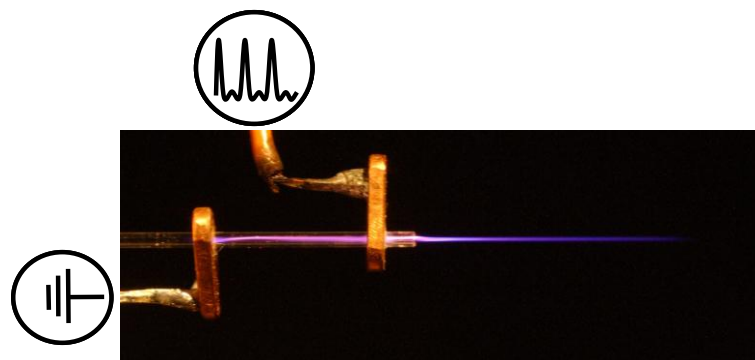


Figure 4.1 Plasma discharge established in the glass capillary between the electrodes and outside in open air.

The distance from the electrode (anode) to the end of the capillary was 2 mm. the working gas was provided at one end of the capillary, passing first the cathode and then the anode region with a defined flow, which is controllable between  $70 \text{ mL min}^{-1}$  and  $500 \text{ mL min}^{-1}$ . The gas leaves the other end of the capillary into the atmospheric environment. The electrodes were connected via isolated cables to a high voltage generator designed and built at ISAS [87]. A signal with a frequency of 20-35 kHz, a pulse width of  $2 \mu\text{s}$  and with an amplitude between 4 and 6 kV has been applied to the electrodes. As the discharge tube has a radial symmetry, the electrodes regions can also be considered as hollow cathodes. This fact leads to an increase of the collision rate between electrodes and atomic species, as electrons have a pendulum motion (hollow cathode effect) [88]. Due to the shortness of the microdischarge current pulses, the electron density is very high. This high electron density is responsible for the efficient dissociation of molecular species and for the excitation of metastable atoms [65]. A plasma jet was established at the end of the capillary as it can be seen in Figure 4.1. The length of the plasma jet depends on the gas flow and was observed in the range of 5 to 20 mm. For flows smaller than  $70 \text{ mL min}^{-1}$ , the plasma extinguished. For the spectral analysis of the plasma jet discharge a USB 2000 spectrometer (Ocean Optics) and an optical fibre  $600 \mu\text{m}$  UV/SR-VIS 190 mm-800 nm were used as shown in

Figure 4.3. As the portable Ocean Optics spectrometer has a limited resolution (1.5 nm FWHM), a certain overlap of the emission lines occurs. The spectra of the plasma jet were acquired end on outside the capillary with the optical fibre at a distance of 30 mm. He 5.0 (4 vpm  $\text{N}_2$ ), Ne 5.0 (2 vpm  $\text{N}_2$ ) and Ar 5.0 (5 vpm  $\text{N}_2$ ), as provided by the

supplier, were used as working gases. Different additional concentrations of  $N_2$ , in the range from 3 ppm up to 690 ppm were added.

## 4.2 Ion mobility spectrometry

The IMS technique is a rapid and sensitive method for detection of gas phase compounds [89]. The method was first applied for the detection of chemical warfare analytes, drugs and explosives. In recent years, the IMS is increasingly in demand for process control, food quality and safety [90, 91] and for medical applications [92].

The IMS was operated with an electric field of  $330 \text{ V cm}^{-1}$  applied on a drift distance of 120 mm and a shutter grid with an opening time of  $100 \mu\text{s}$ . Nitrogen was used as drift gas with a flow of  $200 \text{ mL min}^{-1}$ . The signal of the Faraday plate detector was amplified by a factor of  $11 \text{ nA V}^{-1}$ . The drift time spectra were detected with a length of 100 ms and a resolution of 50 kHz using a USB data-acquisition board developed at the ISAS. The plasma ionisation source was mounted radially to the drift flow in the ionisation chamber as it can be seen in Figure 4.2 [93].

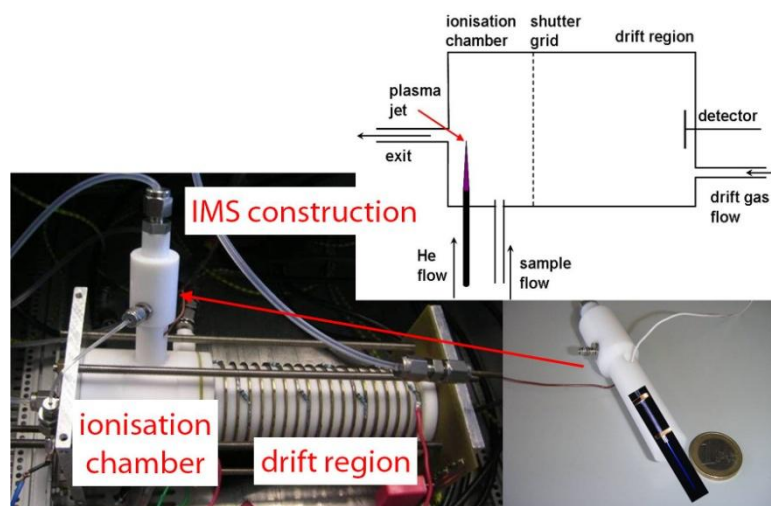
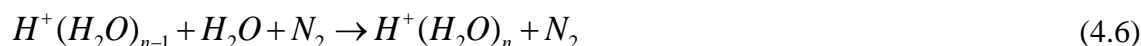


Figure 4.2 Picture and schematic of the IMS device with plasma jet implemented as ionisation source.

The ionisation mechanism called atmospheric pressure chemical ionisation (APCI) of the analyte molecules is done by charge transfer from the so-called reactant ions  $N_2^+$ , which generate protonated water clusters that finally ionise the molecules. The chemical reaction path is the following:



The protonated water clusters  $(H_2O)_nH^+$  are stable reactant ions and  $n$  depends on the humidity of the present gas. Then, ions of the protonated analyte are formed by gas-phase ion-molecule reactions of these charged cluster ions with the analyte molecules. This results in the abundant formation of  $MH^+$  ions, where  $M$  represents the analyte ion.

Once the ions are formed, they enter the pumping and focusing stage of a mass spectrometer in a similar way as the other API sources (for example ESI). They are moved by an electrical field towards the detector, represented by a Faraday plate. During their drift they collide with the drift gas molecules moving in the opposite direction, thus being decelerated. The collision frequency depends on their mass, charge and shape and therefore their drift time is a measure for their mobility, which is characteristic for the ion. The ion current is related to the concentration of the analyte in the ionisation region. The drift time of the ions in the present drift gas can be corrected to the pressure and the temperature of the drift gas, thus obtaining the so-called reduced ion mobility:

$$K_0 = (L / E \cdot t) \cdot (p / p_0) \cdot (T_0 / T) \quad (4.8)$$

where  $K_0$  is the reduced ion mobility (ion mobility  $K = L / (E \cdot t)$ ),  $L$  is the length of the drift distance (cm),  $E$  the strength of the electric field ( $V \text{ cm}^{-1}$ ),  $t$  the drift time (s),  $p$  the pressure of the drift gas in (hPa),  $p_0$  is the atmospheric pressure:  $p_0 = 1013.2$  hPa,  $T$  (K) the temperature of the drift gas and  $T_0 = 273.3$  K.

The most commonly used ionisation source for IMS is the radioactive  $^{63}\text{Ni}$  foil. In this case, the radiation ionises the available drift gas and the so-called reactant ions, the protonated water cluster like  $(\text{H}_2\text{O})_n\text{H}^+$  respectively which are obtained as presented in the chain reaction before [89] can be detected in the IMS. When the analyte is introduced into the ionisation region, the reactant ions transfer their charge to the molecules of the analyte, resulting in a decrease of the reactant ion peak (RIP) and an increase of the analyte peak. The IMS, on which the plasma jet was implemented and tested as ionisation source, was designed at ISAS [90]. The operational parameters of the IMS are given in the following table.

Table 4.1 Experimental parameters of the IMS designed at ISAS using the plasma jet as ionisation source.

Drift tube	12 cm length, 1.5 cm diameter
Electric field	$330 \text{ V m}^{-1}$
Grid opening time	$300 \mu\text{s}$
Drift gas	$\text{N}_2$
Drift gas flow	$100 \text{ mL min}^{-1}$
Sample gas	$\text{N}_2$
Sample gas flow	$150 \text{ mL min}^{-1}$

### 4.3 Optical emission spectroscopy

OES is a popular technique to investigate plasma discharges since it has no influences on the plasma parameters and information about the unperturbed plasma is obtained. The basic premise of this technique is that the intensity of the light emitted at particular wavelengths from an excited state is proportional to the density of the atomic specie in that excited state. Therefore, the measurement of the intensity provides a quantitative indicator of the concentration of the species involved in optical emission. The intensity can be converted into a quantitative relative or absolute number density of the species. For this, the electron energy distribution function and energy dependent cross section for the impact excitation (electrons, excited species and metastable states with the emitting species) are required to be known. In the gas discharge, the plasma species are subject to collisions with electrons and with other plasma species, like those described in the previous part. The excitation collisions and the subsequent radiative decay emit characteristic photons of the plasma species, which can be detected and analysed by

recording of the spectra. Experimentally, the spectral line of an element in a spectrum represents monochromatic images of the entering slit of a spectrometer when this is illuminated with the optical radiation. A spectral line is characterized by its integral intensity,  $I_\lambda$  as well as by its profile  $I(\lambda)$ , the first measure being the integral of the second:

$$I_\lambda = \int_{\lambda-\Delta\lambda}^{\lambda+\Delta\lambda} I(\lambda') d\lambda'. \quad (4.9)$$

Due to the fact that the excited atomic states have defined lifetimes  $\tau$ , the energetic levels corresponding to this states have a finite broadening given by the Heisenberg uncertainty relation:

$$\Delta E = \frac{h}{2\pi\tau}. \quad (4.10)$$

The only level with no broadening ( $\Delta E = 0$ ) is the ground level of fundamental state, because the life time of this state is very long. The broadening of the excited levels induces a corresponding broadening of the emitted optical spectral radiation. In the case of a transition from an excited level, having the corresponding broadening  $\Delta E$ , to the ground level the corresponding broadening of the emitted optical radiation is:

$$\Delta\lambda = \frac{\Delta E^2}{hc} \lambda^2. \quad (4.11)$$

This is called the natural broadening of a spectral line. Except this, there are also broadenings determined by collisions, Stark and Doppler effects.

According to classical electrodynamics, the natural broadening of a spectral line can be explained as follows: an excited atom emits electromagnetic dipole radiation for a specific time period  $\tau$ , and due to the damping of the oscillations, the light emitted in this way is not a strictly harmonic wave. Thus, the natural profile of the emitted radiation by such an oscillator with linear harmonic damping is given by the equation:

$$P(\nu) = \frac{I(\nu)}{I(\nu_0)} = \frac{1}{[4(\nu - \nu_0)]^2 + 1} \quad (4.12)$$

where  $I(\nu_0)$  represents the spectral intensity corresponding to the resonance frequency  $\nu_0$ ,  $I(\nu)$  represents the spectral intensity corresponding to the frequency  $\nu$ , and  $\tau$  is the mean lifetime of the excited state (the mean deexcitation time). As the period of the optical oscillations, which corresponds to the spontaneous atom deexcitation much smaller ( $\nu^{-1} \sim 2 \times 10^{-15}$  s) than the mean lifetime of these excited states ( $t \sim 10^{-7} - 10^{-8}$  s), the natural broadening of the spectral lines is mostly negligible small (the quality factor of these oscillators is very high ( $Q \sim 10^7$ )).

The total intensity of a spectral line  $I_\lambda$  is proportional to the energy density ( $W_\lambda$ ), emitted from the plasma in one unit of time as optical radiation, having the wavelength  $\lambda$ . Considering that the optical radiation having the wavelength  $\lambda$  is the statistical result of spontaneous emission processes of the plasma atoms from an excited energetic level  $i$  to an lower level  $j$ , one could express the corresponding emitted density energy as follows:

$$W_\lambda = n_i A_{ij} h \nu_{ij} = n_i A_{ij} hc / \lambda, \quad (4.13)$$

Where the values have the following meaning:  $A_{ij}$  is the Einstein coefficient for spontaneous transitions (represents the number of emitted photons by one atom through spontaneous emission in one second),  $n_i$  is the density of the atoms on the excited  $i$  level,  $h$  is the Planck's constant, and  $\nu_{ij}$  is the frequency corresponding to the transition from level  $i$  to level  $j$ . The  $A_{ij}$  coefficients have the dimension of a frequency, being equal with the inverse of the mean deexcitation times of the atoms on level  $i$  to a lower energy level  $j$ . The signal  $I_\lambda$  acquired by the detector can be expressed as following:

$$I(\lambda) = \eta(\lambda) W(\lambda), \quad (4.14)$$

Where  $\eta(\lambda)$  represents the transmission function of the system that takes into consideration the losses of optical radiation due to reflection and absorption in the system, the sensitivity of the detector, and the fact that only the radiation emitted in a certain solid angle is acquired. Thus, the integral intensity of a spectral line, given as the signal by the optical detector (spectrometer), can be expressed by the equation:

$$I(\lambda) = \eta(\lambda) n_i A_{ij} hc / \lambda. \quad (4.15)$$

Absolute measurements of the emitted optical power density can only be performed if the transmission function  $\eta(\lambda)$  of the system is known. This can be done by calibration of the optical system using a radiation source with known emission intensity. The emission intensity of these emitted photons of characteristic wavelengths provides information about the concentration of the plasma species.

#### 4.4 Experimental arrangement for optical emission spectroscopy

Since nitrogen plays an important role in the soft ionisation mechanism, the influence of nitrogen concentration in the discharge working gas was investigated by OES measurements. The experimental set-up for optical emission spectroscopy investigation is presented in

Figure 4.3. Also the electrical connection of the discharge electrodes to the plasma generator can be seen in the figure. An oscilloscope was used in order to permit the adjustment of the amplitude of the applied signal on the electrodes.

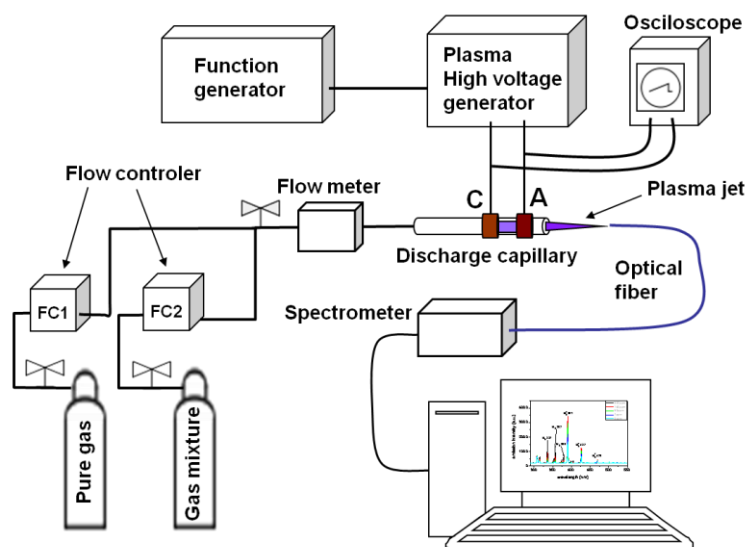


Figure 4.3 Experimental arrangement for spectroscopic analysis of the capillary dielectric barrier discharge using He, Ar and Ne as pure gases as well as mixtures of these with  $N_2$ .

The mixture of working gases was done by combining two gas flows supplied from two gas bottles (pure gas and gas mixture) in order to obtain different concentrations of  $N_2$  in He or Ar. One of the flows was the pure gas, He, Ne or Ar, while the other was He



with N<sub>2</sub>, Ar with N<sub>2</sub> or Ne with N<sub>2</sub>, respectively, with a maximum concentration of 690 ppm. The pressures in the gas bottles were the same and the flows were controlled by two flow controllers (FC1, FC2), adjusted in such a way, that the total amount of gas flow after mixing them is kept constant by measuring it with a flow-meter. Adjusting the two flow controllers, the concentration of N<sub>2</sub> in the working gas could be modified as described in the following. When FC2 was completely closed and FC1 was open, so that the flow-meter measured the required value (i.e. 500 mL min<sup>-1</sup>) there was only the N<sub>2</sub> concentration found in the supplied gases (He 5.0~4 vpm N<sub>2</sub>, Ne 5.0~2 vpm N<sub>2</sub> and Ar 5.0~5 vpm N<sub>2</sub>). When FC1 was completely closed and FC2 was open to have the same amount of gas flow as required, there was the working gas with the highest N<sub>2</sub> concentration (i.e. 690 ppm). So, by adjusting the two flow controllers different concentrations could be achieved.

## 4.5 Results and discussions

Since N<sub>2</sub> plays an important role in soft ionisation mechanisms produced by the CDBD according to the reaction chain presented above, the question arises, if the N<sub>2</sub> amount representing the impurity of the noble gas or if the N<sub>2</sub> molecules in air to which the plasma jet collides is relevant for soft ionisation. Therefore, besides He as buffer gas, Ne and Ar, as well as mixtures of these gases with different concentrations of nitrogen were applied. The ions formed under these conditions were detected by an IMS, furthermore OES measurements were performed.

The IMS measurements were carried out to detect differences in ion formation (reactant ion peak), when different gases were used as working gas in the plasma ionisation source. Ar, Ne and He were used with a flow of 300 mL min<sup>-1</sup>, at discharge voltage of 2 kV for He and Ne, and at a discharge voltage of 4 kV for Ar with a frequency of 30 kHz. The related drift time spectra of the IMS are presented in Figure 4.4. They show the so-called reactant ion peak (RIP), which is caused by the protonated water clustered (H<sub>2</sub>O)<sub>n</sub>H<sup>+</sup>. The small peak before the main-RIP might be ammonia or a small water cluster [94]. It was observed that the sharpest and highest peak is obtained in the case of He and a smaller one when Ne is used. In the case of Ar, no clear reactant ion signal could be measured under the given parameters, just a broad one with no distinct

peak. This is due to different energy levels and also different energy transfer paths from metastable states of He and Ne or from Ar ions that lead to protonation of water.

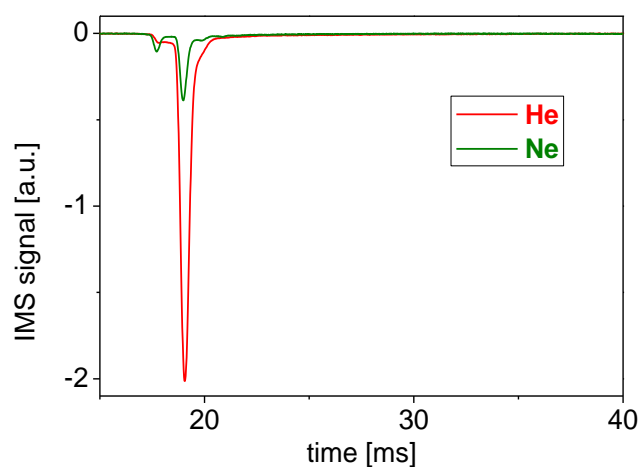


Figure 4.4 The IMS drift time spectra of the reactant ion peak when He and Ne are applied as working gases for the dielectric capillary plasma jet discharge.

Certain amounts of  $N_2$  were added to He 5.0, Ne 5.0 and Ar 5.0 in order to vary the concentration from low values, comparable with the impurity (present in the gas as provided by supplier) up to 690 ppm as mentioned before. The spectra of the plasma jet were acquired end on outside the capillary with the optical fibre at a distance of 30 mm. Characteristic spectra of He, Ne and Ar with nitrogen concentrations of 7 ppm and 140 ppm are presented in Figure 4.5. The spectra are divided into a left part from 300 nm to 500 nm and right part from 580 nm to 850 nm. The part in between these regions contains no lines which are significant for this research. On the left side, accentuated by a blue frame in the range from 380 nm to 500 nm, characteristic spectra of the  $N_2^+$  first negative system with lines at 391 nm (0,0) 427 nm (0,1) and 470 nm (0,2), are shown. They can only be measured when He is applied as buffer gas. In the wavelength range between 300 nm to 380 nm, the  $N_2$  second positive system with lines at 337 nm (0,0), 357 nm (0,1) and 380 nm (0,2) are given. On the right side of the spectra the characteristic lines of the noble gases are presented. The slight deviations of the emission lines in the spectra are within the uncertainty of the spectrometer.

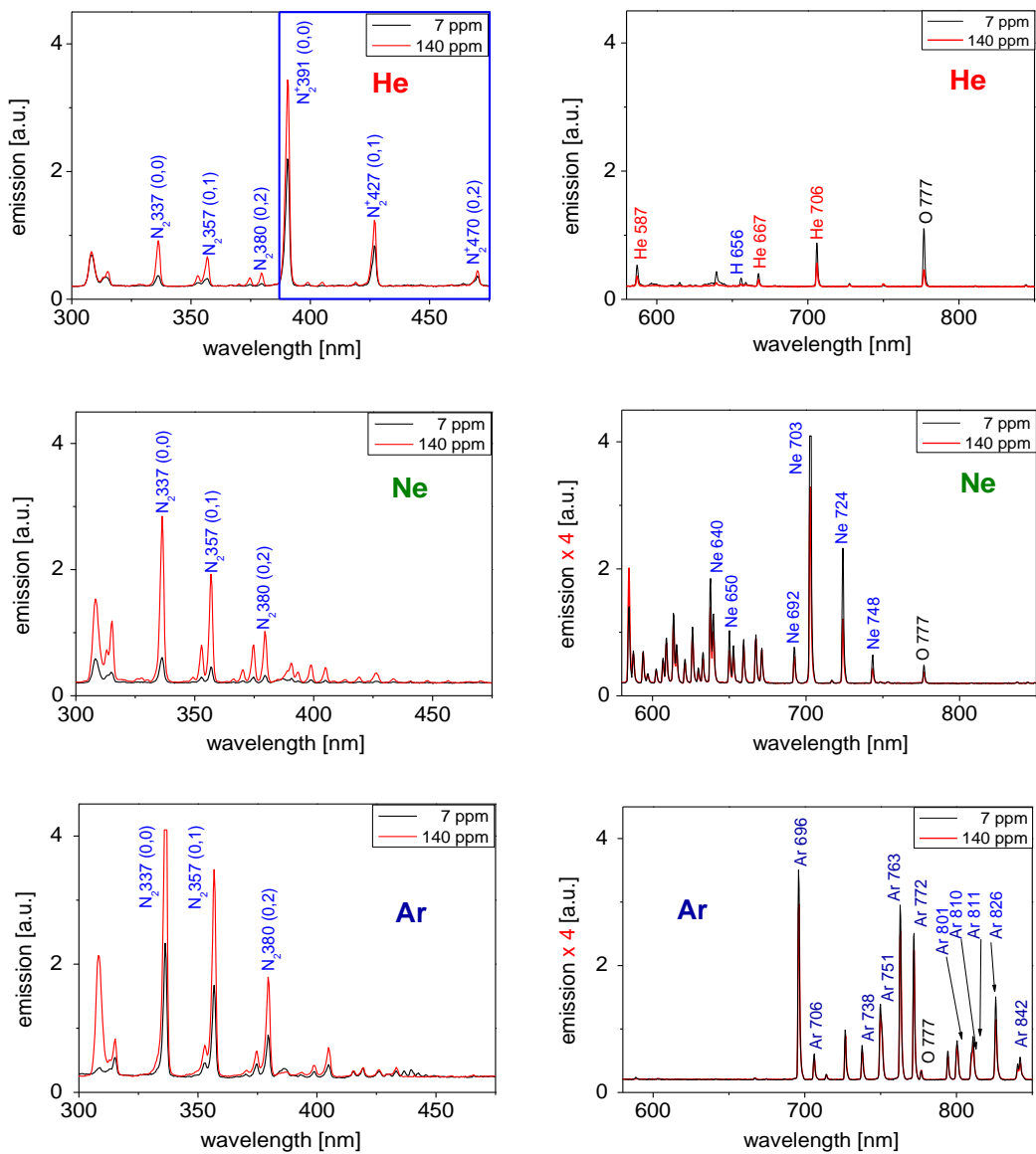


Figure 4.5 Optical emission spectra of He, Ne and Ar as working gases in the dielectric capillary plasma jet discharge. The blue frame indicates the characteristic spectra of the  $N_2^+$  first negative system. The intensities of the specific Ne and Ar spectra are divided by 4 in order to be represented in the same scale as  $N_2^+$  lines.

The *He* lines observed in the discharge correspond to the following electron transitions (Paschen notation):  $3d^3D_{3,2,1}-2p^3P^0_{2,1,0}$  for 587 nm,  $3d^1D_2-2p^1P^0_1$  for 667 nm, and  $3s^3S_1-2p^3P^0$  for 706 nm and have the energy in the range between 20.96 eV-21.22 eV ( $169086\text{ cm}^{-1}$ - $171135\text{ cm}^{-1}$ ) for the lower level and 22.71 eV-23.07 eV ( $183236\text{ cm}^{-1}$ - $186101\text{ cm}^{-1}$ ) for the upper level, respectively, as shown in Figure 4.6.

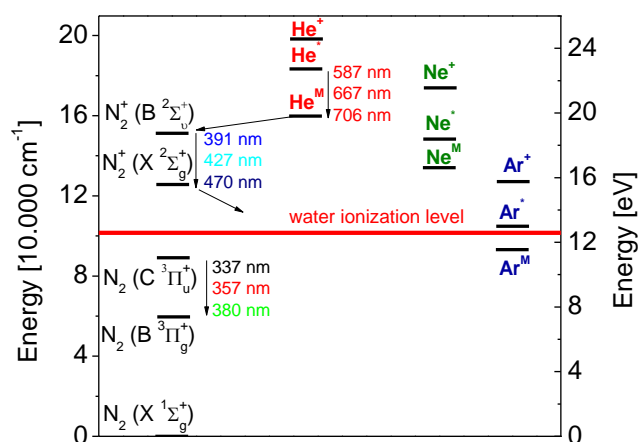
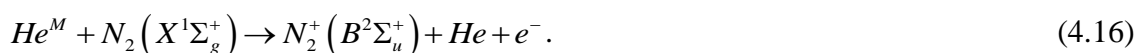


Figure 4.6 Energy transition levels of He, Ne, Ar and N<sub>2</sub> and the water protonation level [94].

The neon lines that appear in the discharge are in the range of 580 nm – 800 nm and correspond to the transitions between 2p<sub>1-10</sub> to 1s<sub>2-5</sub> electron configuration (Paschen notation) and energy differences between 18.38 eV-18.96 eV to 16.62 eV-16.85 eV respectively. Ar exhibits a spectrum pattern with many intense emission lines in the wavelength range of 700 nm – 950 nm that are assigned to the transitions between 2p<sub>1-10</sub> (12.09 eV-13.48 eV) and 1s<sub>2-5</sub> (11.55 eV-11.83 eV).

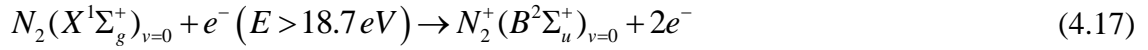
In the case of He, the N<sub>2</sub><sup>+</sup> first negative system lines (391 nm and 427 nm) are initiated by transfer of the energy from the metastable states. This can be proven by the fact that the emission lines of He decrease when the concentration of nitrogen is increased (Figure 4.5). Meanwhile, the lines of the N<sub>2</sub> second positive system (337 nm and 357 nm) increase. In the case of Ne and Ar this cannot be observed. In contrast, the lines of the N<sub>2</sub> second positive system are increased. The emission lines (391 nm and 427 nm) of the N<sub>2</sub><sup>+</sup> first negative system correspond to the transition between N<sub>2</sub><sup>+</sup>(B<sup>2</sup>Σ<sub>u</sub><sup>+</sup>)→N<sub>2</sub><sup>+</sup>(X<sup>2</sup>Σ<sub>g</sub><sup>+</sup>). These transitions cannot be initiated in plasmas at atmospheric pressure in pure N<sub>2</sub> [95], but it is however, a strong transition in He/air or He/N<sub>2</sub> mixtures due to Penning ionisation:



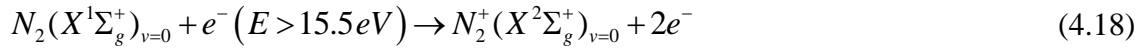
This reaction is almost resonant. The He metastable states He<sup>M</sup> are created by direct electron–atom collisions that produce excited atoms followed by cascade transitions from higher states to E<sub>lowest metastable</sub> = 19.81 eV. The N<sub>2</sub><sup>+</sup>(B<sup>2</sup>Σ<sub>u</sub><sup>+</sup>)<sub>v=0,...,5</sub> energy levels are between 18.73 eV and 20.11 eV (Figure 4.6).

Direct electron excitation of  $N_2^+(B^2\Sigma_u^+)$  is possible from the ground state of  $N_2^+(X^1\Sigma_g^+)$  and  $N_2^+(X^2\Sigma_g^+)$  with  $E_{\text{threshold}} = 18.7 \text{ eV}$  and  $3.2 \text{ eV}$ , respectively in two different ways:

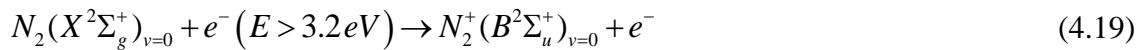
a one step process:



or in a two step process:



and then:



This probably takes place during the initial increase and the early decay of the current pulse; while in later phases  $N_2^+(B^2\Sigma_u^+)$  is populated only by Penning ionisation as described above. The subsequent radiative decays emit characteristic photons of the first negative band head at a wavelength of 391.4 nm with an intensity proportional to the population of the  $N_2^+(B^2\Sigma_u^+)_{v=0}$  state [95].

Optical emission measurements using different ratios of nitrogen in pure He gas were accomplished in order to study the influence of the He metastables on the emission lines of the  $N_2^+$  first negative system and the  $N_2$  second positive system. Figure 4.7 shows the normalized emission intensity variations of some prominent He emission lines (667 nm, 586 nm and 706 nm), representing transitions from different excited states ending on metastable states. Also the 656 nm H line and the normalized emission intensities of the two strongest lines of the  $N_2^+$  first negative system (391 nm and 427 nm), as well as the  $N_2$  second positive system (337 nm and 357 nm) are presented in dependence on the concentration of nitrogen in helium.

The  $N_2^+$  first negative system lines increase whereas the He lines decrease with increasing  $N_2$  concentration up to a value of 140 ppm. Several measurements with  $N_2$  concentrations between 140 and 600 ppm were accomplished and the maximum was always between 140 ppm and 450 ppm. When the maxima of the emission intensity of the  $N_2^+$  first negative system lines are reached, the intensities of the He lines decrease. The maximum of the  $N_2^+$  first negative system lines at 140 ppm nitrogen in He indicates

that the population of  $N_2^+$  is comparable with the population of He metastables. With concentrations higher than 450 ppm, the intensity of the  $N_2^+$  first negative system lines and the He lines should be constant beyond the maximum. The amount of  $N_2^+$  cannot be higher than the amount of He metastables, which deliver the energy for the Penning ionisation.

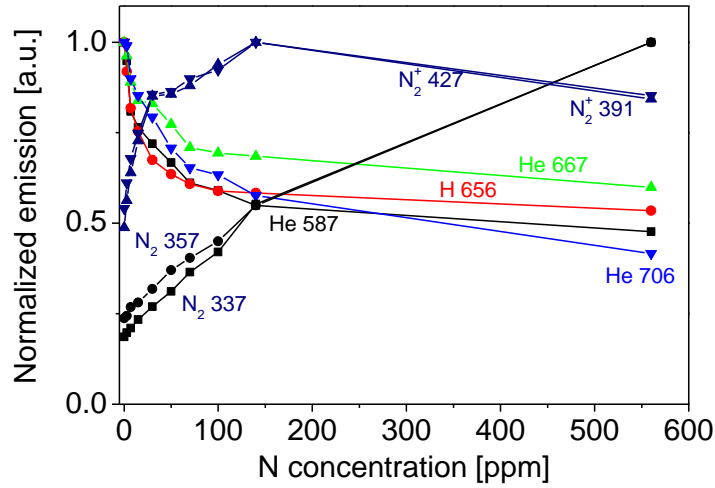
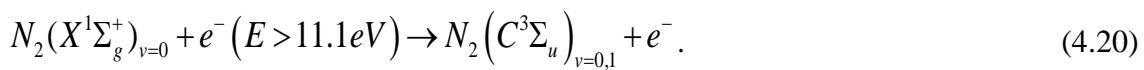


Figure 4.7 Normalized intensities of He,  $N_2$ ,  $N_2^+$  and H emission line variation with respect to the  $N_2/He$  ratio.

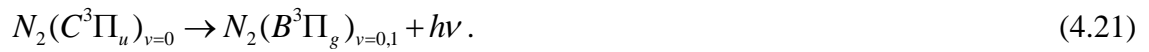
However, Figure 4.7 shows a decrease of these lines with slopes which are nearly parallel. This is due to the fact that the plasma conditions are changed with higher concentration of nitrogen and therefore the amount of metastables is decreasing. The change of the plasma conditions can be explained by the quenching of the electron temperature with the introduction of  $N_2$  due to its lower ionisation potential relative to He.

The 337 nm and 357 nm emission lines of the second positive system of molecular nitrogen correspond to the following transition  $N_2(C^3\Pi_u) \rightarrow N_2(B^3\Pi_g)$  [95]. The upper level population of the  $N_2(C^2\Pi_u)$  state is mainly populated through direct electron impact excitation from the ground state with threshold energy of 11.1 eV. Therefore, the production rate of the upper level of the transition is a function of the  $N_2$  population:



Another population mechanism is the decay from the  $N_2^+(X^2\Sigma_g^+)$  to the  $N_2(C^2\Pi_u)$  state.

The subsequent radiative decays emit characteristic photons of second positive band head, having wavelengths of 337 nm and 357 nm:



The slope of the lines belonging to the  $N_2$  second positive system changes at a  $N_2$  concentration of 140 ppm when the radiative decay from the  $N_2^+(X^2\Sigma_g^+)$  state to the  $N_2(C^2\Pi_u)$  state ends due to the limited energy transfer from He metastables to the  $N_2^+(B^2\Sigma_u^+)$  state. Optical emission measurements were also accomplished perpendicular to the axis of the plasma jet. Similar results were found concerning the maximum OES signal in dependence on the concentration.

He with an increasing concentration of  $N_2$  impurities in the discharge gas lead to smaller IMS signals. Therefore, the most sensitive IMS signal can be obtained with pure He. In the following, the experimental arrangement for the optical emission measurements was accomplished in the ionisation chamber of the IMS. The plasma jet is integrated radial to the IMS tube as shown in Figure 4.2. On the opposite side, the optical fibre was integrated into the ionisation chamber in order to measure emission spectra end on the plasma jet. The diameter of the ionisation chamber is 10 mm, the plasma jet inside has a length of about 9 mm and the distance between the fibre probe and the end of the plasma is 1 mm. The drift gas is perpendicular to the plasma jet and the optical fibre. Figure 4.8 shows the IMS signals when plasma jets with different efficiencies are used. The plasma was operated in different modes initiated by different applied voltages and frequencies. Surprisingly, the mode generated with a lower voltage of 5 kV and frequency of 33 kHz is more efficient for IMS than the mode generated by voltage of 7 kV and 42 kHz. The red line presents the lower and the black line the higher efficiency as it can be seen in Figure 4.8 a. The corresponding spectra, which are given below, are divided into two regions: Figure 4.8 b from 280 nm to 500 nm for the  $N_2$  second positive system and the  $N_2^+$  first negative system emission lines, and Figure 4.8 c from 550 nm to 800 nm for He lines. The intensities of the He lines decrease, and the lines of the  $N_2$  second positive system increase, when the IMS signal increases or the plasma jet works in a low efficiency mode.

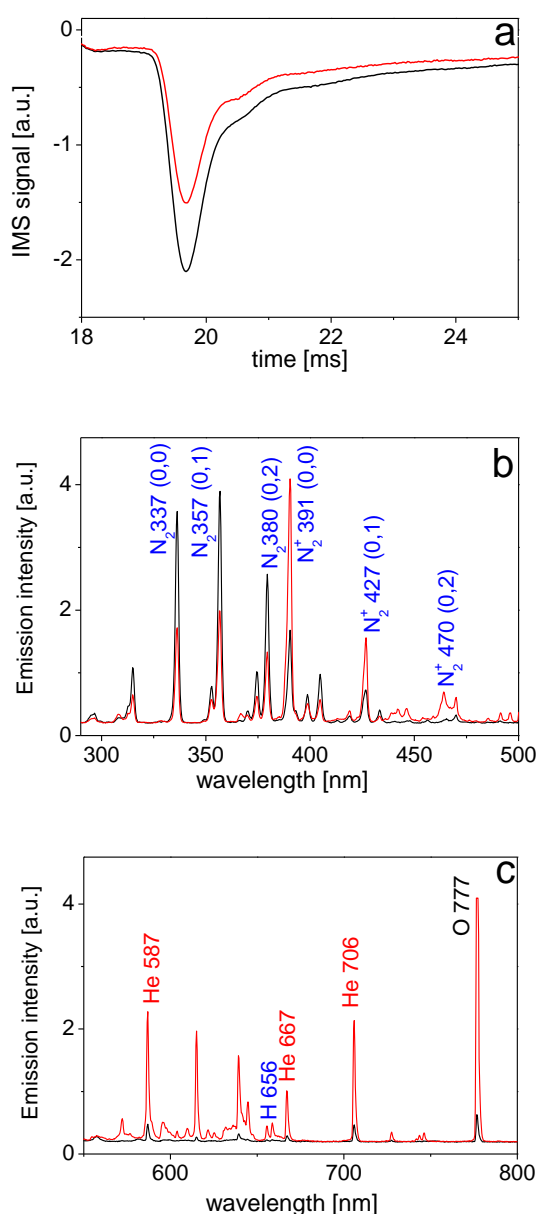


Figure 4.8 IMS drift time spectra (a) and emission spectra (b, c) when He capillary dielectric plasma jet is used with different ionisation efficiencies due to different generator operating parameters (black line: high ionisation efficiency with 5 kV and 33 kHz; red line: low ionisation efficiency with 7 kV and 42 kHz).

On the other hand, the  $N_2^+$  lines decrease even below the level of the lines measured with the plasma jet with a low efficiency. The emission from  $N_2^+$  bandhead at 391 nm and  $N_2$  bandhead at 337 nm should be proportional to the excited state population. Usually the ratio of the signals at 391 nm and 380 nm is  $>1$ , which is the case of spectrum plotted in red with lower ionisation efficiency. In the case of the higher ionisation efficiency, the ratio is smaller than 1. Therefore, the main part of the energy of the lower state of the first negative system is used for the protonation of water



molecules [94] and correspondingly the IMS RIP signal increases. When the energy is transferred from the lower level of the  $N_2^+$  first negative system, to the water molecules to protonates them and the RIP signal increases. In the same the emission intensity of the  $N_2$  lines decreases. With the recombination of  $N_2^+$  ions the population of the upper second positive state and therewith the optical emission of the second positive system will be increased. Considering the results obtained from IMS measurements as well as those from OES it can be concluded that the water protonation process is initiated by energy transfer from He metastable states to  $N_2^+$  excited state and then to water.

## 4.6 Conclusion

Nitrogen plays an important role for soft ionisation mechanisms using the capillary dielectric barrier discharge. Nitrogen can be excited to the upper level of the  $N_2^+$  first negative system ( $B^2\Sigma_u^+$ ) by Penning ionisation due to the He metastables. Therefore, the population of the excited upper level of  $N_2^+$  first negative system ( $B^2\Sigma_u^+$ ) cannot exceed the population density of the metastables. This density is between 140 ppm and 450 ppm of the ground state He atoms. In order to optimize the IMS sensitivity, pure He should be used. The reaction of Penning ionisation should occur in the vicinity of the protonation process. This means that the Penning ionisation between He metastables and nitrogen should happen in the ionisation chamber outside the plasma capillary in the vicinity of the plasma jet. The small RIP observed with the Ne gas discharge can only be explained by Penning ionisation, but the energy difference between Ne metastable state and the protonation level is bigger than the difference between  $N_2^+(X^2\Sigma_g^+)$  and the water protonation level. In the case of Ar, the metastable state is lower than the protonation level and therefore the RIP could not be measured.

The measurements performed and the results obtained shown that the best results were achieved when He was used as working gas for the microplasma jet ionisation source, and that  $N_2$  plays an important role in the energy transfer to protonate water. In the following chapter, a detailed investigation of these two gases and their species distribution along the plasma jet will be presented.



## 5 SPATIALLY RESOLVED SPECTROSCOPIC MEASUREMENTS OF THE CAPILLARY DIELECTRIC BARRIER PLASMA JET<sup>10</sup>

Based on the previous results that showed a connection between the working gas of the plasma jet and the presences of  $N_2^+$  specific emission lines in the observed spectra, further investigations were necessary. He showed to be the best-suited gas to be used for the implementation of the plasma jet as ionisation source for the IMS device, where the mechanism of the reaction chain involves the presence of  $N_2^+$ . These facts directed the research focus to the connection between the reactive species of these two gases. For this purpose an optical emission mapping of the plasma jet was accomplished and a spatial resolved distribution of the reactive species was provided.

### 5.1 Experimental arrangement for plasma jet mapping

For the jet mapping measurements, the plasma discharge was produced using the CDBD construction presented in the previous section with some improvements. The electrodes are encapsulated in Teflon plates to prevent direct arc discharges between them. The distance from the open end of the capillary to the first electrode (the anode) is approximately 2 mm. The whole construction, consisting of capillary, electrodes and connecting cables, is encapsulated in a Teflon cage. A schematic of the capillary, the electrodes connections and Teflon cage is presented in the top part of Figure 5.1. The plasma jet is obtained using He as working gas which is provided with two different gas flow rates  $F_A = 300$  and  $F_B = 1000 \text{ mL min}^{-1}$ . The electrodes are connected through isolated cables to a high voltage generator constructed at ISAS [87]. A function generator providing rectangular pulses of 2  $\mu\text{s}$  width modulates the signal applied to the electrodes. The corresponding values for stable plasma are 6 kV at 20 kHz. Depending

---

<sup>10</sup> Parts of this chapter have been published as they are here presented or slightly modified in *Spatially resolved spectroscopic measurements of a dielectric barrier discharge plasma jet applicable for soft ionisation*, Spectrochimica Acta Part B **66** (2011), doi:10.1016/j.sab.2011.03.005.

on the gas flow rate, the lengths of the plasma jet are of 10 and 20 mm for the 300 and 1000 mL min<sup>-1</sup>, respectively.

The plasma jet mapping was performed by optical emission spectroscopy. The principle of this technique was presented in the previous chapter. For this purpose an USB4000 spectrometer in the visible range (300 - 956 nm) and an optical fibre 600 µm UV/VIS 300 - 1100 nm from Ocean Optics were used together with OOIBase32 software. The optical arrangement applied for plasma jet mapping is presented schematically in Figure 5.1. The top view of the plasma jet, the focusing lens ( $f = 10\text{ mm}$ ) and the entrance of the optical fibre are depicted in the upper part. The lower part shows a vertical section of the arrangement. Both the Teflon cage encapsulating the glass capillary and the acquiring end of the optical fibre are mounted on micrometric stages that allow three-dimensional adjustments. These parts are adjusted by means of a He-Ne laser to be on the same optical axis (the  $y$ -axis, not shown in the Figure). The distances between the plasma jet and the lens and between the lens and the optical fibre determine an object to image ratio of 1:2. Since the aperture of the optical fibre was about 0.5 mm, only the light from a thin column along the optical axis of the investigated plasma jet was detected.

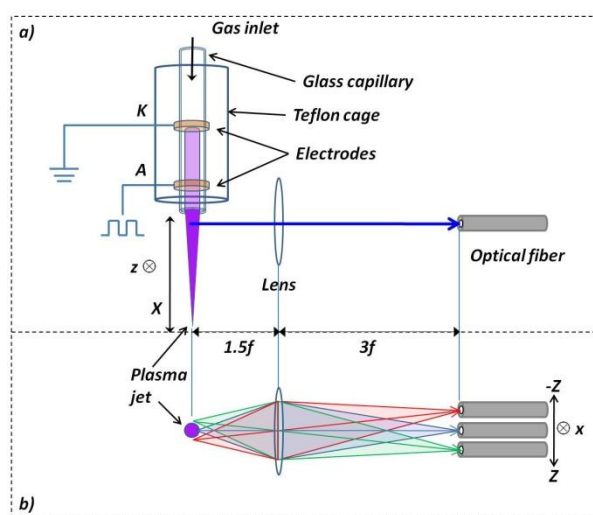


Figure 5.1 Optical arrangement for plasma jet mapping: a) top view, b) section view (end-on)

The effective jet mapping was performed by translating the capillary along the  $x$ -axis in 1 mm steps. For each  $x$  position the optical fibre was shifted along the vertical axis ( $z$ ) in 0.1 mm steps symmetrically with respect to the  $x$ -axis. Thus, the different parts of the jet were imaged on the optical fibre with spatial discrimination in  $z$ -direction of 0.5 mm

(diameter of the optical fibre). At each  $(x, z)$  position, spectra were acquired with 500 ms integration time. The spectra were taken at five and nine  $x$ -positions, for lower and higher gas flow rates, respectively. The spectra were stored by a laboratory PC for further analysis.

## 5.2 Measurements and results

Some results of the plasma jet mapping obtained at lower flow rate of He ( $F_A = 300 \text{ mL min}^{-1}$ ) are illustrated in Figure 5.2. The intensities of two spectral lines belonging to He,  $\text{N}_2^+$ , and  $\text{N}_2$  excited species are shown starting at the  $x_1$  position, which is at a distance of 1 mm away from the orifice of the capillary. The peak intensities of the spectral lines measured at particular  $(x, z)$  positions are represented by contours of constant intensity. Areas between the contours are filled with shades of gray in the range between white (intensity maxima) and black. There is a clear difference between the spatial intensity distributions of each type of the emitting species. The He lines exhibit an intensity maximum close to the capillary orifice, where the intensities of the  $\text{N}_2^+$ , and  $\text{N}_2$  lines are very weak. At a distance of about 2 mm from the capillary orifice both the  $\text{N}_2^+$  and the  $\text{N}_2$  line groups reach their maxima. With further increase of distance  $x$ , intensities of the  $\text{N}_2^+$  lines decrease faster than the intensities of the  $\text{N}_2$  lines.

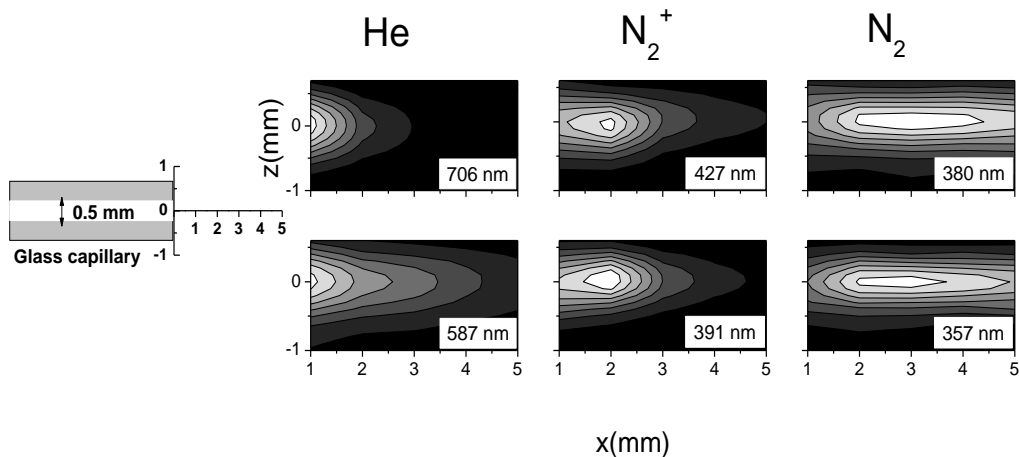


Figure 5.2 Spatial intensity distributions of two He,  $\text{N}_2^+$ , and  $\text{N}_2$  lines represented in two-dimensional contour plot. White areas indicate the regions of maximum intensity in the  $z$ - $x$  plane. The measurements were performed at flow rate of  $F_A=300 \text{ mL min}^{-1}$  through the capillary.

When the flow rate He through the capillary barrier discharge is increased to  $1000 \text{ mL min}^{-1}$  ( $F_B$ ), the general picture remains the same as given in Figure 5.2. However, the maxima regions of the  $\text{N}_2^+$ , and the  $\text{N}_2$  line intensity are shifted further away from the end of the capillary. In addition, the intensity distributions are broader than in the case of the lower He flow-rate. This effect is illustrated in Figure 5.3.

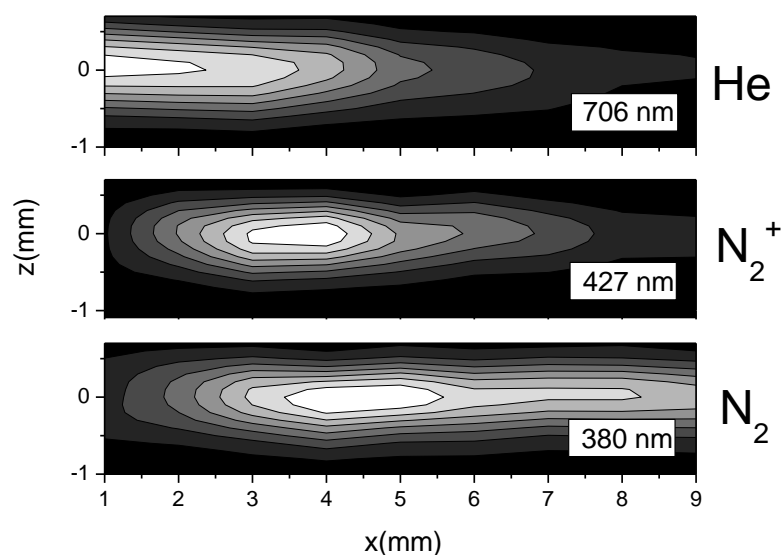


Figure 5.3 Two-dimensional contour plot of intensity distributions in  $z$ - $x$  plane for He 706 nm line (upper part),  $\text{N}_2^+$  427 nm line (middle part) and  $\text{N}_2$  380 nm (lower part). White areas indicate the regions of intensity maxima. The measurements were performed at a He flow rate of  $F_B = 1000 \text{ mL min}^{-1}$ .

A quantitative description of the investigated spatial line intensity distributions is given in Figure 5.4, where a part of the data set from Figure 5.3 is extracted. The plasma jet is nearly radially symmetric with respect to the  $x$ -axis. Due to the fact that the glass capillary could not be arranged perfectly horizontally, the plasma jet had a small inclination, which could be the reason for a slight asymmetry. However, as one can see in Figure 5.4 (left), the radial intensity distributions of the He,  $\text{N}_2^+$ , and  $\text{N}_2$  lines, i.e. the intensities measured along the  $z$ -axis cannot be distinguished within the error bars. These distributions are governed by diffusion of excited He atoms into surrounding atmosphere in radial direction. However, as already shown in Figure 5.2 and Figure 5.3, the distributions of the species mentioned above are strongly separated in  $x$ -direction, which is governed by the He flow rate. The data in Figure 5.4 (right) are presented in a semi-logarithmic plot, where the linear fits for the largest distances indicate that all

three distributions exhibit an exponential decrease. In contrast to the He and  $N_2^+$  lines, the  $N_2$  line intensities decrease much slower.

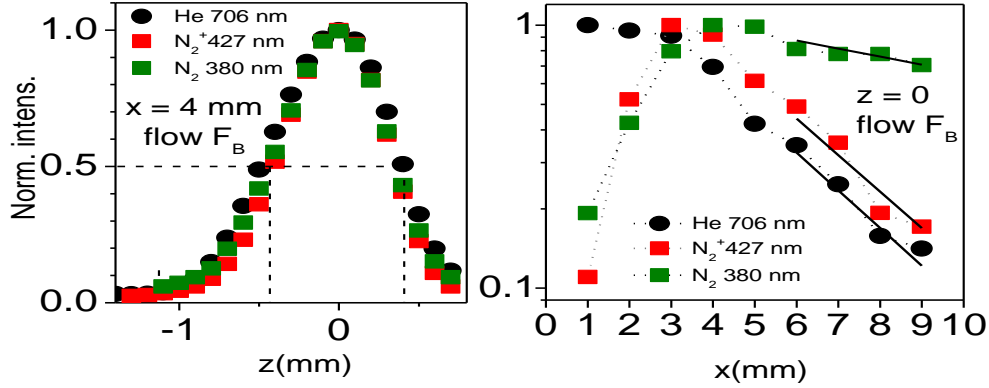


Figure 5.4 Intensity distributions of the He 706 nm, the  $N_2^+$  427 nm and the  $N_2$  380 nm lines extracted from the data presented in Figure 5.3 Left: distributions of the normalized radial line intensity represented by measurements along the  $z$ -axis at the position  $x = 4$  mm. Full width at half-maximum of radial intensity distributions amounts to about 0.9 mm. Right: Normalized intensity distributions along the  $x$ -axis ( $z = 0$ ) presented in semi-logarithmic plot. The size of the symbols used approximately represents the experimental error bars. Full straight lines are linear fits through data at the four largest values of  $x$ .

The intensity of an optically thin spectral line is proportional to the product of the number density in the relevant upper state and the corresponding radiative transition probability. Thus, spatial intensity distributions of the emitted optically thin lines belonging to different excited species yield information about position-dependent relationships between number densities in relevant upper states. In the following section, a simplified semi-quantitative model will be applied to describe the obtained line intensity distributions.

## 5.3 Description of line intensity distributions

### 5.3.1 Spatial density distributions in the jet

In the present case, we have a free burning helium plasma jet which penetrates from the capillary into the air. Initially, at  $x = 0$ , the He number density  $n_{He}$  has a maximum value  $n_{He}(0)$  which is defined by the atmospheric pressure and the temperature of the plasma gas. Similarly to that, the electron density distribution along the plasma jet is

expected to decrease monotonously, too. On the other hand, the density of the air should increase monotonously, starting from the capillary orifice. It is reasonable to assume that the  $x$ -dependence of the helium number density can be described by an exponential function:

$$n_{\text{He}}(x) = n_{\text{He}}(0) f_{\text{He}}(x) = n_{\text{He}}(0) \exp(-ax) \quad \text{for } a > 0. \quad (5.1)$$

Then, since the pressure is constant, the number density distribution of the air along the  $x$ -axis is determined by:

$$n_{\text{air}}(x) = n_{\text{air}}(\infty) f_{\text{air}}(x) = n_{\text{air}}(\infty) [1 - \exp(-ax)], \quad (5.2)$$

where  $n_{\text{air}}(\infty)$  is given by the atmospheric pressure and room temperature. It is plausible that the components of the air ( $\text{N}_2$ ,  $\text{O}_2$ ,  $\text{H}_2\text{O}$ ) obey the same normalized distribution:

$$f_{\text{comp}}(x) = f_{\text{air}}(x) = [1 - \exp(-ax)] \quad (\text{comp: } \text{N}_2, \text{O}_2, \text{H}_2\text{O}). \quad (5.3)$$

Regarding the high-frequency pulses of the plasma generator, the plasma jet is in a quasi-stationary regime. Therefore, the spatial distribution  $f_{el}(x)$  of the electrons produced in the discharge as well as the spatial distributions of excited particles can be regarded as independent of time. Furthermore, it is justified (see section 5.4 and the distribution of helium lines in semi-logarithmic plot) to assume that, in the present case,  $f_{el}(x)$  exhibits also an exponential decrease with increasing distance from the capillary orifice and here we postulate that:

$$f_{el}(x) = \exp(-bx) \quad b > 0. \quad (5.4)$$

It should be emphasized that, primarily due to temperature difference between plasma and air, the coefficients  $a$  and  $b$  are functions of position  $x$ , too. However, as already mentioned in the introduction, the DBD plasma jet is a cold source for soft ionisation, i.e. its gas temperature is slightly higher than the room temperature. Thus, one can approximately take both coefficients  $a$  and  $b$  to be constant.

### 5.3.2 Excitation energy transfer processes involving He, $\text{N}_2$ , and $\text{H}_2\text{O}$

Following the predictions made by experimental findings presented in the previous chapter and reported in [96], one can sketch the most important excitation and de-



excitation processes in the present investigation by using a strongly simplified term scheme presented in Figure 5.5. Here, the relevant states of the involved particles (He,  $N_2^+$ ,  $N_2$ ,  $(H_2O)^+$ ,  $H_2O$ ) are represented as a single state.

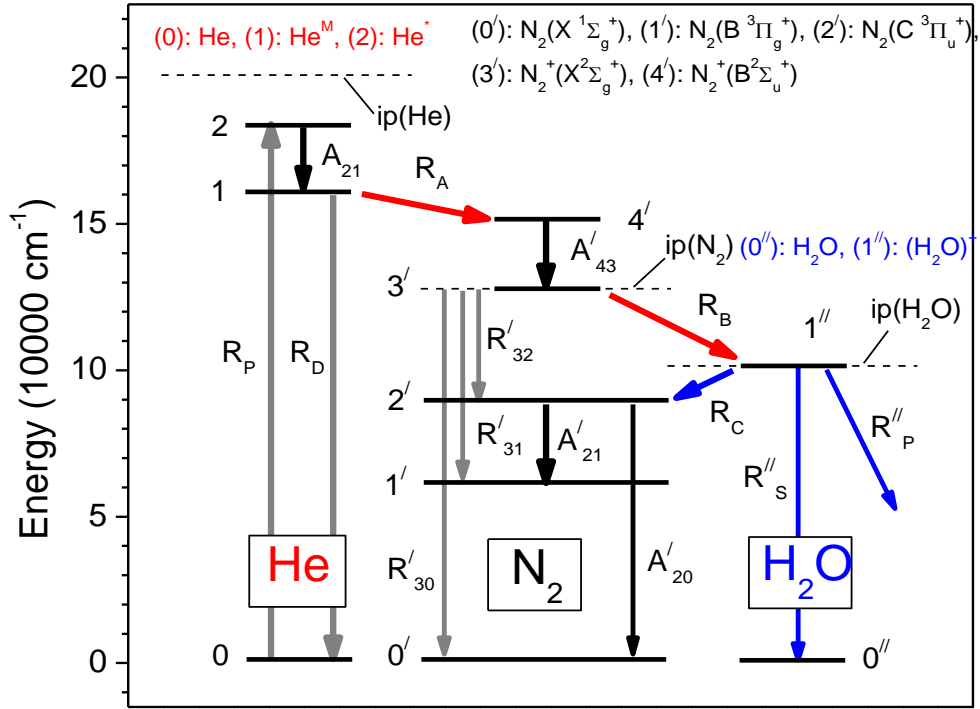


Figure 5.5 Simplified term scheme of He,  $N_2$  and  $H_2O$  with relevant radiative (full black arrows, rates labelled with  $A'_i$ ) and collisional transitions (gray arrows, rates labelled with  $R'_i$ ) in the cascade de-excitation from excited helium. Dashed lines designated with  $ip(He)$ ,  $ip(N_2)$ , and  $ip(H_2O)$  indicate the ionisation potentials. For the sake of picture clarity, the level designations are substituted by numbers. See further explanations in the text.

In the first step, *He* atoms are excited due to collisions with fast electrons produced in the discharge (electron impact excitation process):

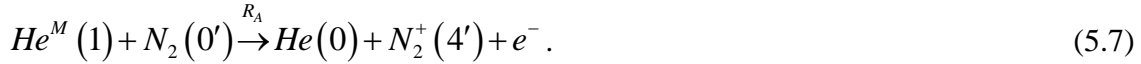


which occurs inside and partially outside of the capillary. The process (5.5) is characterized by a rate, i.e. collisional transition probability  $R_p$  (units:  $s^{-1}$ ). In general, the cross sections for electron impact excitation (EIE) are proportional to the relevant electric dipole moment of the particle in transition, i.e. to the corresponding dipole radiative transition probability, which is very small for metastable states. In particular, the cross sections for EIE of *He* metastables are about one order of magnitude smaller than the cross section for EIE of higher excited states [97]. For that reason, the strong

radiative relaxation of the higher excited states can be taken as the main path for population of metastables and the direct EIE of metastables can be neglected. In the next step, the metastable helium atoms are populated radiatively in the transition from the higher excited state:



Among other collisional de-excitations of He metastable atoms, Penning ionisation of  $N_2$  molecules is an important process in the present case. This has been presented in the previous chapter [96], where a comparison of DBD in He, Ne and Ar clearly shows the strong influence of He metastables on the production of  $N_2^+$  (i.e. the key role of Penning ionisation in formation of  $N_2^+$ ):



In addition, He metastables are de-excited due to collisions with slow electrons:



where  $R_D$  is the corresponding de-excitation rate. Radiative depopulation rates for helium metastables are very small, i.e. their radiative lifetimes are very long (order of magnitude: seconds). Nevertheless, it is well known that their effective lifetimes in plasma are significantly shorter due to collisions with electrons [98]. The collisional excitation processes always are followed by reverse de-excitations. The EIE of metastables, neglected above, are followed by electron impact de-excitations (EID). In contrast to EIE transition probabilities (which are small in comparison with those for higher excited states and therefore negligible in the present model), the EID rates are much larger than radiative relaxation rates of metastables. This leads to the establishment of shorter effective lifetimes of metastables. Therefore, the process (5.8) has to be taken into account.

The higher excited state  $4'$  of the ionised nitrogen molecule, populated in reaction (5.7), is de-excited in the radiative process  $4' \rightarrow 3'$ :



The radiatively populated ground state  $3'$  of the ionised nitrogen molecule is depopulated in a series of recombination processes determined by rates  $R'_{3j}$ :



In addition, ionised nitrogen molecules in the state  $3'$  can be depopulated in collisions with  $H_2O$  molecules:



where the energy difference  $\Delta E'$  between ionisation energy of  $N_2$  and  $H_2O$  is transferred to the kinetic energy of collision products.

In the present experiment, the production of ionised water is detected by the appearance of strong  $N_2$  lines. Namely, there is a probability for the process:



in which the ionised water molecule transfers its potential energy to the relatively close lower lying excited state  $2'$  of the neutral nitrogen molecule. Then, in the final de-excitation step considered here, the second excited state  $2'$  of  $N_2$  is depopulated in  $2' \rightarrow i'$  radiative transitions:



Certainly, excited  $N_2$  molecules can be produced due to electron impact. However, under the present experimental conditions, this mechanism is negligible in comparison to the process described by Eq. (5.13). This is indicated by the fact that in the region close to the capillary orifice the  $N_2$  lines are very weak (see Figure 5.2 and Figure 5.3).

Regarding the depopulation of  $(H_2O)^+$ , besides the transfer (5.12) there are a number of collision processes involving electrons and air components. First, one should take into account radiative recombination with electrons:



where the rate  $R_S''$  represents a sum of all recombination rates. We summarise all other collision processes leading to the depopulation of ionised water by the general expression:



Here, the  $M_1$  symbolizes either electrons or a particular air component, while  $M_2$  and  $M_3$  label the corresponding collision products.  $M_1$  could be an organic molecule acting as a reaction partner and the protonation can be initiated.

In the presented cascade one should consider the direct excitation by energy transfer  $N_2^+(3') \rightarrow N_2(2')$  done through collisions with  $H_2O$ , where water either remains ionised or releases its energy in the transition  $(H_2O)^+ \rightarrow H_2O$ . However, looking at the energy balance before and after such collisions (either strongly endothermic or strongly exothermic), it becomes clear that under the present physical conditions both processes can be neglected.

### 5.3.3 Rate equations

Following the predicted excitation and de-excitation paths described above, a set of corresponding rate equations can be defined.

As mentioned before, the plasma jet burns in a quasi-stationary regime. Therefore, the steady-state rate equations for relevant number densities appearing in the above reactions can be applied. The collisional transition probabilities, i.e. the collisional rates  $R$  introduced above, are usually defined as the products of corresponding rate coefficients  $k$  (unit:  $s^{-1} cm^3$ ) and the collision partner number density  $n$  ( $cm^{-3}$ ). In general, each of the described collisional excitation energy processes between a particular initial state  $i$  and a final state  $f$  (characterized by rate coefficient  $k_{if}$ ) is followed by the reverse reaction (rate coefficient:  $k_{fi}$ ). The principle of the detailed balancing predicts that  $(k_{if}/k_{fi}) \propto \exp(-\Delta E_{fi}/kT)$ , where  $\Delta E_{fi}$  is the energy difference between the final and the initial state. Under the present experimental conditions and with proper estimates for the excited state number densities, the processes reverse to the collisional excitation energy transfers listed above can be neglected. This approximation

leads to a simple set of six linear steady-state rate equations related to the six most important number densities  $n_0$ ,  $n_1$  and  $n_2$  of He, He<sup>M</sup>, He\*, respectively, as well as to the relevant number densities of nitrogen ( $n'_2, n'_3, n'_4$ ) and water ( $n''_1$ ) that are involved in the de-excitation path  $He^* \rightarrow He^M \rightarrow N_2^+ \rightarrow N_2$  or  $H_2O$ :

$$dn_2 / dt = 0 = R_p n_0 - A_{21} n_2 \quad (5.16)$$

$$dn_1 / dt = 0 = A_{21} n_2 - (R_A + R_D) n_1 \quad (5.17)$$

$$dn'_4 / dt = 0 = R_A n_1 - A'_{43} n'_4 \quad (5.18)$$

$$dn'_3 / dt = 0 = A'_{43} n'_4 - (R_B + \sum_{j=0}^2 R'_{3j}) n'_3 \quad (5.19)$$

$$dn''_1 / dt = 0 = R_B n'_3 - (R_C + R_S'' + R_P'') n''_1 \quad (5.20)$$

$$dn'_2 / dt = 0 = R_C n''_1 + R'_{32} n'_3 - (A'_{21} + A'_{20}) n'_2. \quad (5.21)$$

This set of equations involves all mentioned number densities and the rate equation representative for this calculation. All other ground states or excited species are not relevant for this path. The collisional pump rate  $R_p$  for the electron impact excitation process (5.5) is defined as the product of the corresponding rate coefficient  $k_p$  and the number density  $n_{el}$  (cm<sup>-3</sup>) of electrons. In the present weakly ionised plasma, the ground state number density of He ( $n_0$ ) equals with the total helium atom number density  $n_{He}$ . Thus, the positive contribution in Eq. (5.16) can be written as:  $R_p n_0 = k_p n_{el} n_{He}$ . The electron-induced de-excitation rate for the metastable state is defined as:  $P_D = k_D n_{el}$ , while the rate is  $R_A = k_A n_0' = k_A n_{N_2}$ . Here, for the same reason as in case of He, the ground state number density  $n_0'$  is replaced by the total density  $n_{N_2}$ . Furthermore, we have  $R_B = k_B n_0'' = k_B n_{H_2O}$ ,  $R_{3j}' = k_{3j}' n_{el}$  and  $R_S'' = k_S'' n_{el}$ . The sum in Eq. (5.19) represents the rate of possible depopulation processes given by Eq. (5.10), as well as the rate  $R_P''$  in Eq. (5.20) symbolizes the sum of all rates related to additional depopulation processes (5.15). Depending on the kind of collision partners  $M_l$  (either electrons or air components) these rates can be either in the form  $R_P''(e^-) = k_P^{el} n_{el}$  or  $R_P'(comp) = k_P^{comp} n_{comp}$ .

The investigated plasma jet is strongly inhomogeneous. It is obvious that the solutions to the set of rate equations (5.16 - 5.21) exhibit complex dependences on the position in the jet. Nevertheless, well-defined and very different  $x$ -dependencies of He and air components become a helpful tool in further analysis. Of course, one could question what is happening on the radial direction of the plasma jet, especially if there are any diffusion terms that have to be taken into consideration. This question can be answered taking into account the He gas velocity in the plasma jet of  $10^4 \text{ cm s}^{-1}$  and the narrow shape of this jet. They indicate that the diffusion velocity in radial direction is much lower than the axial velocity. The normalized distribution of intensities, as presented in Figure 5.4 (left part) for different species, is of the same bell shape which implies that the diffusion effects are negligible. Furthermore, the widths of these distributions are approximately independent of the  $x$ -position as it can be observed experimentally. Even if this diffusion effect would not be negligible, and the diffusion rates  $R_{diff}$  would be formally added to the radiative rates, the one-dimensional analysis considered in the following would not be affected in any way.

### 5.3.4 Discussion of the shapes of line intensity distributions

We consider the He,  $\text{N}_2^+$ , and  $\text{N}_2$  lines emitted at the frequencies  $\nu_{21}$ ,  $\nu'_{43}$  and  $\nu'_{21}$ . In the case of optically thin lines, their intensities are  $I_{He}(\nu_{21}) \propto A_{21}n_2$ ,  $I_{\text{N}_2^+}(\nu'_{43}) \propto A'_{43}n'_4$  and  $I_{\text{N}_2}(\nu'_{21}) \propto A'_{21}n'_2$ , respectively. Taking into account the present physical situation with the plasma jet penetrating in the atmosphere, it is plausible that the intensities of He lines should decrease monotonously with increasing the distance from the capillary orifice, while the intensities of the lines belonging to the air components will be initially zero and, after reaching a maximum, would decrease monotonously, too. It is also plausible that, in particular, the  $\text{N}_2^+$ , and  $\text{N}_2$  lines should exhibit the same distributions if only the direct electron excitation and radiative de-excitation processes (independent of the position) would occur. However, as shown below, the position-dependent excitation energy processes in the investigated system lead to different spatial distributions of the excited  $\text{N}_2^+$  and  $\text{N}_2$ .

**Distribution of the He lines:**

Rate equation (5.16) with the substitution  $R_p = k_p n_{el}$  yields the following simple spatial dependence of He line intensities along the  $x$ -axis:

$$I_{He}(v_{21}, x) \propto n_{el}(x)n_{He}(x). \quad (5.22)$$

Then, with exponential decrease of electron and helium density adopted above, the expected position-dependent intensities of optically thin He lines are of the following simple form:

$$I_{He}(v_{21}, x) \propto \exp[-(a+b)x]. \quad (5.23)$$

**Distribution of the N<sub>2</sub><sup>+</sup> lines:**

The combination of Eqs. (5.17) and (5.18) and the expression (5.22) yields the following relation between the position-dependent intensities of N<sub>2</sub><sup>+</sup> and He lines:

$$I_{N_2^+}(v'_{43}, x) \propto \Psi(x)I_{He}(v_{21}, x), \quad (5.24)$$

where the function  $\Psi(x)$  is given by:

$$\Psi(x) = \frac{R_A(x)}{R_A(x) + R_D(x)}. \quad (5.25)$$

As one can see from Figure 5.2 and Figure 5.3, the spatial distributions of N<sub>2</sub><sup>+</sup> lines strongly differ from the distributions of He lines. This means that the function  $\Psi(x)$  strongly depends on  $x$ . Up to our knowledge, the values for collisional rate coefficients needed for calculation of distribution (5.24) cannot be found in the literature. In addition, the electron number density has not been measured in the framework of the present investigation and a detailed modelling of line intensity distributions cannot be performed here. However, following the predicted de-excitation paths starting with He metastables and N<sub>2</sub><sup>+</sup> ions, one can define the conditions which should be fulfilled for the branching ratios of relevant collisional transition probabilities. As for the function  $\Psi(x)$ , the value of the branching ratio  $R_A(x)/R_D(x) = k_{AN_2}(x)/k_{Dn_{el}}(x)$  is crucial for describing its  $x$ -dependence, i.e. for describing the formation of N<sub>2</sub><sup>+</sup> (Figure 5.5). Therefore, we consider two extreme cases regarding this parameter.

*Case 1:*  $R_A(x) \gg R_D(x)$ .

In this case, the function  $\Psi(x)$  is nearly 1, which means that, according to expression (5.24),  $I_{N_2^+}(\nu'_{43}, x)$  should acquire the exact shape of the distribution of He lines. This is in contradiction with the present experimental findings therefore, *Case 1* can be excluded.

*Case 2:  $R_A(x) \ll R_D(x)$ .*

In this case, the term  $k_A n_{N_2}(x)$  in the denominator of expression (5.25) can be neglected and  $\Psi(x) \approx R_A(x)/R_D(x)$ , which corresponds to the case when  $\Psi(x)$  becomes strongly dependent on the  $x$ -position. According to the expressions (5.22), (5.24) and (5.25), the shape of  $N_2^+$  line intensity distributions becomes:

$$I_{N_2^+}(\nu'_{43}, x) \propto n_{N_2}(x)n_{He}(x) \quad R_A(x) \ll R_D(x). \quad (5.26)$$

Thus, with the normalized spatial density distributions for He, as previously defined, (Eq. (5.1)) and nitrogen molecules (Eq. (5.3)), the approximate relation (5.26) becomes:

$$I_{N_2^+}(\nu'_{43}, x) \propto [1 - \exp(-ax)] \exp(-ax) \quad R_A(x) \ll R_D(x). \quad (5.27)$$

### Distribution of the $N_2$ lines:

By combining Eqs. (5.18-5.21) is obtained the following relationship between the intensities distribution of the  $N_2$  and  $N_2^+$  lines ( $I_{N_2}(\nu'_{21}, x)$  and  $I_{N_2^+}(\nu'_{43}, x)$ ):

$$I_{N_2}(\nu'_{21}, x) \propto \Phi(x) I_{N_2^+}(\nu'_{43}, x), \quad (5.28)$$

where the function  $\Phi(x)$  reads:

$$\Phi(x) \propto \frac{R_B(x)}{R_B(x) + \sum_{j=0}^2 R'_{3j}(x)} \times \left[ \frac{R'_{32}(x)}{R_B(x)} + \frac{R_C(x)}{R_C(x) + R''_S(x) + R''_P(x)} \right]. \quad (5.29)$$

As shown in Section 5.2, these distributions are also very different in the investigated plasma jet. In order to determine the conditions which yield the most pronounced  $x$ -dependence of  $\Phi(x)$ , we examine extreme cases in the same straightforward manner as above. These extreme cases are defined by the relationships between the rate  $R_B(x)$  and the sum of recombination rates  $S(x) = \sum_{j=0}^2 R'_{3j}(x)$  as well as between  $R_C$  and  $R''_S + R''_P$ .



For the sake of clarity, four possible extreme combinations and corresponding approximate forms of  $\Phi(x)$  are listed in Table 5.1. As it can be seen in this table, only in the case 6 the function  $\Phi(x)$  takes a form which strongly depends on position  $x$ . In all other cases  $\Phi(x)$  becomes constant, which would imply equal distributions of the lines of neutral and ionised  $N_2$ . Therefore, we continue our consideration for *Case 6*. Looking at the denominator of the approximate expression for  $\Phi(x)$  in *Case 6*, once again two extreme solutions are possible. First, if  $(k_s'' + k_p^{el})n_{el}(x) \ll k_p^{comp}n_{comp}(x)$ ,  $\Phi(x)$  would be independent of position and consequently, the spatial distribution of  $N_2$  lines would not differ from the  $N_2^+$  line distribution. Therefore, this case (called *6a*) can be excluded and we continue our consideration for the case *6b*, implying  $(k_s'' + k_p^{el})n_{el}(x) \gg k_p^{comp}n_{comp}(x)$ . In this case, with the assumption of the distributions  $n_{H_2O}(x) \propto [1 - \exp(-ax)]$  and  $n_{el}(x) = \exp(-bx)$ , the spatial distributions of neutral nitrogen molecule lines are in this case:

$$I_{N_2}(\nu'_{21}, x) \propto [1 - \exp(-ax)]^2 \exp[-(a-b)x] \quad (\text{Cases 2 and 6b}). \quad (5.30)$$

Referring to case 6b, an introduction of organic molecules should be performed at the position where the maximum of  $N_2^+$  is located in order to get an efficient protonation. First results are given in [78] and will be investigated in detail in further experiments.

Table 5.1 Approximate expressions for  $\Phi(x)$ .

<i>Case 3:</i> $R_B(x) \ll S(x)$ , $R_C \ll (R_s'' + R_p'')$	$\Phi(x) \propto R'_{32}(x) / S(x) = k'_{32} / \sum_{j=0}^2 k'_{3j}$
<i>Case 4:</i> $R_B(x) \ll S(x)$ , $R_C \gg (R_s'' + R_p'')$	$\Phi(x) \propto \left( k'_{32} / \sum_{j=0}^2 k'_{3j} \right) + 1$
<i>Case 5:</i> $R_B(x) \gg S(x)$ , $R_C \gg (R_s'' + R_p'')$	$\Phi(x) \propto 1$
<i>Case 6:</i> $R_B(x) \gg S(x)$ , $R_C \ll (R_s'' + R_p'')$	$\Phi(x) \propto \frac{k_C n_{N_2}(x)}{(k_s'' + k_p^{el})n_{el}(x) + k_p^{comp}n_{comp}(x)}$

## 5.4 Comparison of experimental data with model data

Representative optically thin lines for He,  $N_2^+$  and  $N_2$ , with the wavelengths of 706 nm, 427 nm and 380 nm, respectively are considered. They are plotted in Figure 5.6 and Figure 5.7. The intensities are given in arbitrary units along the  $x$ -axis for lower ( $F_A$ )

and higher ( $F_B$ ) helium flow through the capillary. The intensities presented in Figure 5.6 and Figure 5.7 are extracted from the data presented in Figure 5.2 and Figure 5.3, respectively, representing the values along the  $x$ -axis at  $z = 0$ .

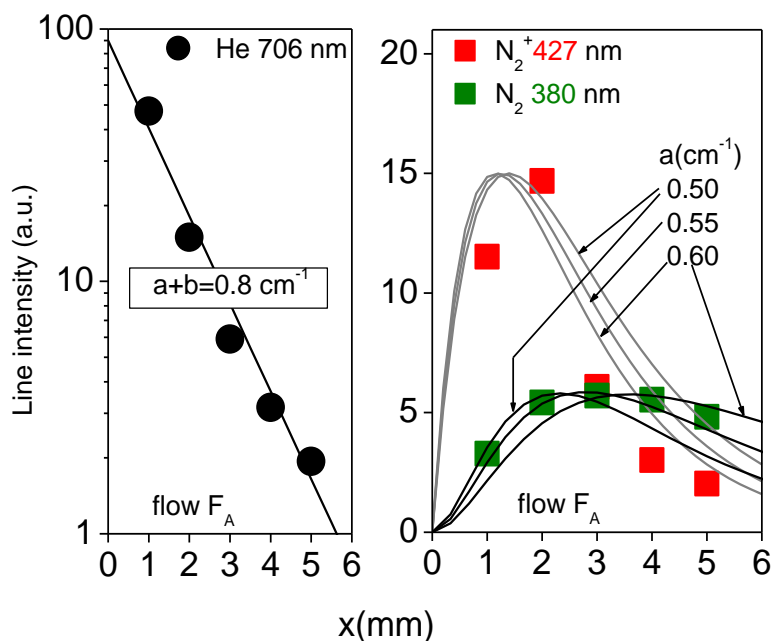


Figure 5.6 Comparison of experimental (symbols) and modelled (lines) intensity distributions for the He 706 nm (left),  $N_2^+$  427 nm and  $N_2$  380 nm lines (right) at lower helium flow  $F_A$ . The error of the experimental data is given of the size of the symbols.

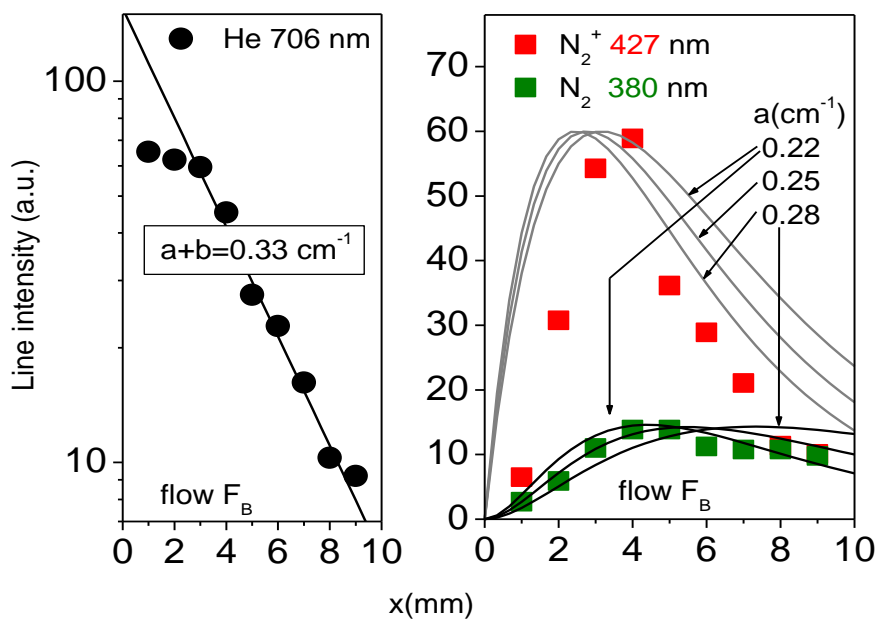


Figure 5.7 Comparison of experimental (symbols) and modelled (lines) intensity distributions for the He 706 nm (left),  $N_2^+$  427 nm and  $N_2$  380 nm lines (right) at higher He flow  $F_B$ . The error of the experimental data is given of the size of the symbols.

The experimental distributions are plotted together with fitted theoretical distributions. Following the previous considerations used up to now and the notation, the  $x$ -dependent intensity distributions for the He 706 nm,  $N_2^+$  427 nm, and  $N_2$  380 nm line intensities can be described by:

$$I(706) = C_{706} \exp[-(a+b)x] \quad (5.31)$$

$$I(427) = C_{427} [1 - \exp(-ax)] \exp(-ax) \quad (\text{Case 2}) \quad (5.32)$$

$$I(380) = C_{380} [1 - \exp(-ax)]^2 \exp[-(a-b)x] \quad (\text{Cases 2 and 6b}). \quad (5.33)$$

The values of scaling factors  $C_\lambda$  are expressed in arbitrary units. The data for the He 706 nm line are presented in semi-logarithmic plots together with the corresponding fitting functions. With the exception of the data obtained at the flow  $F_B$  for the  $x$ -values closest to the capillary orifice, there is a good agreement with the predicted exponential behaviour of the He lines, i.e. with the postulated exponential decrease of He as well as the electron number density along the  $x$ -axis described by the coefficients  $a$  and  $b$ , respectively. The deviation of the first two points from the exponential decrease can be explained by optical thickness of the He 706 nm line in this region at higher flow rate. By comparing analogous distributions of various He lines, it becomes evident that such deviations close to the capillary orifice indeed are correlated with their increased optical thickness. The fitted values  $(a+b)$  for the lower  $F_A$  and the higher flow  $F_B$  are  $0.8 \text{ cm}^{-1}$  and  $0.33 \text{ cm}^{-1}$ , respectively, with statistical errors less than 5 %. Here, in the case of  $F_B$ , the first two points were not included in the fitting procedure.

As shown in Section 5.2, the distributions for various  $N_2^+$  lines are very similar and within the error bars. Therefore, one can conclude that these lines are optically thin in the whole examined jet region and their intensity distributions can directly be connected with  $n_4'$ . An analogous conclusion is valid for the  $N_2$  lines and their connection with  $n_2'$ . In Figure 5.6 (right) and Figure 5.7 (right) the approximate expressions (5.32) and (5.33) are fitted to the intensity distributions of the lines of  $N_2^+$  427 nm (full gray lines) and  $N_2$  380 nm (full black lines).

Eqs. (5.32) and (5.33) are coupled with fitting parameters  $a$  and  $(a-b)$  which, combined with the values of the fitting parameter  $(a+b)$  for the given helium flow rate, yield

unambiguous values for the coefficients  $a$  and  $b$ . The values for the parameters  $a$  and  $(a+b)$  were determined by fitting the maximum positions of the distributions (5.32) and (5.33) to the positions of the intensity maxima of the 427 nm and 380 nm lines distributions, respectively. Taking into account the previously obtained values for  $(a+b)$ , the best fitting for both distributions can be obtained for  $a_A = (0.55 \pm 0.05) \text{ cm}^{-1}$  at lower and  $a_B = (0.25 \pm 0.03) \text{ cm}^{-1}$  at the higher helium flow rate. The corresponding values for the coefficients governing exponential decrease of electron densities are  $b_A = (0.80 - a_A)$  and  $b_B = (0.33 - a_B) \text{ cm}^{-1}$ . The factors  $C_\lambda$  were obtained by fitting to the values of experimental distributions maxima.

As one can see in Figure 5.6 and Figure 5.7, the experimental intensity distribution of the  $\text{N}_2^+$  427 nm line are narrower than the theoretical ones. As for the condition given by *Case 1* ( $R_A(x) \ll R_D(x)$ ), a more detailed numerical analysis shows that the calculated distribution (5.32) slightly changes even if the branching ratio  $R_A(x)/R_D(x)$  takes values up to 0.5. On the other hand, the  $\text{N}_2$ -line distributions are well described by the functional shape given by Eq. (5.33). It should be noted that, according to the conditions defined by the *Case 6b*, the major de-excitation of nitrogen ions is due to the energy transfer to the water molecules ( $R_B(x) \gg S(x)$ ) and only a small portion of  $(\text{H}_2\text{O})^+$  is depopulated due to collisions with  $\text{N}_2$  ( $R_C(x) \ll R'_S + R''_P$ ).

The general agreement between measurements and the simulation confirms two facts. First, both theoretical and experimental distributions are broader at higher helium flow rate, and second, both simulated curves at higher flow rate are shifted towards larger distances from the capillary orifice.

## 5.5 Conclusion

The spatially resolved spectroscopic measurements performed on the dielectric barrier plasma jet confirm the results of previous investigations while providing additional insight into the relevant excitation energy processes which lead to the pronounced ionisation of water in air and the subsequent protonation of organic molecules for soft ionisation.

The Intensity distributions in the plasma jet of some relevant emission lines of the species involved in the energy transfer process (He 706 nm, N<sub>2</sub> 380 nm and N<sub>2</sub><sup>+</sup> 427 nm) for two different helium flows (300 and 1000 mL min<sup>-1</sup>) have been discussed.

The plasma jet, which penetrates from the zone of the capillary barrier discharge into the atmosphere, has a strongly non-homogeneous distribution of the ground-state particles. However, the jet is axially symmetric and its non-homogeneity along the axis of penetration is well defined. This constitutes an important starting point in the presented modelling involving He and N<sub>2</sub> reactive states.

A simplified semi-quantitative analysis of the position-dependent energy transfer processes involving He, N<sub>2</sub> and H<sub>2</sub>O in their ground, excited and ionised states is presented. In this approach, the number density distributions of excited He, N<sub>2</sub><sup>+</sup> and N<sub>2</sub> along the plasma jet were simulated and compared with the intensity distributions of the corresponding optically thin spectral lines observed in the experiment.

There is a general agreement of the shapes of the simulated line intensity with the experiment, which is confirmed by the reproduced position of the maxima of line intensity as well as their shifting towards larger distances from the capillary orifice.

In turn, one can conclude that the main excitation path leading to the protonation of water in a helium plasma jet penetrating into the atmospheric air starts with the collision of He metastables and nitrogen molecules in air. Penning ionisation of nitrogen and subsequent energy transfer to the water molecules leads to an efficient ionisation and protonation of water. Approximate values were determined for several important branching ratios in the described cascade de-excitation model. In addition, the region in the plasma jet featuring the most efficient subsequent protonation of sample molecules was identified and will be the subject of further investigations.

By combining the present experimental findings with time-resolved measurements on a helium DBD plasma jet reported by Xiong et al [99], it can be argued that the main excitation path leading to protonation of water in helium plasma jet penetrating in the air atmosphere starts with the collisions of helium metastables and nitrogen molecules in air. From this, it can be concluded that Penning ionisation of nitrogen molecules and subsequent energy transfer to the water molecules are the processes leading to an efficient water ionisation and protonation.

As pointed out by Xiong et al [99], another reaction that can lead to production of  $N_2^+(B^2\Sigma_u^+)$  is represented by the charge transfer reaction as follows:  $He_2^+ + N_2 \rightarrow 2He + N_2^+(B^2\Sigma_u^+)$ . However, In the opinion of the authors, in DBD plasmas which are generated in mixtures of helium and nitrogen, this reaction may not be important in the decay phase, during which the positive ions mostly are represented by  $N_2^+$  or  $N_4^+$  but not by  $He_2^+$ .

The simplified distribution model along the plasma jet of the helium and nitrogen species based on the energy transfer processes is in good accordance with the performed spatially resolved mapping of the plasma jet. Distinct regions occupied by the atomic and molecular species of interest can be identified along the jet. It has been shown that there is a direct connection between population density of the He metastable and the  $N_2^+$  first negative system, so in the following chapter an estimation of one of the He excited levels involved in the production of metastables will be given.

## **6 ESTIMATION OF THE NUMBER DENSITY OF HE METASTABLE ATOMS IN THE PLASMA JET**

### **6.1 Optical absorption measurements for evaluating the He metastable density in the plasma jet**

As the results obtained so far show that there is a close relation between the He metastable excited state and the  $N_2^+$  first negative system, an important challenge rises: to determine the density of the He metastable atoms present in the plasma jet. One way to solve this problem would be the absorption spectroscopy technique. This technique measures the absorption of an incident beam of light passing a plasma layer. The wavelength of this beam of light has to be identical with the wavelength emitted by the plasma excited atoms through radiative decay between two well defined energetic levels. This technique was implemented by Kunze et al. [64] for a DBD applied to element spectroscopy using a diode laser. As for the specific He wavelengths observable in the plasma jet no diode laser or tuneable laser was available, the only possibility to perform absorption spectroscopy measurements was self absorption.

An attempt to perform optical self absorption measurements was done using a reflected beam from the capillary region in between the electrodes, passing through the plasma jet. A schematic of the experimental arrangement is presented in Figure 6.1.

The measurements were performed as follows: the light coming from the capillary region was collimated using the lens L1 positioned on the left side at a distance corresponding to  $1f$  away of the capillary, where  $f$  represents the lens focal length. The collimated beam is reflected back by the prisms and passes through the plasma jet. The second lens L2 positioned on the right side at a distance of  $1.5f$  from the plasma jet was installed to focus the light on the entrance of the optical fibre which was situated at  $3f$  distance. The position of L2 determined an object to image ratio of 1:2, fact providing a good optical resolution. Since the aperture of the optical fibre was about 0.5 mm, only the light from a thin column along the optical axis of the investigated plasma jet was detected.

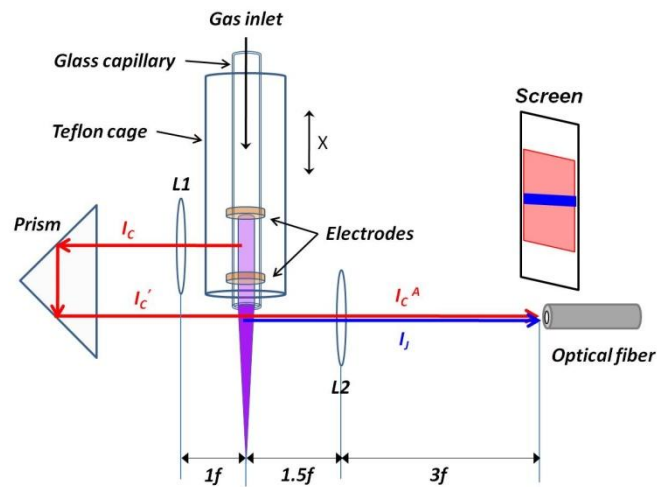


Figure 6.1 Experimental set-up for absorption measurements.  $I_C$  intensity of the light coming from the capillary region before passing through the plasma jet;  $I_J$  intensity of the light coming from the plasma jet region;  $I_C^A$  the intensity of the light coming from the capillary after passing through the plasma jet region.

Considering that the plasma jet is produced using a pulsed signal, in order to perform the self absorption measurements, the light emitted in the capillary ( $I_C$ ) and the light of the plasma jet ( $I_J$ ) have to be time synchronised. To ensure if the two plasma regions emit synchronised light, measurements using a photomultiplier (Hamamatsu R268) and an oscilloscope were carried out.

The following procedure was performed: first the emission signal from the plasma between the electrodes ( $I_C$ ) was measured on one channel of the oscilloscope while on the second channel the applied discharge voltage (“voltage signal in”) was used as reference. On the second step, the emission signal from the plasma jet ( $I_J$ ) was measured on the first channel while on the second channel the same signal (“voltage signal out”) was used as the reference. The data were stored and analysed afterwards. For one period, the applied discharge voltages and the corresponding plasma emission signals are plotted in Figure 6.2. Obviously, the signals of the two plasma regions are synchronised.

Based on these results, the absorption measurements were performed as follows: the Teflon cage encapsulating the glass capillary together with the copper electrodes was shifted in steps of 1 mm on the  $x$ -axis as it can be seen in Figure 6.1. The light from a certain point in between the electrodes ( $I_C$ ) was focused by the lens having a



correspondent point on the plasma jet ( $I_J$ ). The distance between  $I_C$  and  $I_C'$  reflected by the prism being always the same, (~1 cm), the first x position was approximately 1 mm apart from the end of the capillary and the last one was at 5 mm. For each x position three different spectra were acquired as follows: first the light coming from the plasma jet as well as from in between the electrodes ( $I_J$  and  $I_C^A$ ) was recorded, second, only the light coming from the plasma jet ( $I_J$ ) by blocking the collimated beam ( $I_C$ ), and third only the light coming from the plasma inside the capillary ( $I_C$ ) by blocking the light from the jet. This procedure was performed for two different flows of gas  $300 \text{ mL min}^{-1}$  and  $1000 \text{ mL min}^{-1}$ , respectively. The spectra were stored by a laboratory PC for further evaluations.

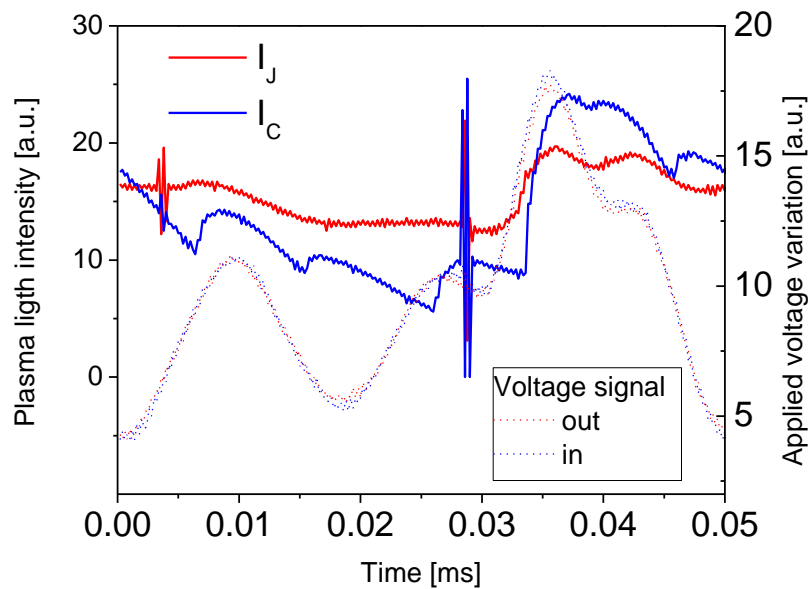


Figure 6.2 The applied voltage signal (dashed lines) and the corresponding plasma emission signal (continuous lines) from the region between the electrodes  $I_C$  (blue line) and from the plasma jet  $I_J$  (red line)

Although the effects of absorption of the reflected beam were registered, these results cannot be used for evaluation of He metastable atom density. This conclusion was based on the findings presented by Kunze et al [100] and Xiong et al. [99] on absorption measurements on a DBD discharge and a dielectric plasma jet, respectively. According to the results given by the authors above mentioned, one can conclude that in the plasma jet, which is subject of this research, the plasma burns in a relatively short time interval (about  $10 \mu\text{s}$ ). Only in this period, fast electrons are present and the gas temperature is significantly higher than room temperature. In a relatively long time interval between

two pulses (about 100  $\mu\text{s}$ ) the jet is cold (nearly at room temperature) and the population of metastables is high. In this period, the cascade de-excitation of metastables by collisions with air components begins, starting with the Penning ionisation  $\text{He}^M + \text{N}_2 \rightarrow \text{He} + \text{N}_2^+ + e^-_{\text{slow}}$ . Taking into account the conclusion given above, one should first of all have in mind the fact that the line emission emerges from the plasma “bullets” described in the previous chapter, which travel through the gas flow. Second, the Ocean Optic spectrometer used integrates the emission line within a spatial window defined by the spatial resolution ( $\Delta z$ ,  $\Delta x$ ). However, the reflected light, most probably, hits cold gas somewhere between two pulses. A simulation of the “time-frozen” jet is shown in Figure 6.3.

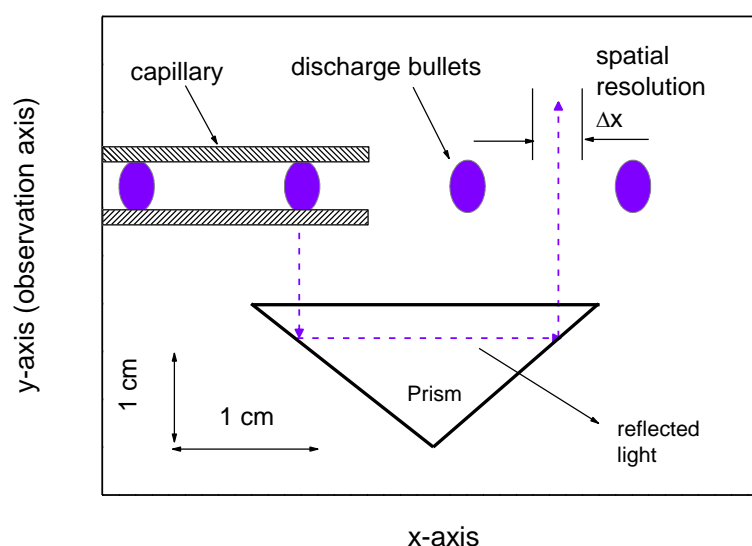


Figure 6.3 “Frozen” jet simulated for the He flow of 1000 mL min<sup>-1</sup>.

For the gas flow of 1000 mL min<sup>-1</sup> the velocity is about 10<sup>4</sup> cm s<sup>-1</sup> and a fast camera would record narrow discharge bullets at certain positions along the  $x$ -axis. The duration of the discharges (10  $\mu\text{s}$ ) and the gas velocity yield the corresponding bullet length of about 1 mm. The distance between the bullets (about 1 cm) is determined by the time interval between two pulses (100  $\mu\text{s}$ ). The possibility of mismatching between the light emitted of one plasma bullet inside the capillary ( $I_C$ ) and a plasma bullet outside the capillary, based on the unknown parameters, forced to abandon this evaluation method of the density of He metastable atoms. For the same purpose, another technique was

implemented based on the emission measurements performed for the plasma jet mapping (see chapter 5). This evaluation will be presented in the following.

## 6.2 Observed spectral intensities

Based on the experiential arrangement used in the previous chapter for the plasma jet mapping, one can apply the expression for the spectral intensities as follows:

$$I^\nu = \rho^\nu c = \frac{8\pi^2}{c^2} \frac{h\nu}{\exp(h\nu/kT) - 1}, \quad (6.1)$$

where  $\rho^\nu = \frac{8\pi^2}{c^3} \frac{h\nu}{\exp(h\nu/kT) - 1}$  represents the spectral density of radiation emitted at

a frequency  $\nu$ (Hz) per unit volume and per unit frequency interval  $d\nu$ , it has the unit  $\text{erg cm}^{-3} \text{ Hz}$ . Here, the temperature is given in Kelvin and the values for  $c$ ,  $h$ , and  $k$  are  $3 \times 10^{10} \text{ cm s}^{-1}$ ,  $6.625 \times 10^{-27} \text{ erg s}$ , and  $1.38 \times 10^{-16} \text{ erg K}^{-1}$ , respectively (according to A.P. Thorne [101]). The emission spectra were observed along the  $y$ -axis and they were measured in the  $x$ - $z$  plane with a spatial resolution defined by  $\Delta z = \Delta x = 0.25 \text{ mm}$  as it can be seen in Figure 5.1 in the previous chapter. The lower part of this figure is repeated in Figure 6.4 for clearness of the explanations.

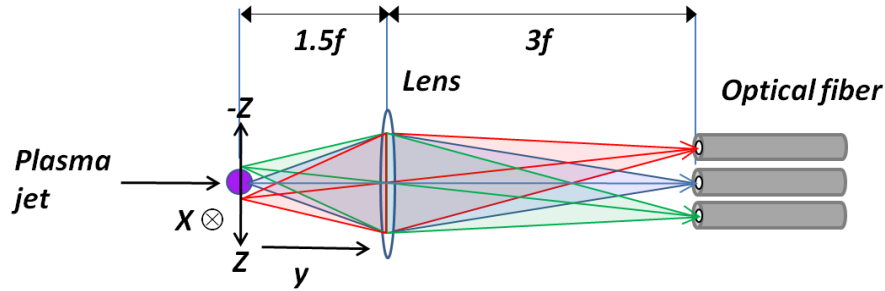


Figure 6.4 Optical arrangement for plasma jet mapping performed as described in chapter 5.

### 6.2.1 Number density distributions

In the case of the plasma jet studied here, the number density distributions for different species of interest are radially symmetric with respect to the  $x$ -axis (along the plasma jet):  $n(\vec{r}) = n(x, r)$ . They can be derived by the Abel inversion method (see Appendix)

from the intensities of optically thin lines measured along the  $z$ -axis as those shown in Figure 6.5.

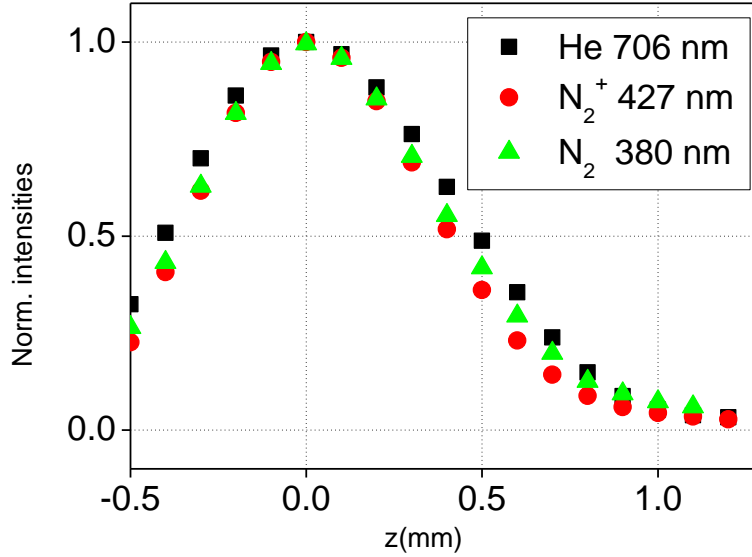


Figure 6.5 Normalized line intensity distributions of optically thin lines measured at flow  $F_B$  at position  $x = 4 \text{ mm}$ .

The density distributions  $n(x,y)$  obtained by Abel inversion from normalized intensities, plotted in Figure 6.5, are of a bell-shape form, too. Their full widths at half maximum are slightly higher (about 10 %) than those of measured intensity shapes. Consequently, in the present case the emission intensity  $I_0$  given by the expression:

$$I_0 = \varepsilon_{21}(\nu) / k_{12}(\nu) \sim \frac{8\pi hc}{\lambda_{12}^3} \frac{n_2}{n_1} \frac{g_1}{g_2} \quad (6.2)$$

at a given position in  $x$ - $z$  plane strongly depends on the variable  $y$ . In the following evaluation only the maximum intensities will be considered, i.e. the intensities measured along the  $x$ -axis at  $z = 0$  (Figure 6.4). In order to simplify the present problem, and consequently to obtain an analytical expression for the relevant position-dependent spectral intensity  $I_{21}^\nu(x, z = 0)$ , two approximations have to be done.

First approximation: the normalized density distributions in the upper and lower states corresponding to a certain radiative transition are equal. In practice, this is not always true, but in the present experiments it can be taken as valid.

Second approximation: the supposed bell-shape density distribution  $n(x,y)$  is replaced by a square function which is equal to  $n^0(x)$  within the interval  $y \in [-L_{eff}/2, +L_{eff}/2]$  and otherwise equal to 0, as it is shown in Figure 6.6.

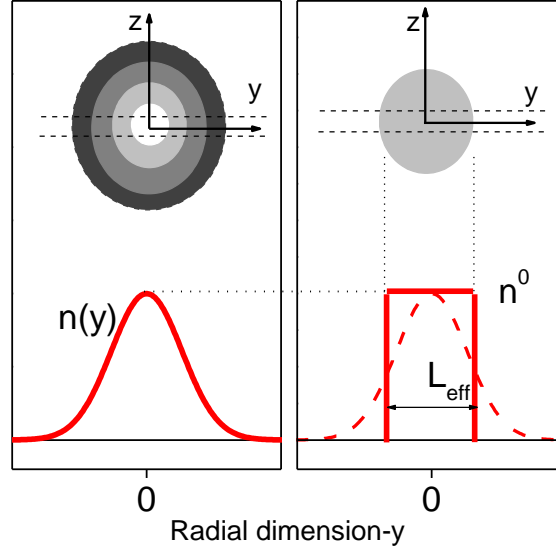


Figure 6.6 Square approximation for the number density distributions.

The second approximation means that the observed plasma column at  $z = 0$  is treated as homogeneous. The density is regarded to be equal to the maximum value  $n^0(x)$  at the axis of the jet. The effective length of the observed column is defined as  $L_{eff} = \int n(y)dy/n^0$ , so the integrals of the considered bell-shaped and square function are equal.

### 6.2.2 The spectral intensity of the measured He lines

According to the experimental findings, the widths of radial intensity distributions are nearly equal at different  $x$ -positions, i.e. the corresponding effective lengths are constant and their value is  $L_{eff} \approx 0.1 \text{ cm}$ . Using the approximations introduced above, the spectral intensity  $I_{21}^v$ , which is observed along the  $y$ -axis at a certain position  $x$  along the plasma jet and at  $z = 0$ , can be written according to expressions (A.3) and (A.12) in the appendix as follows:

$$I_{21}^{\nu}(x, \nu) \sim \frac{8\pi hc}{\lambda_{12}^3} \frac{n_2^0(x)}{n_1^0(x)} \frac{g_1}{g_2} \left\{ 1 - \exp \left[ -\frac{\lambda_{12}^2}{8\pi} \frac{g_2}{g_1} A_{21} n_1^0(x) L_{\text{eff}} P_{21}(\nu) \right] \right\} \quad (6.3)$$

For clearness of explanation, the radiative transitions corresponding to the emission line analysed in the present studies are depicted in Figure 6.7. Also the first He resonance line at 58.4 nm as well as the 388.8 nm and 1083.0 nm lines are indicated.

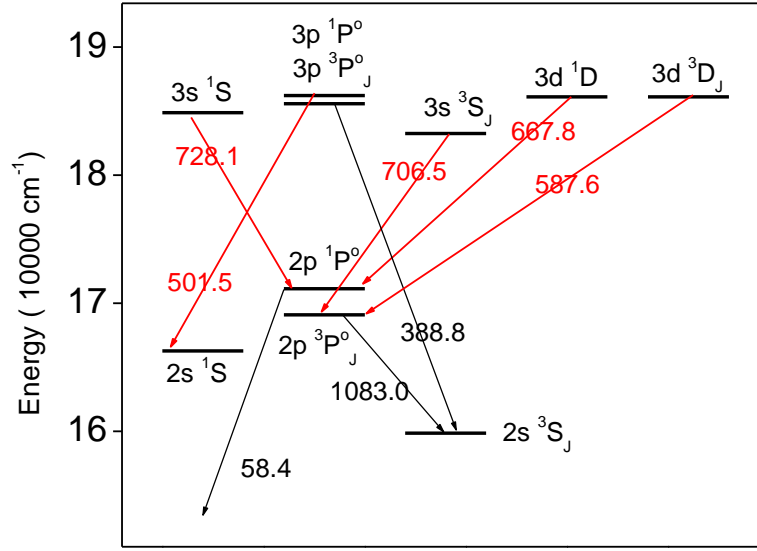


Figure 6.7 Partial term diagram of He and the relevant transitions. The transitions corresponding to the measured lines are symbolized by red arrows. The attributed numbers are the wavelengths in nanometers [102].

The basic data for the transitions plotted in Figure 6.7 are given in the following table.

Table 6.1 Basic data for the lines emerging in transitions between the lowest He states [102].

$\lambda(\text{nm})$	Transition	$E_i (\text{cm}^{-1})$	$E_k (\text{cm}^{-1})$	$g_i$	$g_k$	$A_{ki} (10^8 \text{ s}^{-1})$
58.4	$1s^2 \ ^1S \leftrightarrow 2p \ ^1P^{\circ}$	0	171135	1	3	18
388.8	$2s \ ^3S_j \leftrightarrow 3p \ ^3P^{\circ}_j$	159856	185565	3	5	0.095
501.5	$2s \ ^1S \leftrightarrow 3p \ ^1P^{\circ}$	166278	186210	1	3	0.13
587.6	$2p \ ^3P^{\circ}_j \leftrightarrow 3p \ ^3D_j$	169087	186102	5	7	0.71
667.8	$2p \ ^1P^{\circ} \leftrightarrow 3d \ ^1D$	171135	186105	3	5	0.638
706.5	$2p \ ^3P^{\circ}_j \leftrightarrow 3s \ ^3S$	169087	183237	5	3	0.278
728.1	$2p \ ^1P^{\circ} \leftrightarrow 3s \ ^1S$	171135	184865	3	1	0.18
1083.0	$2s \ ^3S \leftrightarrow 2p \ ^3P^{\circ}_j$	159856	169087	3	5	0.10

## 6.3 Broadening of the He lines

One important aspect of the spectroscopy in general and of optical spectroscopy in particular is the broadening of the measured line, i.e. the lines recorded in a spectrum exhibit a broadening (a physical width) centred on the actual emission line. In the analysis of the recorded spectra several parameters have to be taken into consideration in order to get the real profile of the line and also to determine the physical properties of the system emitting that wavelength. In the following section the broadening aspects will be taken into consideration in determining the profile of He 728 nm line. A detailed presentation of the broadening components can be found in the Appendix.

### 6.3.1 General aspects

In the present experiment the measured He lines are emitted from hot plasma "bullets" (or "pockets"), where in principle they are absorbed, too. The plasma is weakly ionised and the line kernels are broadened mainly due to collisions (impact broadening) with neutral perturbers (He and air components) and fast electrons. These mechanisms contribute to the Lorentz components of the line profiles. In addition, the observed lines are broadened by the Doppler effect. For the modelling of the resulting line profiles  $P(\nu)$  one should know the gas temperature, the number densities of the perturbing particles and the corresponding impact broadening parameters  $\gamma_P^\nu$ . The impact self-broadening parameters of the He lines, which are of interest, are taken from literature [103-106] and are listed in the following table:

Table 6.2 Self-broadening (Lorentz) parameters at  $T = 300\text{ K}$  of the considered He lines taken from the references [103-106].

Emission line (nm)	$\gamma_{He}^\nu (10^{-9} \text{ cm}^3 \text{ s}^{-1})$
He 501	1.47
He 587	1.30
He 667	2.45
He 706	1.4
He 728	2.35

The impact parameters given above are due to van der Waals interactions and, according to the theory of line broadening, their values are temperature dependent ( $\gamma \propto T^{0.3}$ ).

### 6.3.2 Lorentz and Doppler broadening of the He 728.1 nm line

In the following section, the broadening of the He 728.1 nm line in pure helium at atmospheric pressure is simulated for two values of gas temperature:  $T_\alpha = 1000\text{ K}$  and  $T_\beta = 2000\text{ K}$ . This yields the He number densities of  $n_{\text{He}}^\alpha = 7.2 \times 10^{18}\text{ cm}^{-3}$  and  $n_{\text{He}}^\beta = 3.6 \times 10^{18}\text{ cm}^{-3}$ , respectively, and the corresponding FWHM's of the components of the Lorentz profile are  $\Delta_L^\alpha = 24.3\text{ GHz}$  and  $\Delta_L^\beta = 15\text{ GHz}$  according to the formula (A.25) in the appendix. The corresponding Doppler (Gauss) widths are  $\Delta_D^\alpha = 4.6\text{ GHz}$  and  $\Delta_D^\beta = 6.5\text{ GHz}$ , according to the formula (A.23) in the appendix. The normalized ( $\int P(\nu)d\nu = 1$ ) Doppler and Lorentz profiles for the present examples are given in Figure 6.8. The profiles were calculated and plotted in Origin using the formulas in appendix. Here, the profiles are centred to the line frequency  $\nu_{21}$ , i.e. the conversion  $\nu \rightarrow \nu - \nu_{21}$  was made.

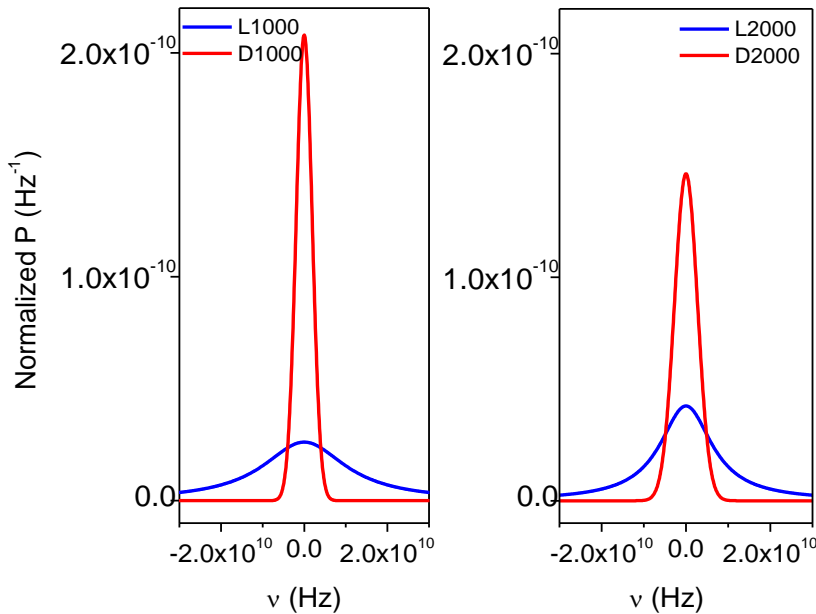


Figure 6.8

Calculated Lorentz and Doppler components for the present example: He 728.1 nm line at atmospheric pressure and two different temperatures: 1000 K and 2000 K. Lorentz components: L1000 and L2000, Doppler components: D1000 and D2000.



### 6.3.3 Voigt profiles and Pearson-7 function

In general, both Doppler and Lorentz broadening mechanisms are present and the resulting profile of a spectral line represents their convolution:

$$P_{12}^V(\nu) = \int P_{12}^D(\nu - x) P_{12}^L(x) dx \quad (6.4)$$

which is well known as the Voigt profile. There is no exact analytical solution to Eq. 6.4 representing the convolution of the Doppler and Lorentz profiles, and for each particular case numerical calculations are needed. Nevertheless, for given values of the FWHM of the Doppler and Lorentz profiles, in the literature one can find approximate analytical expressions for corresponding Voigt profiles.

However, there are empirical formulas as those given by Kunze et al [64] for the full width at half-maximum  $\Delta_\nu$  and the peak value  $P_{21}^V(\nu_{21}) \equiv P_0^V$  of the Voigt profile. In terms of Doppler and Lorentz FWHM's, these quantities can be written as:

$$\Delta_\nu = \Delta_L / 2 + \sqrt{(\Delta_L / 2)^2 + \Delta_D^2} \quad (6.5)$$

$$P_0^V = \frac{1}{\Delta_\nu [1.065 + 0.447(\Delta_L / \Delta_\nu) + 0.058(\Delta_L / \Delta_\nu)^2]} \quad (6.6)$$

The relations discussed above are accurate to 1% for all values of the ratio  $\Delta_L/\Delta_D$  in the range from 0 to  $\infty$ . The calculation of Voigt profiles is time consuming and it is very convenient to use appropriate analytical approximations. One of them is the function known in algebra as Pearson-7 function [107] defined as:

$$P_{12}^{(7)}(\nu) = \frac{P_0^V}{\left[1 + \frac{4(\nu - \nu_{21})^2}{(\Delta_\nu)^2}\right]^p} \quad (6.7)$$

By variation of the parameter  $p$ , the best fit for the calculated Voigt profile is obtained. For ratios  $\Delta_L/\Delta_G$  higher than 2, this parameter amounts 1. Otherwise,  $p$  is higher than 1, and for instance, for  $\Delta_L/\Delta_G = 0.1$ , the best match is obtained with  $p \approx 2.5$ . In Figure 6.9, the Pearson-7 function is plotted for the example described above at  $T = 2000$  K.

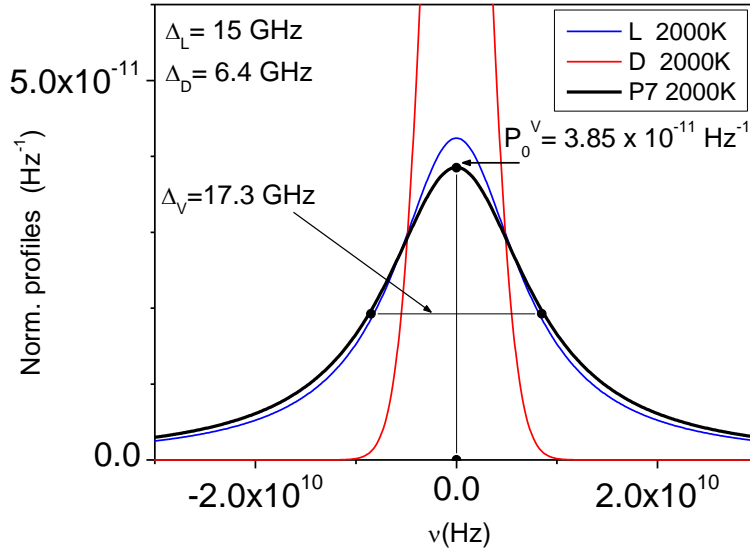


Figure 6.9 Pearson-7 profile (black line) calculated via Eqs. (6.5), (6.6) and (6.7) for the example described above at  $T = 2000$  K. L2000 (blue line): Lorentz component, D2000 (red line): Doppler component.

In the present example, the ratio  $\Delta_L/\Delta_G$  amounts to 2.34 and the value of the parameter  $p$  was taken to be 1. Parallel with that, the corresponding Voigt profile was calculated via Eq. (A.26) in the appendix. An excellent agreement between the profile represented by the Pearson-7 function and the numerically obtained convolution was found in the line kernel as well in the far line wings.

### 6.3.4 Measured line intensities

To measure the real shape of an observed spectral line intensity, one needs a spectrometer whose band pass is at least 10 times narrower than the FWHM of the line. For the example given for the He 728 nm line in section 6.3.2, the required band pass would be about  $\delta\nu = 2$  GHz ( $\delta\lambda = 3.5 \times 10^{-3}$  nm). As mentioned before, for the measurements that have been performed, the spectrometer band pass is much larger than the FWHM of the measured lines, so that the registered signals correspond to the integrals of spectral intensities discussed in case a in the appendix. Therefore, in the present case, the measured line intensities are given by Eq. (A.16) in the appendix:

$$I_{21}^M(\nu) \sim r(\nu_{21})P_S(\nu - \nu_{21}) \int_{-\infty}^{+\infty} I_{21}^V(\nu) d\nu. \quad (6.8)$$

Indeed, all measured intensities exhibit the same wavelength-dependent shape, i.e. a shape equal to the instrumental profile as it can be seen in the lower right graph of Figure 6.10. However, their peak intensities depend on the integral of the corresponding spectral intensities over the frequencies.

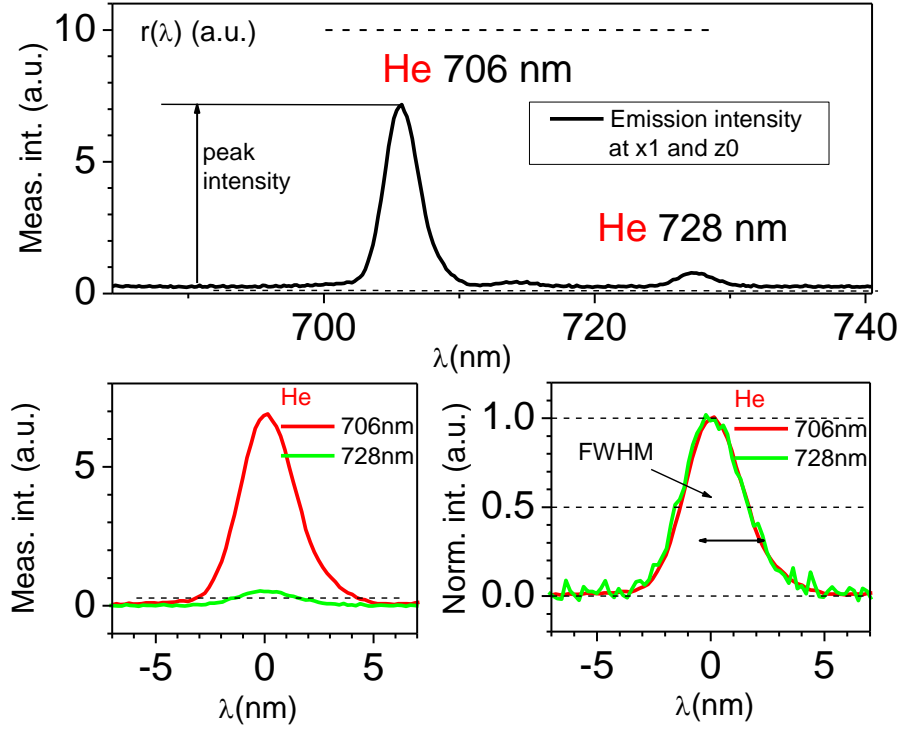


Figure 6.10 Upper plot: The sequence of the mapping measurement at a He flow rate of  $1000 \text{ mL min}^{-1}$ . The  $r(\lambda)$  is the spectral response (supposed to be constant in the considered relatively narrow wavelength range). Lower plot left: Centred line intensities with reduced background. Lower plot right: The line intensities normalized with respect to the peak intensity values.

In the present case, the expression for the measured peak intensities  $I_{21}$  can be written as:

$$I_{21} \sim r(\nu_{21}) \int_{-\infty}^{+\infty} I_{21}^{\nu}(\nu) d\nu. \quad (6.9)$$

Taking into account Eq. (6.3) from above, the intensities of the measured peak at certain  $x$  position along the plasma jet axis and  $z = 0$  are given by:

$$I_{21}(x) \sim r(\lambda_{21}) \frac{8\pi hc}{\lambda_{12}^3} \frac{n_2^0(x)}{n_1^0(x)} \frac{g_1}{g_2} \int \left\{ 1 - \exp \left[ -\frac{\lambda_{12}^2}{8\pi} \frac{g_2}{g_1} A_{21} n_1^0(x) L_{\text{eff}} P_{21}(\nu) \right] \right\} d\nu. \quad (6.10)$$

In the case of optically thin lines, the integral in previous equation becomes:

$$\int \{1 - \exp[-KP_{21}(\nu)]\} d\nu \approx \int \{1 - 1 + KP_{21}(\nu)\} d\nu = K \quad (6.11)$$

and the measured peak intensities at the position given above are of the simple form:

$$I_{21}(x)|_{thin} \sim \frac{hc}{\lambda_{12}} n_2^0(x) L_{eff} A_{21}. \quad (6.12)$$

### 6.3.5 Curve of growth

The integral in Eq. (6.10) discussed in the previous section is the so-called curve of growth. Generally, for a homogeneous layer the curve of growth  $F_{CG}$  is given by the following formula:

$$F_{CG} = \int \left\{ 1 - \exp \left[ -\frac{\lambda_{12}^2 g_2}{8\pi g_1} A_{21} n_1 L P_{21}(\nu) \right] \right\} d\nu. \quad (6.13)$$

The curve of growth describes the growth of the intensity of a spectral line with the increase of the product  $n_1 L$ . For optically thin lines, this growth is linear with  $n_1 L$ . The  $F_{CG}$  depends not only on the variable  $n_1 L$ , but also on basic line parameters and line profile, which is governed by actual physical conditions.

A practical example for calculation the curve of growth of He 728 nm line will be given in the appendix.

### 6.3.6 Simulated curves of growth for He 728 nm line

Using the procedure presented in the appendix, three curves of growth for He 728 nm line were calculated using the input parameters given in table 6.3.

Table 6.3 Input broadening parameters ( $p_{He} = 1 \text{ Atm}$ ).

	A	B	C
T(K)	1000	2000	1000
$\Delta D$ (GHz)	4.6	6.5	4.6
$\Delta L$ (GHz)	24.3	15	72.9

The chosen input parameters correspond to the range of the predicted physical conditions at the capillary orifice. The results obtained are tabulated below and plotted in Figure 6.11.

It has to be noted that in the optically thin region, the curves of growth do not depend on the line profiles and exhibit a linear dependency on the product  $n_1L$ .

Table 6.4 Calculated curves of growth for the He 728 nm using the parameters defined in Table 6.3.

$n_1L$ (cm <sup>-2</sup> )	$F_{cg}^A$ (Hz)	$F_{cg}^B$ (Hz)	$F_{cg}^C$ (Hz)
$1 \times 10^{11}$	$1.27 \times 10^8$	$1.26 \times 10^8$	$1.25 \times 10^8$
$2.1 \times 10^{11}$	$2.68 \times 10^8$	$2.65 \times 10^8$	$2.63 \times 10^8$
$4.6 \times 10^{11}$	$5.86 \times 10^8$	$5.79 \times 10^8$	$5.77 \times 10^8$
$1 \times 10^{12}$	$1.26 \times 10^9$	$1.25 \times 10^9$	$1.25 \times 10^9$
$2.1 \times 10^{12}$	$2.64 \times 10^9$	$2.59 \times 10^9$	$2.62 \times 10^9$
$4.6 \times 10^{12}$	$5.67 \times 10^9$	$5.50 \times 10^9$	$5.70 \times 10^9$
$1 \times 10^{13}$	$1.18 \times 10^{10}$	$1.12 \times 10^{10}$	$1.22 \times 10^{10}$
$2.1 \times 10^{13}$	$2.29 \times 10^{10}$	$2.10 \times 10^{10}$	$2.49 \times 10^{10}$
$4.6 \times 10^{13}$	$4.30 \times 10^{10}$	$3.72 \times 10^{10}$	$5.12 \times 10^{10}$
$1 \times 10^{14}$	$7.27 \times 10^{10}$	$5.91 \times 10^{10}$	$9.84 \times 10^{10}$
$2.1 \times 10^{14}$	$1.11 \times 10^{11}$	$8.70 \times 10^{10}$	$1.68 \times 10^{11}$
$4.6 \times 10^{14}$	$1.67 \times 10^{11}$	$1.27 \times 10^{11}$	$2.70 \times 10^{11}$
$1 \times 10^{15}$	$2.48 \times 10^{11}$	$1.85 \times 10^{11}$	$4.09 \times 10^{11}$
$2.1 \times 10^{15}$	$3.58 \times 10^{11}$	$2.62 \times 10^{11}$	$5.92 \times 10^{11}$
$4.6 \times 10^{15}$	$5.26 \times 10^{11}$	$3.78 \times 10^{11}$	$8.65 \times 10^{11}$
$1 \times 10^{16}$	$7.63 \times 10^{11}$	$5.41 \times 10^{11}$	$1.24 \times 10^{12}$

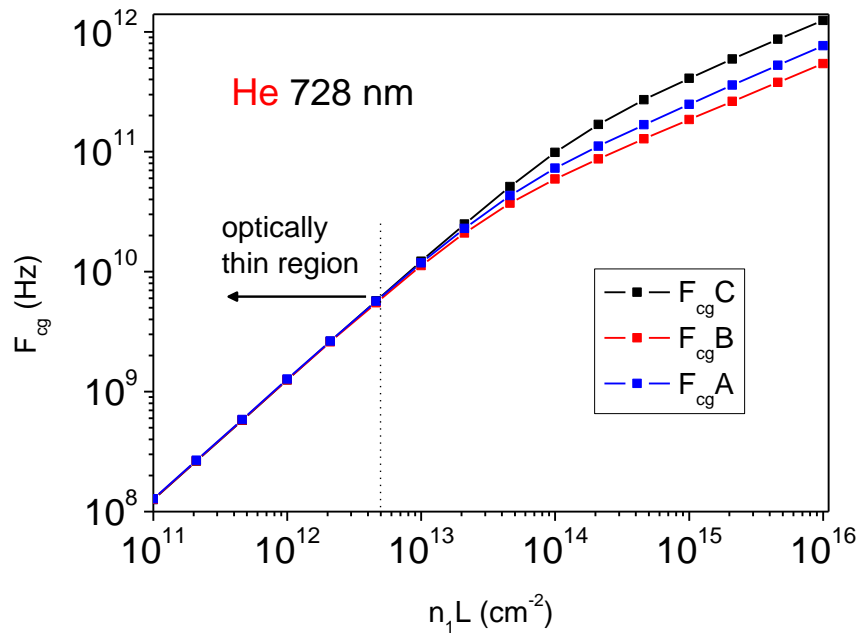


Figure 6.11 Some curves of growth for the He 728 nm line.

## 6.4 Estimation of the number density of He

### 6.4.1 He emission lines measurements

For the estimation of the number density of He atoms in the resonance  $2p^1P^0$  state, the emission spectra acquired for the plasma jet mapping will be evaluated in the following. The maxima of the emitted lines intensities for two different gas flows ( $F_A = 300 \text{ mL min}^{-1}$ ,  $F_B = \text{mL min}^{-1}$ ) along the jet axis ( $z = 0$ ) will be considered. A sequence of the spectra acquired between 690 and 740 nm for the bigger gas flow is given in Figure 6.12. The plots correspond to different positions along the  $x$ -axis (from 1 to 9 mm away from the capillary orifice) and for the maximum position along the  $z$ -axis ( $z = 0$ ), according to Figure 5.1 in the previous chapter.

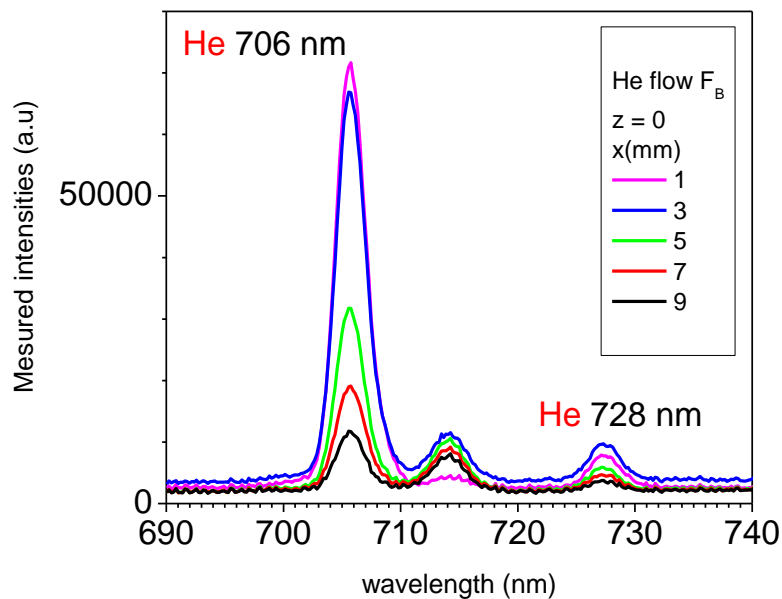


Figure 6.12 Section of some typical spectra measured along the plasma jet for different  $x$  positions (distance from capillary orifice: 1, 3, 5, 7, 9 mm) at  $z = 0$  (the position for the maximum of the measurable intensity along the  $z$ -axis).

The measured relative intensities of some He lines along the plasma jet for the two different gas flows are presented in Figure 6.13.

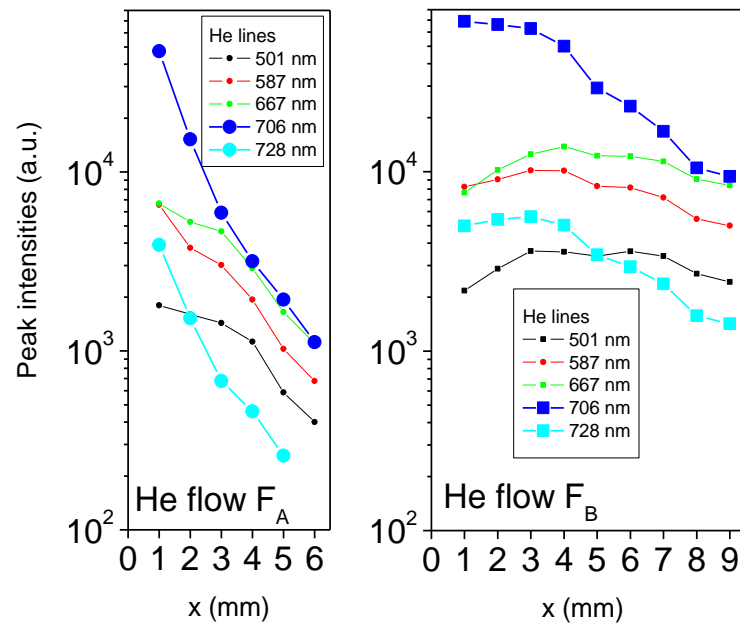


Figure 6.13 Peak intensities of He lines measured at  $z = 0$  in dependence on position  $x$  along the plasma jet.

In the following, evaluation only the 706 and 728 nm He lines will be considered. The ratio of their intensities against the  $x$ -position is given in Figure 6.14.

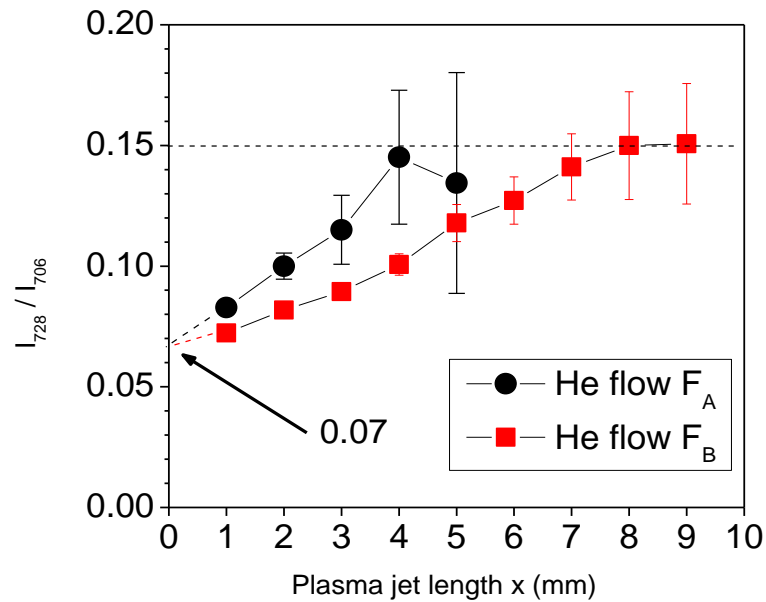


Figure 6.14 The variation of the peak intensities ratios  $I_{728}/I_{706}$  in dependence on  $x$  position along the plasma jet.

At the end of the jet, i.e. at positions where the intensities are still measurable, the ratio  $I_{728}/I_{706}$  takes the value of about 0.15 for both applied He flows as it can be observed from Figure 6.14. However, in both cases this ratio converges to the value of about 0.07 for  $x = 0$ , i.e. at the capillary orifice.

### 6.4.2 The optical thickness of considered lines

In the present case, a free burning He plasma jet which penetrates from the capillary into the air is considered. Initially, at  $x = 0$ , the He number density  $n_{He}$  has a maximum value  $n_{He}(0)$  which is defined by the atmospheric pressure and the temperature of the plasma gas. Generally, the  $x$ -dependence of the He number density can be described by  $n_{He}(x) = n_{He}(0)f_{He}(x)$ , where the function  $f_{He}(x)$  decreases with  $x$ . Since the pressure is constant, the air number density distribution along the  $x$ -axis is determined by  $n_{air}(x) = n_{air}(\infty)(1-f_{He}(x))$ . It cannot be determined whether the measured He lines are optically thin or not. However, since the measured intensity ratios are saturated at the end of the jet, one can assume that in this region (between 4 and 5 mm for lower gas flow, and between 7 and 9 mm at higher flow respectively) the He number density is small and the lines are optically thin. Thus, at the end of the jet the ratio of intensities of the considered lines can be written as:

$$\left. \frac{I_{728}}{I_{706}} \right|_{end} = \frac{r^{728}}{r^{706}} \frac{\lambda_{21}^{706}}{\lambda_{21}^{728}} \frac{n_2^{728}(end)}{n_2^{706}(end)} \frac{A_{21}^{728}}{A_{21}^{706}} = 0.15 \pm 0.02, \quad (6.14)$$

where  $n_2^\lambda(end)$  labels the number densities of relevant upper levels at the end of the jet on its axis ( $z = 0$ ). Even though the exact spectral response of the used optical spectrometer is not known, in the following procedure the value  $r^{728}/r^{706} = 1$  will be assumed, taking into consideration that the lines in present evaluation are very close in spectrum. Then, from Eq. (6.14) one obtains the population ratio:

$$\frac{n_2^{728}(end)}{n_2^{706}(end)} = \frac{728}{706} \frac{0.278}{0.18} (0.15 \pm 0.02) = 0.225 \pm 0.03. \quad (6.15)$$



### 6.4.3 The excitation temperatures

By introducing the Boltzmann density distribution into the expression of the density population, the following expression for the density ratio is obtained:

$$\frac{n_2^{728}(end)}{n_2^{706}(end)} = \frac{g_2^{728}}{g_2^{706}} \exp\left(-\frac{\Delta E}{kT_{exc}^{end}}\right) \quad (6.16)$$

and one can calculate the excitation temperature  $T_{exc}^{end}$  at the end of the jet as it follows:

$$\exp\left(-\frac{hc}{k} \frac{\Delta E (cm^{-1})}{T_{exc}^{end} (K)}\right) = \frac{3}{1} (0.225 \pm 0.03). \quad (6.17)$$

This yields the mean value  $\bar{T}_{exc}^{end} = 1.44 \times 1628 / \ln(0.675) \approx 6000$  K. When approaching the capillary orifice, this calculation yields lower excitation temperatures, which is quite opposite to the expected result. According to findings of Kunze et al. [100], the excitation temperatures in plasma bullets at  $x = 0$  are expected to be in the range of several thousand Kelvin (320000 K). This means that the expected number density ratio at the capillary orifice is:

$$\frac{n_2^{728}(x=0)}{n_2^{706}(x=0)} = \frac{g_2^{728}}{g_2^{706}} \exp\left(-1.44 \frac{1628}{T_{exc}^{x=0} (K)}\right) \approx \frac{g_2^{728}}{g_2^{706}} = \frac{1}{3}. \quad (6.18)$$

Consequently, the decrease of the  $I_{728}$  to  $I_{706}$  ratio for the approach to the capillary orifice can only be explained by an increase of the optical depth of the He 728 nm line.

### 6.4.4 The procedure to estimate the number density of He metastable

The basic assumption that has to be made for the following procedure is that the He 706 nm line remains optically thin in the vicinity of the capillary orifice,  $x \rightarrow 0$ . Considering this fact, the intensity ratio  $I_{728}/I_{706}$  at a given  $x$  position can be written according to the Eqs. (6.10) and (6.12) in section 6.3.4 as:

$$\left. \frac{I_{728}}{I_{706}} \right|_x = \frac{\frac{8\pi}{(\lambda_{21}^{728})^3} \frac{n_2^{728}(x) g_1^{728}}{n_1^{728}(x) g_2^{728}} F_{CG}^{728} [n_1^{728}(x) L_{eff}]}{\frac{1}{\lambda_{21}^{706}} n_2^{706}(x) A_{21}^{706} L_{eff}} \quad (6.19)$$

and simplified as follows:

$$\frac{I_{728}}{I_{706}} \Big|_x = 8\pi \frac{\lambda_{21}^{706} n_2^{728}(x) g_1^{728}}{(\lambda_{21}^{728})^3 n_2^{706}(x) g_2^{728} A_{21}^{706}} \frac{1}{n_1^{728}(x) L_{eff}} \frac{F_{CG}^{728} [n_1^{728}(x) L_{eff}]}{n_1^{728}(x) L_{eff}}. \quad (6.20)$$

Considering Eq. (6.18) from above, the expression (6.20) for  $x = 0$  yields:

$$\frac{F_{CG}^{728} [n_1^{728}(x=0) L_{eff}]}{n_1^{728}(x=0) L_{eff}} = \frac{1}{8\pi} \frac{(\lambda_{12}^{728})^3 g_2^{706}}{\lambda_{12}^{706} g_1^{728} A_{21}^{706}} \frac{I_{728}}{I_{706}} \Big|_{x=0}, \quad (6.21)$$

and introducing the corresponding numerical values yields:

$$\frac{F_{CG}^{728} [n_1^{728}(x=0) L_{eff}]}{n_1^{728}(x=0) L_{eff}} = \frac{1}{8\pi} \frac{(7.28 \times 10^{-5})^3 \cdot 3}{7.06 \times 10^{-5} \cdot 3} 2.78 \times 10^7 \times 0.07 = 4.2 \times 10^{-4} \text{ Hz cm}^2 \quad (6.22)$$

With known profile of the He 728 nm line, one can calculate the function on the left side of Eq. (6.22) above, which yields ambiguous values for  $n_1^{728}(x=0) L_{eff}$ , i.e. for the number density  $n_1^{728}(x=0)$  in the resonance state at the capillary orifice.

### 6.4.5 Density estimations

The parameters of the actual profile are not yet known. Nevertheless, using the calculated curves of growth in the previous section, one can estimate at least the lowest value for the number density of interest in present the experiment. First, one has to consider that at the capillary orifice the DBD burns in pure He. Second, according to the results found by Kunze et al [64, 100] and Xiong et al [99], the *He* lines are emitted only from hot plasma bullets, where the gas temperature is at least 1000 K. At that temperature, neglecting the impact broadening due to collisions with electrons, the line broadening parameters are as given by *case A* in Table 6.3 (section 6.3.6). In contrast to the physical situation in [64] ( $p_{Ar} = 20$  mbar), in the present case we have He at atmospheric pressure and the gas temperature in plasma bullets is expected to be higher than 1000 K. To study the influence of the increasing gas temperature, the value  $T = 2000$  K was arbitrarily chosen and the corresponding curve of growth was calculated (case B in Table 6.3). Here, the contribution to the Lorentz broadening due to electrons collisions still was neglected. In the third case (case C), the influence of an additional pressure broadening (due to electrons) was simulated for  $T = 1000$  K where

the total Lorentz FWHM was taken to be three times larger than in the case A. The values obtained for the quantity  $F_{CG}^{728}(n_1L)/n_1L$  were calculated from the Table 6.4 and plotted in Figure 6.15.

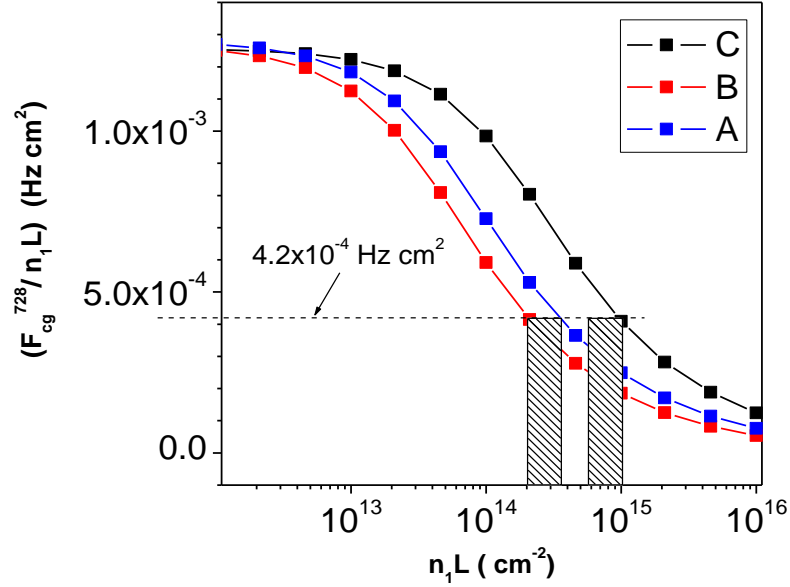


Figure 6.15 The number density estimation of the lower He state belonging to 728 nm transition

When no broadening due to electrons is included, the values for the curve of growth  $F_{CG}^{728}(n_1L)/n_1L$  obtained using Eq. (6.22) are plotted in Figure 6.15. It can be seen that the  $n_1^{728}(x=0)L_{eff}$  takes the values between  $2 \times 10^{14} \text{ cm}^{-2}$  and  $5 \times 10^{14} \text{ cm}^{-2}$  for gas temperatures ranging between 2000 K and 1000 K, respectively. Since  $L_{eff} \approx 0.1 \text{ cm}$ , the corresponding number density  $n_1^{728} \equiv n(2p^1P^0)$  in the resonance state at the capillary orifice is approximately in the range from  $2 \times 10^{15} \text{ cm}^{-3}$  to  $5 \times 10^{15} \text{ cm}^{-3}$  (about 1000 times smaller than the He ground-state atom density). This value is in accordance with the results obtained in chapter 4, when the maximum of  $N_2^+$  was obtained for a concentration of 140 ppm representing a density in the range of  $10^{15} \text{ cm}^{-3}$  from the total amount of gas at atmospheric pressure. Including electron broadening, this value becomes even higher.

### 6.4.6 Discussion, conclusion and outlook

Reviewing the initial assumptions made for the present evaluation procedure, the first one is included by the Eq. (6.19) given above where the He 706 nm was considered to be optically thin. However, if this assumption would not be correct, the value of the right side of Eq. (6.21) would be lower and the number density  $n_I^{728} \equiv n(2p^1P^0)$  would be higher than estimated above, respectively. Furthermore, if the condition given by Eq. (6.18) is not fulfilled, the value of the right side of Eq. (6.21) would be higher, which yields a lower value of the estimated number density. However, assuming an excitation temperature at the capillary orifice equal to that at the end of the jet (6000 K), the obtained values for  $n_I^{728} \equiv n(2p^1P^0)$  would be about 1.5 times lower than estimated above. Also, if the gas temperature would be different, for instance about 4000 K, then the estimated values would be two times lower. As conclusion, one could say that the present evaluation procedure indicates that the considered density amounts at least  $1 \times 10^{15} \text{ cm}^{-3}$ .

The behaviour of other measured He line intensities indicates that when approaching the capillary orifice, the decrease of their intensities becomes significant as it can be seen in Figure 6.13. This is obviously due to the increase of their optical thickness.

Time and space-resolved laser absorption as well as laser fluorescence measurements of one of the He lines of interest can give information about the gas temperature and the actual line broadening, as well as accurate data regarding the number density in the corresponding metastable state. Then, by combining these results with the data obtained by emission spectroscopy for other lines, one can get a full picture about the metastable density in the dielectric barrier capillary plasma jet discharge.

## 7 CONCLUSION AND OUTLOOK

A soft ionisation source that can be implemented to analytical devices like IMS and LC/MS was presented. This source is based on a dielectric capillary plasma jet discharge. Investigations to characterize the plasma by means of optical spectroscopy were performed and information about the processes that take place inside the plasma jet was obtained.

The plasma jet was implemented in an IMS device and tested using He, Ne and Ar as working gases. As nitrogen plays an important role for soft ionisation mechanism using the capillary dielectric barrier discharge investigations using mixtures of the rare gases with nitrogen in different concentration were used to produce the plasma jet. By acquiring the emission spectra of the plasma jet, it was found that only in the case of He the upper excited levels of the  $N_2^+$  first negative system ( $B^2\Sigma_u^+$ ) can be excited. This is based on the He metastables Penning ionisation. Increasing the concentration of nitrogen in the gas mixture, it was found that the population of the excited upper level of  $N_2^+$  first negative system ( $B^2\Sigma_u^+$ ) cannot exceed the population density of the metastables and this density is between 140 and 450 ppm of the He atoms in ground state. Pure He should be used and the reaction of Penning ionisation should take place in the vicinity of the water protonation process, to obtain the most sensitive IMS signal. This means that the Penning ionisation between He metastables and nitrogen should happen in the ionisation chamber outside the plasma capillary in the vicinity of the plasma jet. When Ne is used as working gas in the plasma jet, a small RIP is observed. This can only be explained by Penning ionisation, but the energy difference between Ne metastable state and the protonation level is bigger than the difference between  $N_2^+(X^2\Sigma_g^+)$  and the water protonation level. In the case of Ar, the metastable state is lower than the protonation level and therefore a RIP could not be measured.

The following investigation on the plasma jet was intended to get a mapping of the important species along the plasma jet. This was a good way to prove that there exists an optimal position where the upper excited levels of the  $N_2^+$  first negative system

( $B^2\Sigma_u^+$ ) can be excited due to Penning ionisation by He metastables. The distribution of intensities in the plasma jet of some relevant emission lines of the species involved in the energy transfer process (He 706 nm,  $N_2$  380 nm and  $N_2^+$  427 nm) have been presented for two different He flows. It was found that the plasma jet, which penetrates from the zone of the capillary barrier discharge into the atmosphere, has strongly non-homogeneous distribution of the ground-state particles along its axis while it is axially symmetric. Based on these experimental findings, a simplified model involving He and  $N_2$  reactive states was developed. It represents a semi-quantitative analysis of position-dependent energy transfer processes involving He,  $N_2$  and  $H_2O$  in their ground, excited and ionised states. The number density distributions of excited He,  $N_2^+$  and  $N_2$  along the plasma jet were simulated and compared with the intensity distributions of the corresponding optically thin spectral lines observed in the experiment. A general agreement between modelled and experimental results was found and confirmed by the reproduced position of maxima of the line intensity as well as by their shift towards larger distances from capillary orifice. It can be concluded that the main excitation path leading to the protonation of water in the He plasma jet penetrating in the air atmosphere starts with the collisions of He metastables and  $N_2$  molecules in air. Penning ionisation of nitrogen and subsequent energy transfer to the water molecules lead to an efficient water ionisation and protonation. Even though other energy transfers paths, like charge transfer might be considered, this is the most important one. In the described cascade de-excitation, several important branching ratios were determined approximately. In addition, a region in the plasma jet characterized by the most efficient subsequent protonation of sample molecules was identified.

In the previous investigations it was shown that the density of  $N_2^+(B^2\Sigma_u^+)$  excited state of the first negative system plays an important role in the process of water protonation and depends on the density of the He metastable density population. Thus, a new task arose, which is determination of the population density of the excited He state which populates through radiative decay the metastable level. This task was accomplished by the evaluation of the variation of the He emission lines along the plasma jet as they were measured for the plasma jet mapping.

Considering the broadening parameters of the emission lines for the case of the considered thin line, a simulation of the curve of growth was done from which the density population could be estimated. The He 706 nm was considered to be optically thin, and based on this assumption, the evaluation procedure indicates that the considered density population for  $n_I^{728} \equiv n(2p^1P^0)$  amounts at least to  $1 \times 10^{15} \text{ cm}^{-3}$ .

Time and space resolved laser absorption spectroscopy as well as laser fluorescence measurements for one of the interest He lines would be necessary. These could give information about the gas temperature and the actual line broadening, as well as accurate results in evaluating the population density in the corresponding metastable state. Then, by combining these results with the emission-spectroscopic data for other lines, one can get a full picture about the metastable density in the dielectric barrier capillary plasma jet discharge.





## 8 APPENDIX

### 8.1 Conversion of energy units

The following conversion of units is given according to *Spectrophysics* by A. P. Thorne [101].

$$1J(10^7 \text{ erg}) = 6.242 \times 10^{18} \text{ eV} \Rightarrow 5.034 \times 10^{22} \text{ cm}^{-1}$$

$$1 \text{ eV} = 1.602 \times 10^{-19} \text{ J} \Rightarrow 8065 \text{ cm}^{-1}$$

$$1 \text{ cm}^{-1} \Rightarrow 1.986 \times 10^{-23} \text{ J} = 1.240 \times 10^{-4} \text{ eV}$$

$$k = 1.380 \times 10^{-23} \text{ J} \cdot \text{K}^{-1} = 0.861 \times 10^{-4} \text{ eV} \cdot \text{K}^{-1} \Rightarrow 0.695 \text{ cm}^{-1} \cdot \text{K}^{-1}$$

$$hc = 1.98648 \times 10^{-23} \text{ J} \cdot \text{cm}^{-1} = 1.23985 \times 10^{-6} \text{ eV} \cdot \text{cm}^{-1}$$

### 8.2 Basic aspects of optical spectroscopy

A short presentation of the basic aspects regarding optical spectroscopy will briefly be presented and defined in the following part. For practical reasons, the cgs-units will be used here: in this specific area of atomic spectroscopy, which is the subject of this work, formulas and calculations are simpler in the cgs-system than in the MKS-system. The final results are always presented in MKS units. The notions used here are according to A.P. Thorne [101] and W. Demtröder [108]

**Spectral density of radiation  $\rho^\nu$  ( $\text{erg cm}^{-3} \text{ Hz}^{-1}$ ) and spectral intensity of radiation  $I^\nu$  ( $\text{erg cm}^{-2} \text{ s}^{-1} \text{ Hz}^{-1}$ )**

The spectral density of radiation is the energy emitted at a given frequency  $\nu$ (Hz) per unit volume and per unit frequency interval  $d\nu$ . For example, in the case of blackbody radiation this is defined as:

$$\rho^\nu(\text{erg cm}^{-3} \text{ Hz}^{-1}) = \frac{8\pi\nu^2}{c^3} \frac{h\nu}{\exp(h\nu / kT) - 1} \quad (\text{A.1})$$

Here, the temperature is given in K and the values for  $c$ ,  $h$ , and  $k$  are:  $3 \times 10^{10} \text{ cm s}^{-1}$ ,  $6.625 \times 10^{-27} \text{ erg s}$ , and  $1.38 \times 10^{-16} \text{ erg K}^{-1}$ , respectively.

The spectral intensity is related to spectral density via  $I^\nu = \rho^\nu c$ , it is defined as the energy emitted per unit area, time and frequency.

### The absorption coefficient $k(\nu)$ ( $\text{cm}^{-1}$ ) and its frequency dependence

When a beam of light is passing in  $y$ -direction through a thin layer containing atoms which are characterized by an absorption line produced by the  $1 \rightarrow 2$  transition, the change of the spectral intensity  $dI^\nu(\nu, y)$  at the position  $y$  is proportional to the incident spectral intensity  $I^\nu(\nu, y)$  and the layer thickness  $dx$  (cm) as follows:

$$dI^\nu(\nu, y) = -k_{12}(\nu) I^\nu(\nu, y) dy. \quad (\text{A.2})$$

The frequency-dependent factor  $k_{12}(\nu)$  ( $\text{cm}^{-1}$ ), i.e. the absorption coefficient for the  $1 \rightarrow 2$  transition, is usually defined by:

$$k_{12}(\nu) = \frac{\lambda_{12}^2}{8\pi} n_1 \frac{g_2}{g_1} A_{21} P_{12}(\nu). \quad (\text{A.3})$$

The significance and the corresponding units in the above equation to obtain the absorption coefficient  $k_{12}(\nu)$  in  $\text{cm}^{-1}$  are:  $\lambda_{12}$  is the wavelength line in cm,  $n_1$  is the number density of absorbing atoms in the lower state in  $\text{cm}^{-3}$ ,  $g_1$  and  $g_2$  are the statistical weights of the lower and upper state,  $A_{21}$  is the radiative transition probability in  $\text{s}^{-1}$ , and  $P_{12}(\nu)$  is the normalized line profile in  $\text{Hz}^{-1}$ .

The normalized line profile (normalized absorption distribution over frequencies  $\nu$  in Eq. (A.3) fulfills the following condition:

$$\int P_{12}(\nu) d\nu = 1. \quad (\text{A.4})$$

According to Eq. (A.2), the transmitted spectral intensity after passing a finite absorption column (length:  $L$ ) is given by:

$$I^\nu(\nu, L) = I^\nu(\nu, 0) \exp[-k_{12}(\nu) L], \quad (\text{A.5})$$

which is the well known Beer's absorption law. One should keep in mind that Eq. (A.2) is valid for weak incident spectral density, so that the energy, which is absorbed and

spontaneously re-emitted energy in  $x$ -direction, is negligible. Otherwise, the induced emission should also be taken into account, which is done by an additional term on the right side of Eq. (A.2). This leads to the non-linear absorption and saturation.

### Simultaneous emission and absorption of a spectral line

Considering a plasma column, i.e. an emitting and simultaneously absorbing medium with relevant number densities  $n_1$  and  $n_2$ , the spontaneous emission done by transition  $2 \rightarrow 1$  is followed by absorption  $1 \rightarrow 2$ , respectively. Spontaneous emission is distributed spatially isotropic and an exact radiometric calculation would require the introduction of the plasma cross section and the corresponding space angles. In the present case the one-dimensional geometry is assumed, i.e. the diameter of the plasma column is small in comparison with the column length  $L$ . Furthermore, it is assumed that the plasma column is homogeneous, which means that  $n_1$  and  $n_2$  do not depend on the position  $y$ . In this case (see Figure 8.1), the difference  $dI_{21}^{\nu}(\nu, x)$  between the incident and out coming intensity of the spectral line related to a thin layer (thickness:  $dy$ ) at position  $y$  is:

$$dI_{21}^{\nu}(\nu, y) = \varepsilon_{21}(\nu) dy - k_{12}(\nu) I_{21}^{\nu}(\nu, y) dy. \quad (\text{A.6})$$

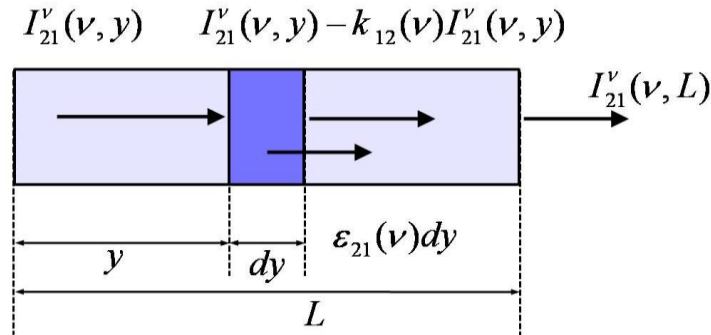


Figure 8.1 Geometry for the calculation the intensity of a spectral line emitted from a plasma.

The linear spectral emissivity of an emission line emerging by the corresponding  $2 \rightarrow 1$  transition is labeled by  $\varepsilon_{21}(\nu)$  in Eq. (A.6). It is proportional to the energy of emitted photons, the radiative transition probability  $A_{21}$ , the number density  $n_2$  of the atoms in the upper state and to the emission line profile  $P_{21}(\nu)$ :

$$\varepsilon_{21}(\nu) \propto h\nu_{12} A_{21} n_2 P_{21}(\nu). \quad (\text{A.7})$$

In the next step, the expression (A.6) is re-written in the following form:

$$\frac{d}{dy} I_{21}^{\nu}(\nu, y) = k_{12}(\nu) \left[ \frac{\varepsilon_{21}(\nu)}{k_{12}(\nu)} - I_{21}^{\nu}(\nu, y) \right]. \quad (\text{A.8})$$

The line emission profile  $P_{21}(\nu)$  equals to the absorption profile  $P_{12}(\nu)$ , which follows from the relationship between the Einstein coefficients for emission and absorption.

This means that the ratio  $I_0 = \varepsilon_{21}(\nu)/k_{12}(\nu)$  does not depend on frequency:

$$I_0 = \varepsilon_{21}(\nu)/k_{12}(\nu) \propto \frac{8\pi hc n_2 g_1}{\lambda_{12}^3 n_1 g_2}. \quad (\text{A.9})$$

Since the medium is supposed to be homogeneous (number densities do not depend on  $y$ ), it is convenient to introduce the quantity  $J_{21}^{\nu}(\nu, y) = I_0 - I_{21}^{\nu}(\nu, y)$ . With this substitute, the equation (A.8) becomes:

$$\frac{d}{dy} J_{21}^{\nu}(\nu, y) = -k_{21}(\nu) J_{21}^{\nu}(\nu, y). \quad (\text{A.10})$$

After integration from  $y = 0$  to  $y = L$ , Eq. (A.10) yields:

$$J_{21}^{\nu}(\nu, L) = J_{21}^{\nu}(\nu, 0) \exp[-k_{21}(\nu)L]. \quad (\text{A.11})$$

Then, the expression for the emitted spectral line intensity related to the whole plasma column is given by:

$$I_{21}^{\nu}(\nu, L) = \frac{\varepsilon_{21}(\nu)}{k_{21}(\nu)} \{1 - \exp[-k_{21}(\nu)L]\} \propto \frac{8\pi hc n_2 g_1}{\lambda_{12}^3 n_1 g_2} \{1 - \exp[-k_{21}(\nu)L]\} \quad (\text{A.12})$$

### The registered line intensities

The spectra are acquired with a spectrometer, which is characterized by its (normalized) instrumental profile  $P_S(\nu)$  and its spectral response  $r(\nu)$ . The measured intensities are displayed in arbitrary units. The registered line intensity is a convolution of the instrumental profile and the observed spectral line intensity as follows:

$$I_{21}^M(\nu, L) \propto \int_{-\infty}^{+\infty} r(\xi) P_S(\xi) I_{21}^{\nu}(\nu - \xi, L) d\xi. \quad (\text{A.13})$$

Usually, the spectral response varies slowly within the profile of the particular line as well as within the instrumental profile, i.e. it can be taken as constant in the actual integration frequency range:

$$I_{21}^M(\nu, L) \propto r(\nu_{21}) \int_{-\infty}^{+\infty} P_S(\xi) I_{21}^\nu(\nu - \xi, L) d\xi. \quad (\text{A.14})$$

Here, two extreme cases regarding the widths of  $P_S(\nu)$  and  $P_{21}(\nu)$  can be considered. In the case that the width of the line profile is much narrower than the width of the spectrometer profile (case a), the subintegral function  $I_{21}^\nu(\nu - \xi, L)$  in Eq. (A.14) is a sharp peak at the frequency  $\nu_{21}$  and can be formally treated as the  $\delta$ -function:

$$I_{21}^\nu(\nu - \xi, L) \approx \delta(\nu - \nu_{21} - \xi) \int_{-\infty}^{+\infty} I_{21}^\nu(\nu, L) d\nu. \quad (\text{A.15})$$

Then, the formula (A.14) yields:

$$I_{21}^M(\nu, L)|_a \propto r(\nu_{21}) P_S(\nu - \nu_{21}) \int_{-\infty}^{+\infty} I_{21}^\nu(\nu, L) d\nu. \quad (\text{A.16})$$

In case a, the shape of the measured line reflects the exact form of the instrumental profile and the signal is proportional to the integral of the intensity of the spectral line. This integral (integration of Eq. (A.12)) depends on the line parameters, the line profile, the relevant number densities and the length of the observed emitting column.

If the instrumental profile is much narrower than the line profile (case b) the instrumental profile can be represented by the  $\delta$ -function:

$$P_S(\xi) \approx \delta(\xi - \nu_{21}) \int_{-\infty}^{+\infty} P_S(\nu) d\nu. \quad (\text{A.17})$$

In this case, the Eq. (A.14) yields the following expression:

$$I_{21}^M(\nu, L)|_b \propto r(\nu_{21}) I_{21}^\nu(\nu - \nu_{21}, L) \int_{-\infty}^{+\infty} P_S(\nu) d\nu. \quad (\text{A.18})$$

In case b), the measured intensity follows the shape of the emitted spectral intensity as defined by Eq. (A.12). The integral of the instrumental profile is a constant. For instance, if  $P_S(\nu)$  is defined in the normalized form as mentioned above, then the integral in the expression (A.18) is equal to 1.

### Optical depth and optical thickness of spectral lines

The dimensionless quantity  $k_{21}(\nu)L$  is the so-called “*optical depth*” of the considered spectral line. As one can take from Eq. (A.12), only in the optically thin case, i.e. when  $k_{21}L \ll 1$  applies, the spectral intensity of the line follows the shape of the actual line profile:

$$I_{21}^V(\nu, L) \Big|_{thin} \propto h\nu_{12} A_{21} n_2 L P_{12}(\nu) \quad (\text{A.19})$$

In practice, the lines can be considered as optically thin when the optical depths take values less than 0.05. Otherwise, the lines are treated to be optically thick and the general form of the emitted spectral intensity is defined by Eq. (A.12). In case a defined above, the spectrometer integrates the spectral intensity and the measured line intensity of an optically thin line, according to Eqs. (A.4), (A.16) and (A.19) is given by:

$$I_{21}^M(\nu, L) \Big|_{a, thin} \propto r(\nu_{21}) h\nu_{12} A_{21} n_2 L P_S(\nu - \nu_{21}). \quad (\text{A.20})$$

### Normalized line profiles

The broadening of the kernels of spectral lines usually is governed by the Doppler effect and the collisions between the emitting particles and surrounding perturbers. The resulting line profiles are both analytical functions as given below.

#### The Doppler (Gauss) broadening:

$$P_{12}^D(\nu) = \frac{2\sqrt{\ln 2}}{\sqrt{\pi} \Delta_D} \exp \left[ - \left( \frac{\nu - \nu_{21}}{\Delta_D} 2\sqrt{\ln 2} \right)^2 \right], \quad (\text{A.21})$$

where  $\Delta_D$  is the Doppler FWHM given by:

$$\Delta_D (Hz) = \frac{2\sqrt{\ln 2}}{\lambda_{12}} \sqrt{2kT/M}. \quad (\text{A.22})$$

In the case of He,  $\Delta_D$  amounts to:

$$\Delta_D (Hz) = 1.07 \times 10^4 \frac{\sqrt{T(K)}}{\lambda_{12}(cm)}. \quad (\text{A.23})$$

**The Lorentz (pressure) broadening:**

$$P_{21}^L(\nu) = \frac{2}{\pi \Delta_L} \frac{1}{4 \left( \frac{\nu - \nu_{21}}{\Delta_L} \right)^2 + 1}, \quad (\text{A.24})$$

where  $\Delta_L(\text{Hz})$  is the Lorentz FWHM, which is given as the product of perturber number density of the atoms  $n_p$  and the impact broadening parameter  $\gamma_P^V$  ( $\text{cm}^3 \text{s}^{-1}$ ):

$$\Delta_L = \gamma_P^V n_p. \quad (\text{A.25})$$

**The Voigt profile**

In general, both Doppler and Lorentz broadening mechanisms occur and the resulting profile is their convolution:

$$P_{12}^V(\nu) = \int P_{12}^D(\nu - x) P_{12}^L(x) dx, \quad (\text{A.26})$$

which is well known as the Voigt profile. There is no analytical solution for Eq. (A.26) and for each particular case, numerical calculations are needed. Nevertheless, for given Doppler and Lorentz full widths at half-maximum, in literature one can find approximate analytical expressions for the corresponding Voigt profiles.

**Multiple Lorentz broadening**

Lorentz broadening occurs due to collisions between the emitting atoms and surrounding perturbers in a medium (pressure broadening). If we have a monoatomic medium, then the Lorentz broadening is caused by collisions with atoms of the same kind (homonuclear collisions, self-broadening). If additional other perturbers (atoms, molecules, electrons) are present, the resulting broadening is a convolution of the particular Lorentz profiles. The resulting line shape is again of the Lorentz form, where the resulting  $\Delta_L$  equals to the sum of the particular contributions.

**8.3 The curve of growth for He 728 nm determined using Origin software**

Using the Origin8 software from OriginLab Corporation, the curve of growth for the population density of the He excited state on the upper level corresponding to the

728 nm emission line was calculated. Atmospheric pressure and a temperature of  $T_{\beta} = 2000$  K were assumed. The basic parameters corresponding to this transition are: the wavelength  $\lambda_{12} = 7.28 \times 10^{-5}$  cm, the statistical weights of the corresponding levels transitions  $g_2 = 1$ ,  $g_1 = 3$  and the Einstein coefficient for spontaneous emission  $A_{21} = 0.18 \times 10^8$  s<sup>-1</sup>. The Origin project file contains a worksheet with nine columns that are named and defined as described in the following.

According to the previous section, the acquired spectral lines are broadened. The corresponding broadening parameters are given as constants in two separate columns: Lorentz broadening:

**col(L)**  $\equiv \Delta_L = 1.5 \times 10^{10}$  (Hz) and Doppler broadening:

**col(D)**  $\equiv \Delta_D = 6.5 \times 10^9$  (Hz). The parameters of the corresponding Voigt profile are calculated in columns **col(V)** and **col(P<sub>0</sub>)** by setting the column values as follows:

$$\begin{aligned} \mathbf{col(V)} &= (\mathbf{col(L)} / 2) + ((\mathbf{col(L)} / 2)^2 + (\mathbf{col(D)})^2)^{0.5} \equiv \Delta_V = \\ &\Delta_L / 2 + \sqrt{(\Delta_L / 2)^2 + \Delta_D^2} = 1.74247 \times 10^{10} \text{ (Hz)} \end{aligned}$$

**col(P<sub>0</sub>)**  $\equiv P_0^V = 3.844449 \times 10^{-11}$  (Hz<sup>-1</sup>) according to Eq. (6.6) in Sec. 6.3.3.

The normalized line profile represented in **col(P7)** is a normalized Pearson-7 function which is calculated as defined by Eq. (6.7) in Sec. 6.3.3. Here, for the parameter **p**, a value of 1 was chosen:

$$\mathbf{col(P7)} = \mathbf{col(P_0)} / ((1 + 4 * (\mathbf{col(A)})^2 / (1 * (\mathbf{col(V)})^2)^1).$$

The column A (**col(A)**) represents the frequency scale in Hz. For practical reasons, the line profile is centered to the line frequency (**col(A)**  $\equiv \nu - \nu_{21}$ ). The **col(A)** was defined in three steps in the following manner:

i) **col(A)** = i for i = 1 to 4000 (i the number of steps)

ii) **col(A)** = **col(A)** - 2000 (centering),

iii) **col(A)** = **col(A)** · 5E8 (setting the A-scale to the absolute frequency-scale (Hz)).



To get the correct values for the relevant integral over the frequencies, numerical calculations require a sufficiently wide (finite) range of summation and sufficiently small summation steps. To reproduce the line kernel correctly, the summation steps should be at least ten times smaller than the FWHM of the line. In the present case (see the broadening section) the frequency steps ( $5 \times 10^8 \text{ s}^{-1}$ ) are arbitrarily chosen to be around 3.5 times below this requirement.

A check of the integral (summation) of the column values for **col(P7)** shows if the chosen number of frequency steps (yielding the finite integration range) is sufficient. The product of this sum with the step width  $5 \times 10^8$  should be near to 1. However, the number of steps (4000) was chosen by testing the shape of the subintegral function in Eq.(A.4) which is defined in **col(F)** as it follows below.

The column **col(n1L)** represents the variable  $n_1L$  ( $\text{cm}^{-2}$ ). To make the evaluation steps more clear, the value of this variable is defined as follows:

**col(n1L)** → set column values → **col(n1L)** = chosen value in  $\text{cm}^{-2}$ .

After setting the data in **col(L)**, **col(D)**, **col(V)**, **col(Po)** and **col(P7)**, the exponent in the subintegral function (optical depth), given by Eq. (6.13) in section 6.3.5 is calculated in **col(OD)** for a chosen particular value in **col(n1L)** as follows:

$$\mathbf{col(OD)} = ((7.28\text{E} - 5)^2 / (8 \cdot 3.14)) \cdot (1/3) \cdot (0.18\text{E}8) \cdot \mathbf{col(P7)} \cdot \mathbf{col(n1L)}$$

After setting the column values in **col(OD)**, the subintegral function given in Eq. (6.13) in section 6.3.5 is calculated in the **col(F)** as follows:

$$\mathbf{col(F)} = 1 - \exp(-\mathbf{col(OD)})$$

The validity of the integration procedure should be tested on **col(P7)** and **col(F)**.

Test 1. The normalization of the P7 profile

The integral of *P7* over the frequency range should be equal to 1. When setting the data in **col(P7)**, one can calculate the sum of column values as follows: **Analysis** → **Statistics on columns** → **Data1**. In the resulting window Data1 the sum amounts to  $2.0998 \times 10^{-9} \text{ Hz}^{-1}$ . This value multiplied by the frequency step  $5 \times 10^8 \text{ Hz}$  yields the integral of *P7* over the frequencies equal to 1.0499. The deviation from 1 is a matter of

the chosen parameter  $p = 1$  (see 6.1.3. above). It should be slightly adjusted ( $p = 1.061$ ) to obtain the integral of  $P7$  over the frequencies closer to 1. This correction was introduced in the windows Test2 and Test3.

Test 2: the frequency steps.

When plotting the  $P7$ , one can see that the chosen frequency steps are sufficiently small for correct reproduction of the profile in the line kernel as can be seen from Figure 8.2.

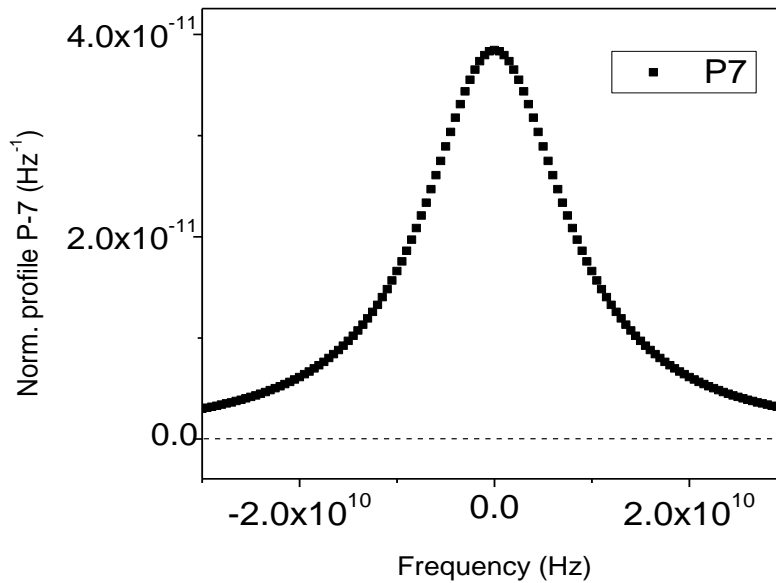


Figure 8.2 Frequency steps.

Test3: the frequency range.

With the chosen value  $n_l L = 1 \times 10^{17} \text{ cm}^{-2}$  in **col(n1L)**, the subintegral function  $F17$  was calculated and plotted in Figure 8.3 together with  $F16$  ( $n_l L = 1 \times 10^{16} \text{ cm}^{-2}$ ) against the frequency. The latter is calculated in the window Test3b. As one can see from Figure 8.3, the chosen integration frequency range (from  $-3 \times 10^{12} \text{ Hz}$  to  $+3 \times 10^{12} \text{ Hz}$ ) is not large enough for the integration over the entire range of  $F17$ , i.e. when  $n_l L = 1 \times 10^{17} \text{ cm}^{-2}$ . In that case, one should enlarge the number of steps (now: 4000). However, the calculation presented in the following section will be performed for the values  $n_l L$  up to  $1 \times 10^{16} \text{ cm}^{-2}$  so that the chosen frequency range can be taken as appropriate.

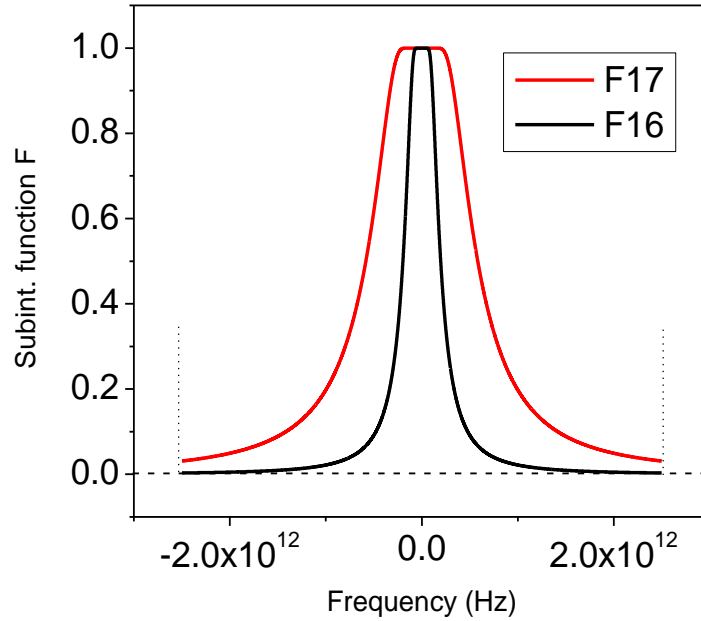


Figure 8.3 Testing the frequency integration range.

In the present example, the evaluation was performed for the values of the variable  $n_l L$  ( $\text{cm}^{-2}$ ) equal to  $a \times 10^b$  ( $\text{cm}^{-2}$ ), where  $a = 1, 2.1$  and  $4.6$  while  $n = 11, 12 \dots 16$ . The chosen steps are nearly equidistant on a logarithmic scale. For each value defined in **col(n1L)**, the column **col(OD)** and subsequently **col(F)** were calculated. When by multiplying the sum of calculated values in the **col(F)** with the value of the frequency steps, one obtains the corresponding value of the curve of growth  $F_{cg}(n_l L)$ .

## 8.4 Abel transformation

The following procedure applied in case of cylindrical symmetry of light sources called Abel's inversion is according to Lochte-Holtgreven [109]. In the case of a non-homogenous optically thin plasma, different plasma layers, each having an individual emissivity and an individual thickness contribute to the observed intensity. In return, in plasma analysis from the observed integrated intensity the individual plasma layers of different emissivity have to be found. The solution of this problem is not unambiguous and no general solution can be given. If, however, the symmetry of the light source is known, a solution is possible.

In the case of a cylindrical or spherical symmetry of the light source the observed projected intensities can be transformed into the radial intensity distribution within the plasma.

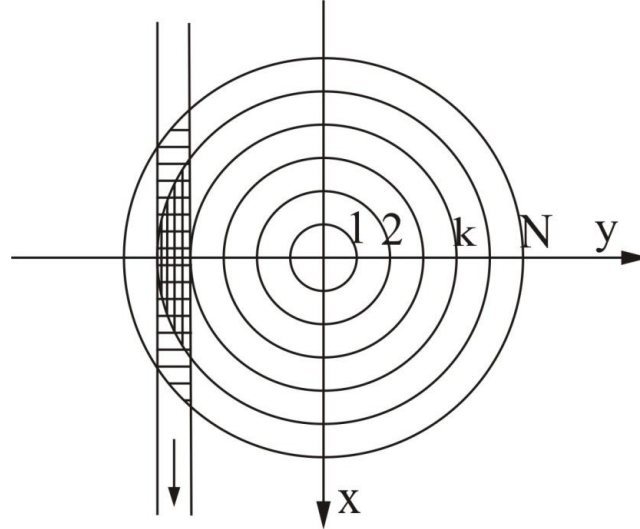


Figure 8.4 Subdivision of a plasma column into cylinders. X axis is the direction of observation. After W. Lochte-Holtgreven [109].

Let the axis of symmetry be denoted as z-axis (see Figure 8.4 ). We observe a circular plasma disc edge on, the  $x$  coordinate pointing from the axis towards the observer, the  $y$ -axis perpendicular to  $x$ .  $I(y)$  denotes the intensity of the radiation integrated over the  $x$  direction at a distance  $y$  from the  $xz$  plane. The local emissivity of the plasma at a distance  $r$  from the axis is  $\varepsilon(r)$ , then  $I(y)$  is related to  $\varepsilon(r)$  by:

$$I(y) = 2 \int_0^{\sqrt{R^2 - y^2}} \varepsilon(r) dx = 2 \int_y^R \frac{\varepsilon(r) r dr}{\sqrt{r^2 - y^2}}, \quad (\text{A.27})$$

where  $R$  is the radius for which  $\varepsilon(r)$  becomes zero. An inversion yields the desired quantity  $\varepsilon(r)$ :

$$\varepsilon(r) = -\frac{1}{\pi} \int_r^R \frac{dI(y)}{dy} \frac{dy}{\sqrt{(y^2 - r^2)}}. \quad (\text{A.28})$$

As Eq. (A.27) is of the Abel type, Eq. (A.28) is the corresponding Abel inversion. A large number of papers have appeared to handle the solution of these equations. Four different methods have been used:

a) graphical integration,

b) 1: expansion of the integral Eq. (A.27) into a set of linear equations given by:

$$I(y_k) = \sum_{i=k}^N a_{ik} \varepsilon(r_i)$$

2: a method similar to the one discussed above, but using an inverse matrix:

$$\varepsilon(r_i) = \sum_{i=k}^N b_{ik} I(y_k)$$

c) expansion of the integral Eq. (A.28) into a set of linear equations

$$\varepsilon(r_i) = \sum_{i=k}^N \beta_{ik} I'(y_k)$$

d) approximation of  $I(y)$  by polynomials. The solution of Eq. (A.27) of (A.28) is done by use of computer.



## BIBLIOGRAPHY

1. Crookes, W., *On the illumination of lines of molecular pressure, and the trajectory of molecules*. Phil. Trans. R. Soc., 1879. **170**: p. 135-164.
2. Langmuir, I., *Oscillations in ionized gases*. Proc. Nat. Acad. Sci. U.S. , 1928. **14**(8): p. 627-637.
3. Tonks, L. and I. Langmuir, *Oscillations in Ionized Gases*. Physical Review 1929. **33**: p. 195-211.
4. Popa, G. and L. Sirghi, *Bazele fizicii plasmei*. 2000, Iasi: Ed. Universitatii.
5. Conrads, H. and M. Schmidt, *Plasma generation and plasma sources*. Plasma Sources Sci. Technol., 2000. **9**: p. 441-454.
6. Kong, P., *Atmospheric-pressure plasma process and applications*, in *SOHN International Symposium On Advanced Processing of Metals and Materials; Principles, Technologies and Industrial Practice*. 2006.
7. Lieberman, M.A. and A.J. Lichtenberg, *Principles of Plasma Discharges and Materials Processing*. 2005, Hoboken, New Jersey.: John Wiley & Sons, Inc.
8. Braithwaite, N.S.J., *Introduction to gas discharges*. Plasma Sources Sci. Technol., 2000. **9**: p. 517-527.
9. Franzke, J., *The micro-discharge family (dark, corona, and glow-discharge) for analytical applications realized by dielectric barriers*. Anal. Bioanal. Chem, 2009. **395**: p. 549-557.
10. Janasek, D., J. Franzke, and A. Manz, *Scaling and the design of miniaturized chemical-analysis systems*. Nature, 2006. **442**: p. 374-380.
11. Iza, F., et al., *Microplasmas: Sources, Particle Kinetics, and Biomedical Applications*. Plasma Process. Polym., 2008. **5**: p. 322-344.
12. White, A.D., *New Hollow Cathode Glow Discharge*. J. Appl. Phys, 1959. **30**(5): p. 711-719.
13. Foest, R., M. Schmidt, and K. Becker, *Microplasmas, an emerging field of low-temperature plasma science and technology*. International Journal of Mass Spectrometry, 2006. **248**: p. 87-102.
14. Miclea, M. and F. J., *Analytical Detectors Based on Microplasma Spectrometry*. Plasma Chem. Plasma Process, 2007. **27**: p. 205-224.
15. The European Physical Journal D, Atomic, Molecular, Optical and Plasma Physics, 2010. **60**(3).
16. Walsh, J.L., J.J. Shi, and M.G. Konga, *Contrasting characteristics of pulsed and sinusoidal cold atmospheric plasma jets*. Appl. Phys. Lett., 2006. **88**: p. 171501-1 - 171501-3.

17. Iza, F. and J.A. Hopwood, *Self-organized filaments, striations and other nonuniformities in nonthermal atmospheric microwave excited microdischarges*. IEEE Trans. Plasma Sci., 2005. **33**(2): p. 306-307.
18. Muller, L., et al., *Self-organized filaments in dielectric barrier glow discharges*. IEEE Trans. Plasma Sci., 1999. **27**(1): p. 20-21.
19. Takano, N. and K.H. Schoenbach, *Self-organization in cathode boundary layer discharges in xenon*. Plasma Sources Sci. Technol., 2006. **15**: p. S109-S117.
20. Broekaert, J.A.C., *The development of microplasmas for spectrochemical analysis*. Anal. Bioanal. Chem, 2002. **374**: p. 182-187.
21. Becker, K.H., K.H. Schoenbach, and J.G. Eden, *Microplasmas and applications*. J. Phys. D: Appl. Phys., 2006. **39**: p. R55-R70.
22. Kogelschatz, U., *Applications of Microplasmas and Microreactor Technology*. Contrib. Plasma Phys., 2007. **47**(1-2): p. 80-88.
23. C.Tendero, et al., *Atmospheric pressure plasmas: A review*. Spectrochimica Acta Part B, 2006. **61**(2-30).
24. Yokoyama, T., et al., *The mechanism of the stabilisation of glow plasma at atmospheric pressure*. J. Phys. D: Appl. Phys., 1990. **23**: p. 1125-1128.
25. Massines, F. and G. Gouda, *A comparison of polypropylene-surface treatment by filamentary, homogeneous and glow discharges in helium at atmospheric pressure*. J. Phys. D: Appl. Phys., 1998. **31**: p. 3411-3420.
26. Goossens, O., et al., *Application of atmospheric pressure dielectric barrier discharges in deposition, cleaning and activation*. Surface and Coatings Technology, 2001. **142-144**: p. 474-481.
27. Kogelschatz, U., *Dielectric-barrier Discharges: Their History, Discharge Physics, and Industrial Applications*. Plasma Chem. Plasma Process, 2003. **23**(1): p. 1-46.
28. Massines, F., et al., *Experimental and theoretical study of a glow discharge at atmospheric pressure controlled by dielectric barrier*. Journal of Applied Physics, 1998. **83**(6): p. 2950-2957.
29. Wagner, H.-E., et al., *The barrier discharge: basic properties and applications to surface treatment*. Vacuum, 2003. **71**: p. 417-436.
30. He, Y., et al., *Dielectric Barrier Discharge-Induced Chemiluminescence: Potential Application as GC Detector*. Analytical Chemistry, 2007. **79**: p. 4674-4680.
31. Zhu, Z., et al., *Microplasma Source Based on a Dielectric Barrier Discharge for the Determination of Mercury by Atomic Emission Spectrometry*. Anal. Chem., 2008. **80**: p. 8622-8627.
32. Zhu, Z., et al., *Determination of Se, Pb, and Sb by atomic fluorescence spectrometry using a new flameless, dielectric barrier discharge atomizer*. Spectrochimica Acta Part B, 2008. **63**: p. 431-436.



33. Laroussi, M. and T. Akan, *Arc-Free Atmospheric Pressure Cold Plasma Jets: A Review*. Plasma Process. Polym., 2007. **4**: p. 777-788.
34. Schütze, A., et al., *The Atmospheric-Pressure Plasma Jet: A Review and Comparison to Other Plasma Sources*. IEEE Transactions on Plasma Science, 1998. **26**(6): p. 1685-1684.
35. Laimer, J. and H. Störi, *Recent Advances in the Research on Non-Equilibrium Atmospheric Pressure Plasma Jets*. Plasma and Fusion Research: Rapid Communications, 2007. **4**: p. 266-274.
36. Coulombe, S., et al., *Miniature atmospheric pressure glow discharge torch (APGD-t) for local biomedical applications\**. Pure Appl. Chem., 2006. **78**(6): p. 1147-1156.
37. Zhang, J., et al., *A novel cold plasma jet generated by atmospheric dielectric barrier capillary discharge*. Thin Solid Films, 2006. **507-507**: p. 404-408.
38. Forster, S., C. Mohr, and W. Viol, *Investigations of an atmospheric pressure plasma jet by optical emission spectroscopy*. Surface and Coatings Technology, 2005. **200**: p. 827-830.
39. Duan, Y., C. Huang, and Q. Yu, *Low-temperature direct current glow discharges at atmospheric pressure*. IEEE Transactions on Plasma Science, 2005. **33**(2): p. 328-329.
40. Laroussi, M. and X. Lu, *Room-temperature atmospheric pressure plasma plume for biomedical applications*. Appl. Phys. Lett., 2005. **87**: p. 113902-1 - 113902-3.
41. Laroussi, M., et al., *Inactivation of Bacteria by the Plasma Pencil*. Plasma Process. Polym., 2006. **3**: p. 470-473.
42. Teschke, M., et al., *High-speed photographs of a dielectric barrier atmospheric pressure plasma jet* IEEE Transactions on Plasma Science, 2005. **33**(2): p. 310 - 311.
43. Chen, G., et al., *The preliminary discharging characterization of a novel APGD plume and its application in organic contaminant degradation*. Plasma Sources Sci. Technol., 2006. **15**: p. 603-608.
44. Cheng, C., Z. Liye, and R.-J. Zhan, *Surface modification of polymer fibre by the new atmospheric pressure cold plasma jet*. Surface and Coatings Technology, 2006. **200**: p. 6659-6665.
45. Kim, D.B., et al., *Study of geometrical and operational parameters controlling the low frequency microjet atmospheric pressure plasma characteristics*. Appl. Phys. Lett., 2006. **89**: p. 061502-1 -061502-3.
46. Koinuma, H., H. Ohkubo, and T. Hashimoto, *Development and application of a microbeam plasma generator*. Appl. Phys. Lett., 1992. **60**(7): p. 816-817.
47. Janca, J., et al., *HF plasma pencil —new source for plasma surface processing*. Surface and Coatings Technology, 1999. **116-119**: p. 547-551.

48. Stoffels, E., et al., *Plasma needle: a non-destructive atmospheric plasma source for fine surface treatment of (bio)materials*. Plasma Sources Sci. Technol., 2002. **11**: p. 383-388.
49. Foest, R., et al., *RF Capillary Jet - a Tool for Localized Surface Treatment*. Contrib. Plasma Phys., 2007. **47**(1-2): p. 119-128.
50. Stonies, R., et al., *A new small microwave plasma torch*. Plasma Sources Sci. Technol., 2004. **13**: p. 604-611.
51. Hrycak, B., M. Jasinski, and J. Mizeraczyk, *Spectroscopic investigations of microwave microplasmas in various gases at atmospheric pressure*. The European Physical Journal D, Atomic, Molecular, Optical and Plasma Physics, 2010. **60**(3): p. 609-619.
52. Laroussi, M., *Low temperature plasma-based sterilization: Overview and state-of-the-art*. Plasma Processes and Polymers, 2005. **2**(5): p. 391-400.
53. Vleugels, M., et al., *Atmospheric plasma inactivation of biofilm-forming bacteria for food safety control*. Ieee Transactions on Plasma Science, 2005. **33**(2): p. 824-828.
54. Herrmann, H.W., et al., *Decontamination of chemical and biological warfare (CBW) agents using an atmospheric pressure plasma jet (APPJ)\**. Physics of Plasma, 1999. **6**(5): p. 2284-2289.
55. Jeong, J.Y., et al., *Etching materials with an atmospheric-pressure plasma jet*. Plasma Sources Sci. Technol., 1998. **7**: p. 282-285.
56. Jeong, J.Y., et al., *Etching polyimide with a nonequilibrium atmospheric-pressure plasma jet*. Journal of Vacuum Science & Technology A, 1999. **17**(5): p. 2581-2585.
57. Tu, V.J., et al., *Tantalum etching with a nonthermal atmospheric-pressure plasma*. Journal of Vacuum Science & Technology a-Vacuum Surfaces and Films, 2000. **18**(6): p. 2799-2805.
58. Yang, X., et al., *Etching of uranium oxide with a non-thermal, atmospheric pressure plasma*. Journal of Nuclear Materials, 2004. **324**(2-3): p. 134-139.
59. Kim, Y., et al., *Measurements of dioxygen fluoride (O<sub>2</sub>F) in an atmospheric pressure plasma jet*. Applied Physics Letters, 2005. **87**(1): p. -.
60. Moravej, M. and R.F. Hichs, *Atmospheric Plasma Deposition of Coatings Using a Capacitive Discharge Source*. Chemical Vapor Deposition, 2005. **11**: p. 469-476.
61. Kunze, K., et al., *The dielectric barrier discharge as a detector for gas chromatography*. Spectrochimica Acta Part B, 2003. **58**: p. 1435-1443.
62. Franzke, J., et al., *Microplasmas for analytical spectrometry*. J. Anal. At. Spectrom., 2003. **18**: p. 802-807.
63. Miclea, M., et al., *Plasma for lab-on-the-chip applications*. Spectrochimica Acta Part B, 2002. **57**: p. 1585-1592.

64. Kunze, K., et al., *Diode laser-aided diagnostics of a low-pressure dielectric barrier discharge applied in element-selective detection of molecular species*. Spectrochimica Acta Part B, 2002. **57**: p. 137-146.
65. Miclea, M., et al., *The dielectric barrier discharge - a powerful microchip plasma for diode laser spectrometry*. Spectrochimica Acta Part B, 2001. **56**: p. 37-43.
66. Franzke, J. and M. Miclea, *Sample Analysis with Miniaturized Plasmas*. Applied Spectroscopy, 2006. **60**(3): p. 80A - 90A.
67. Guchardi, R. and P.C. Hauser, *A capacitively coupled microplasma in a fused silica capillary*. J. Anal. At. Spectrom., 2003. **18**: p. 1056-1059.
68. Guchardi, R. and P.C. Hauser, *Determination of non-metals in organic compounds by gas chromatography with a miniature capacitively coupled plasma emission detector*. J. Anal. At. Spectrom., 2004. **19**: p. 945-949.
69. Miclea, M., et al., *Microplasma-based atomic emission detectors for gas chromatography*. Anal. Bioanal. Chem, 2007. **388**: p. 1565-1572.
70. Michels, A., et al., *Spectroscopic characterization of a microplasma used as ionisation source for ion mobility spectrometry*. Spectrochimica Acta Part B, 2007. **62**(1208-1215).
71. Eijkel, J.C.T., H. Stoeri, and A. Manz, *A dc Microplasma on a Chip Employed as an Optical Emission Detector for Gas Chromatography*. Anal. Chem., 2000. **72**: p. 2547-2552.
72. Pearse, R.W.B. and A.G. Gaydon, *The Identification of Molecular Spectra*. 1950, London: Chapman and Hall LTD.
73. Smith, P.L., et al. *Atomic spectral line database*. <http://www.pmp.uni-hannover.de/cgi-bin/ssi/test/kurucz/sekur.html>].
74. Zhu, Z., et al., *Application of atmospheric pressure dielectric barrier discharge plasma for the determination of Se, Sb and Sn with atomic absorption spectrometry*. Spectrochimica Acta Part B, 2006. **61**: p. 916-921.
75. Skelton, R.J., et al., *Radio-Frequency Plasma Detector for Sulfur Selective Capillary Gas-Chromatographic Analysis of Fossil-Fuels*. Analytical Chemistry, 1989. **61**(20): p. 2292-2298.
76. Lu, X. and M. Laroussi, *Dynamics of an atmospheric pressure plasma plume generated by submicrosecond voltage pulses*. Journal of Applied Physics, 2006. **100**(6): p. -.
77. Sublet, A., et al., *Atmospheric and sub-atmospheric dielectric barrier discharges in helium and nitrogen*. Plasma Sources Science & Technology, 2006. **15**(4): p. 627-634.
78. Hayen, H., A. Michels, and J. Franzke, *Dielectric Barrier Discharge Ionization for Liquid Chromatography/Mass Spectrometry*. Anal. Chem., 2009. **81**(24): p. 10239-10245.
79. Dole, M., et al., *Molecular Beams of Macroions*. The Journal of Physical Chemistry, 1968. **49**(5): p. 2240-2249.

80. Yamashita, M. and J.B. Fenn, *Electrospray Ion Source. Another Variation on the Free-Jet Theme*. The Journal of Physical Chemistry, 1984. **88**(20): p. 4451-4459.
81. Horning, E.C., et al., *New Picogram Detection System Based on a Mass Spectrometer with an External Ionization Source at Atmospheric Pressure*. Anal. Chem., 1973. **45**(6): p. 936-943.
82. Horning, E.C., et al., *Atmospheric Pressure Ionization (API) Mass Spectrometry. Solvent Mediated Ionization of Samples Introduced in Solution and in a Liquid Chromatograph Effluent System*. J. Chromatogr. Sci., 1974. **12**: p. 725-729.
83. Robb, D.B., T.R. Covey, and A.P. Bruins, *Atmospheric Pressure Photoionization: An Ionization Method for Liquid Chromatography-Mass Spectrometry*. Anal. Chem., 2000. **72**: p. 3653-3659.
84. Syage, J.A., M.D. Evans, and K.A. Hanold, *Photoionization mass spectrometry*. Am. Lab., 2000. **32**(24): p. 24-29.
85. Nissen, W.M.A., *Liquid Chromatography-Mass Spectrometry*. 3rd ed. 2006, Boca Raton, FL: CRC Press.
86. Matthias Mann, C.K.M., and John B. Fenn\*, *Interpreting Mass Spectra of Multiply Charged Ions*. Anal. Chem., 1989. **61**(15): p. 1702-1708.
87. Heming, R., et al., *Electrical generators driving microhollow and dielectric barrier discharges applied for analytical chemistry*. Anal. Bioanal. Chem, 2009. **395**: p. 611-618.
88. Schrittwieser, R., et al., *Cavity-hollow cathodesputtering source for titanium films*. J. Plasma Physics, 2010. **76**: p. 655-664.
89. Eiceman, G.A. and Z. Karpas, *Ion Mobility Spectrometry*. 1994, London, UK: 1st Ed. CRC Press.
90. Vautz, W., et al., *Ion mobility spectrometry for food quality and safety*. Food Addit. Contam., 2006. **23**: p. 1064-1073.
91. Vautz, W., J.I. Baumbach, and J. Jung, *Beer Fermentation Control Using Ion Mobility Spectrometry – Results of a Pilot Study*. Journal of the Institut of Brewing, 2006. **112**(2): p. 157-164.
92. Baumbach, J.I. and M. Westhoff, *Ion mobility spectroscopy to detect lung cancer and airway infections*. Spectrosc. Eur., 2006. **18**: p. 22-27.
93. Vautz, W., A. Michels, and J. Franzke, *Micro-plasma: a novel ionisation source for ion mobility spectrometry*. Anal. Bioanal. Chem, 2008. **2008**: p. 2609-2615.
94. Kostianinen, R. and T.J. Kauppila, *Effect of eluent on the ionization process in liquid chromatography–mass spectrometry*. J. Chromatogr. A, 2009. **1216**: p. 685-699.
95. Qayyum, A., et al., *Diagnostics of nitrogen plasma by trace rare-gas–optical emission spectroscopy*. Journal of Applied Physics, 2005. **98**: p. 103303-1 - 103303-9.

96. Olenici-Craciunescu, S.-B., et al., *Characterization of a capillary dielectric barrier plasma jet for use as a soft ionisation source by optical emission and ion mobility spectrometry*. *Spectrochimica Acta Part B*, 2009. **64**: p. 1253-1258.
97. <http://www.siglo-kinema.com>.
98. Vadla, C., et al., *Optimization of lead metastable production in a low pressure argon discharge*. *spectrochimica Acta Part B: Atomic Spectroscopy*, 2000. **55**: p. 1759-1769.
99. Xiong, Q., et al., *Temporal and spatial resolved optical emission behaviors of a cold atmospheric pressure plasma jet*. *J. Appl. Phys*, 2009. **106**: p. 083302-1 - 083302-6.
100. Kunze, K., et al., *Diode laser-aided diagnostics of a low-pressure dielectric barrier discharge applied in element-selective detection of molecular species*. *Spectrochimica Acta Part B*, 2002. **57**: p. 137-146.
101. Thorne, A.P., *Spectrophysics*. 1988, New York: Chapman and Hall.
102. Ralchenko, Y., A.E. Kramida, and J. Reader. *NIST Atomic Spectra Database*. <http://www.nist.gov/pml/data/asd.cfm>].
103. Su, J.F. and J.L. Nicol, *Measurements of self broadening of the triplet line  $\lambda$  706.5 nm in helium*. *J. Phys. B: At. Mol. Opt. Phys.*, 1990. **23**: p. 2215-2222.
104. Rohe-Hansen, J., K. Jeß, and V. Helbig, *Study of the pressure broadening of the 587.6 nm helium and the 588.2 nm neon lines*. *J. Phys. B: At. Mol. Opt. Phys.*, 1987. **20**: p. 4993-5003.
105. Mullamphy, D.F.T., G. Peach, and I.B. Whittinghams, *Self-broadening of singlet lines of helium*. *J. Phys. B: At. Mol. Opt. Phys.*, 1991. **24**: p. 3709-3726.
106. Lindsay, A.C., et al., *Absorption measurements of resonance broadening in helium*. *J. Phys. B: At. Mol. Opt. Phys.*, 1989. **22**: p. L303-L307.
107. Whitfield, S.B., et al., *Near threshold 4d photoexcitation and photoionization of Xe*. *J. Phys. B: At. Mol. Opt. Phys.*, 1992. **25**: p. 4655-4771.
108. Demtröder, W., *Laser Spectroscopy*. 1996, Berlin: Springer-Verlag.
109. Lochte-Holtgreven, W., *Plasma Diagnostics*. 1968, Amsterdam: North-Holland Publishing Company.



## ACKNOWLEDGMENTS

Herewith I would like to express my gratitude and thank the people that made this thesis possible. The present work was performed at the *Leibniz-Institut für Analytische Wissenschaften-ISAS e.V.* in Dortmund, and was funded by the *Deutsche Forschungsgemeinschaft*.

I am very grateful to PD Dr. Joachim Franzke for offering me the possibility to do my PhD work under his supervision. I thank him for the many fruitful discussions and suggestions in performing the experimental work and data evaluation as well as for the corrections and guidelines in writing my thesis.

Many thanks are directed to Dr. Cedomil Vadla from Institute of Physics in Zagreb, Croatia, for his suggestions and help in experimental work as well as for his support in data evaluation.

I thank to Prof. Dr. Dieter Suter for accepting to be the second referee of this thesis and for the interest shown on this work.

I would like to thank my colleagues that first guided my steps in the laboratory, Antje Michels and Sven Tombrink, and also to Norman Ahlmann for his technical support and practical discussions. Many thanks go to the Miniaturisation group in ISAS for the friendly working atmosphere and collaboration, discussions and fun, as well as for the patience and the help in improving my German language. I thank Ann-Kathrin Stark for the useful discussions and explanations as well as for the collaboration on writing our theses. I am very thankful to Dr. Martin Brücher for the careful reading of my thesis and the corrections he made. Special thanks go to Magnus Eickmeyer for his help in getting me familiar and for arranging my stay in Dortmund, not to forget the friendly discussions with a lot of jokes. I thank the people from the mechanical workshop which I mostly bothered on Friday afternoons, and also the people from the electrical workshop and especially to Dr. Richard Heming that designed and built the “Bogdan Generator” for my plasma discharge.

Last but not least I am deeply indebted to my family and especially to my wife Dr. Alina Olenici-Craciunescu for encouragements and support.





# Curriculum vitae

## Personal data

First name **Stefan-Bogdan**  
Surname **Olenici-Craciunescu**  
Date and place of birth 19.02.1981, Suceava, Romania  
Nationality Romanian  
Marital status married

## Employment

Since April 2008 Research assistant at Leibniz Institut für Analytische Wissenschaften-ISAS e.V. Dortmund

## Education and training

June 2008 -present PhD Student at the Faculty of Physics, Technische Universität, Dortmund  
October 2006 -March 2008 PhD student at the Faculty of Physics, *Alexandru Ioan Cuza University*, Iasi, Romania  
October 2004 -September 2006 Master in Plasma Physics at the Faculty of Physics, *Alexandru Ioan Cuza University*, Iasi, Romania  
September 2000 -July 2004 Bachelor in Physics at the Faculty of Physics, *Alexandru Ioan Cuza University*, Iasi, Romania  
September 1996 -June 2000 High School Graduate Certificate at *Stefan cel Mare National College*, Suceava, Romania

## Awarded scholar-ships

*Erasmus-Socrates*: Institute for Ion Physics and Applied Physics, Leopold Franzens University Innsbruck, Austria  
Nov. 2005–Apr. 2006  
*CEEPUS*:  
May 2005-Jul. 2006, Nov.-Dec. 2006,  
Mar.-Apr. 2007, Jul.-Aug. 2007  
Wissenschaftlich-Technische Zusammenarbeit Österreich-Tschechien:  
Faculty of Mathematics and Physics, Carl University, Prague, Czech Republic  
Nov.-Dec. 2005

## Attended international conferences and published papers

2008-2011

European Winter Conference On Plasma Spectrochemistry, 15.02-20.02.2009, Graz, Austria, **S.B. Olenici-Craciunescu**, A. Michels, R. Heming, S. Tombrink, H. Kleine, W. Vautz, J. Franzke, *Spectroscopic analysis of a dielectric barrier capillary discharge used as a soft ionization source for ion mobility spectroscopy*-poster.

5<sup>th</sup> Nordic Conference on Plasma Spectrochemistry, 6.06-9.06.2010, Loen, Norway

**S.B. Olenici-Craciunescu**, J. Franzke, C. Vadla, *Characterization of a Dielectric Barrier Capillary Discharge Jet Applicable for Soft Ionization in Ion Mobility Spectrometry*-poster.

**S.B. Olenici-Craciunescu**, A. Michels, C. Meyer, R. Heming, S. Tombrink, W. Vautz and J. Franzke, *Characterization of a capillary dielectric barrier plasma jet for use as a soft ionisation source by optical emission and ion mobility spectrometry*, Spectrochimica Acta Part B 64 (2009) 1253-1258.

Heming R., Michels A., **Olenici S.B.**, Tombrink S., Franzke J. *Electrical generators driving microhollow and dielectric barrier discharges applied for analytical chemistry*. Anal. Bioanal. Chem., 395 (2009) 611-618.

**S.B. Olenici-Craciunescu**, S. Müller, A. Michels, V. Horvatic, C. Vadla, J. Franzke, *Spatially resolved spectroscopic measurements of a dielectric barrier discharge plasma jet applicable for soft ionization*, Spectrochimica Acta Part B (2011) doi:10.1016/j.sab.2011.03.005.

C. Ionita, R. Schrittwieser, A. Murawski, Ch. Maszl, M. Asandulesa, A. Nastuta, G. Rusu, M. Dobromir, D. Luca, S. Jaksch, **S.B. Olenici-Craciunescu**, C. Douat, I. Vojvodic, P. Scheier, *Investigations of a cavity-hollow cathode sputtering source for titanium thin films*. C. McKenna: 37th European Physical Society (EPS) Conference on Plasma Physics 2010, Contributed Papers. Mulhouse: European Physical Society, ISBN 2-914771-62-2, P1.312.

R. Schrittwieser, C. Ionita, A. Murawski, Ch. Maszl, M. Asandulesa, A. Nastuta, G. Rusu, C. Douat, **S.B. Olenici**, I. Vojvodic, M. Dobromir, D. Luca, S. Jaksch, P. Scheier, *Cavity hollow cathode sputtering source for titanium thin films*, Journal of Plasma Physics 76 (2010) 655-664.

R. Schrittwieser, A. Murawski, I. Vojvodic, C. Ionita, **S.B. Olenici**, S. Jaksch, P. Scheier, *Probe measurements on a cavity-hollow cathode discharge used as sputter source for titanium*, Acta Physica Universitatis Comenianae (2010) L-LI/1-2, 95-104.